THERMOPHORETIC TRANSPORT AND DEPOSITION OF SUB-MICRON PARTICLES SUSPENDED IN GAS FLOWS

By

Meisam Mehravaran

A DISSERTATION

Submitted to
Michigan State University
in partial fulfillment of the requirements
for the degree of

Mechanical Engineering-Doctor of Philosophy

2013

ABSTRACT

THERMOPHORETIC TRANSPORT AND DEPOSITION OF SUB-MICRON PARTICLES SUSPENDED IN GAS FLOWS

By

Meisam Mehravaran

Thermophoretic transport of small particles in gas flows has many scientific and engineering applications, but has not been studied widely and is not well understood. Thermophoretic forces arise in the presence of temperature differences, which drive particles from hotter to colder regions of flows and may lead to deposition on surfaces, which may degrade heat transfer. Previous studies have shown that, in flows with sub-micron particles, and temperature gradients of the order of 10 K/cm, thermophoresis can be a dominant particle transport mechanism. In the research described in this proposal, the governing equations for mass, momentum, energy and species have been formulated and approximate boundary conditions for particulate transport have been proposed. A new series solution has been obtained for the particle concentration field in steady laminar tube flow, the results of which are consistent with particle deposition experiments. The effects of the tube entrance zone and of gas compressibility have been studied using computational fluid dynamics, and also compare well with experimental observations. In the case of steady turbulent duct flows, approximations based on existing direct numerical simulation results lead to a simple 1D model for the deposition efficiency of sub-micron particles that compares well with results of several experimental studies.

There are also many engineering applications in which thermophoretic transport of particles takes place in unsteady pulsating flows, though there have been no previous studies of these problems. In the second part of this thesis, the effect of oscillating flows on ther-

mophoretically driven mass transfer is investigated. It is found that unsteadiness has little or no effect on thermophoretic transport when the direction of flow oscillation is normal to the direction of heat transfer. However, when the directions of flow oscillation and heat transfer are aligned, flow oscillation can lead to significant enhancements in both heat transfer and thermophoretic mass transfer. In the particular problem of oscillating slug flow with an axial temperature gradient, it is found that the mass transfer is enhanced by up to 3 orders of magnitude over its steady rate. Variation of the frequency of oscillation reveals a tuning effect whereby a particular oscillation frequency maximizes the effective thermophoretic diffusivity. In the case of a considerable convective velocity in the direction normal to heat transfer-such as a porous channel flow with a pulsating vertical component of velocity, it is seen that thermal disturbances travel quickly in the longitudinal direction. Thus, in order to attain a tuning effect, a very high pulsating frequency would have to be imposed in the vertical direction, which would require high velocities that would surpass laminar thresholds and is impractical in most circumstances. In many industrial applications, the effect of unsteadiness on heat transfer and thermophoretic mass transfer is negligible. However, significant effects of mass-transfer enhancement could theoretically be observed in a few specialized devices such as conductive heat exchangers, if the heat transfer and flow oscillation periods coincide. This enhancement is a kind of thermal resonance which can theoretically occur when heat transfer takes place slowly, but it is a specialized effect and depends on the characteristics of the heat/mass transfer device and the frequencies of flow and thermal oscillation.

TABLE OF CONTENTS

LIST OF TABLES

LIST OF FIGURES

Chapter 1

Introduction

Particle-laden flows are important in many scientific and industrial processes such as particle and droplet deposition in gas and steam turbines, fouling processes in heat exchangers and thermoelectric devices, and in the transport of chemical aerosols, atmospheric dispersal of pollutants and determination of indoor air quality. In the recent years, considerable attention has been given to biomedical applications of particulate transport such as the development of efficient devices for drug delivery by inhalation and the prediction of exposure levels to particulate matter and pollutants in indoor and outdoor environments. Relatively little research has been carried out on these applications of particulate laden flows, many of which are poorly understood, and more is needed to provide a better understanding of particle transport and deposition.

The motion of particles and the flow in which they are suspended are generally coupled. Based on the interaction between the particles and the carrier phase, the coupling between the flow and the particles can be categorized as either one-way, two-way or four-way couplings [41]. In flows with dilute concentrations of small particles, the flow affects the particles while the effect of particles on the flow is negligible–a one-way coupling. In the case of large particles (greater than 10 μm) or high concentration (above 2% volume fraction), the particles and the flow affect each other, which is referred to as 'two-way' coupling [95]. When particles interact with both one another, by collision, hydrostatic charge, etc., as well as with the fluid, the particle-particle and particle-flow interactions are considered a four-way

coupling [71].

The methods used for modeling particulate transport and deposition can be divided into Eulerian [41] and Lagrangian approaches [33, 88]. In the Eulerian schemes, the evolution of the concentration of particles is traced through points fixed in an Eulerian reference frame. In the Lagrangian approach, the equations of motion are solved for a large number of particles and the trajectory is traced for each particle separately. In general, Eulerian methods are computationally faster than Lagrangian schemes though handling the boundary conditions is more difficult. Eulerian particle transport equations can be solved making use of Eulerian flow solvers that usually have high computational efficiency. Lagrangian methods are easier to implement and can take advantage of parallel processing computations, especially when the fluid-particle coupling is 'one-way.'

Deposition of particles has been studied by many researchers. One characterization of experimental studies [77, 87, 34] on particle deposition is according to the 'S'-shaped curve shown in Fig. 1.1, which can be categorized as the three distinct regions: region 1 in which turbulent diffusion dominates other transport mechanisms; region 2 in which turbulent diffusion-eddy impaction is significant; and region 3, in which effects of particle inertia are considerable. The different modes of deposition have been identified by Guha [41] as: thermophoresis, turbophoresis and Fickian diffusion, with each mode most relevant to a particular range of particle size. Guha also proposed a unified Eulerian approach to predict the deposition velocity of particles in all three regions of Fig. 1.1. In this figure the ordinate is $v^+{}_{dep} = \dfrac{v_{dep}}{u^*}$ and the abscissa is $\tau^+ = \dfrac{\tau {u^*}^2}{\nu} = \dfrac{1}{18}\left(\dfrac{\rho_p}{\rho}\right)\dfrac{{d_p}^2 {u^*}^2}{\nu^2}$ where u^* is the friction velocity, d_p is the particle diameter, ρ_p is the density of particulate material, ρ and ν are the bulk density and viscosity, and τ^+ is the dimensionless particle response time. Based on his studies, the transport of small particles which lie in region 1 ($\tau^+ < 0.2$) can be

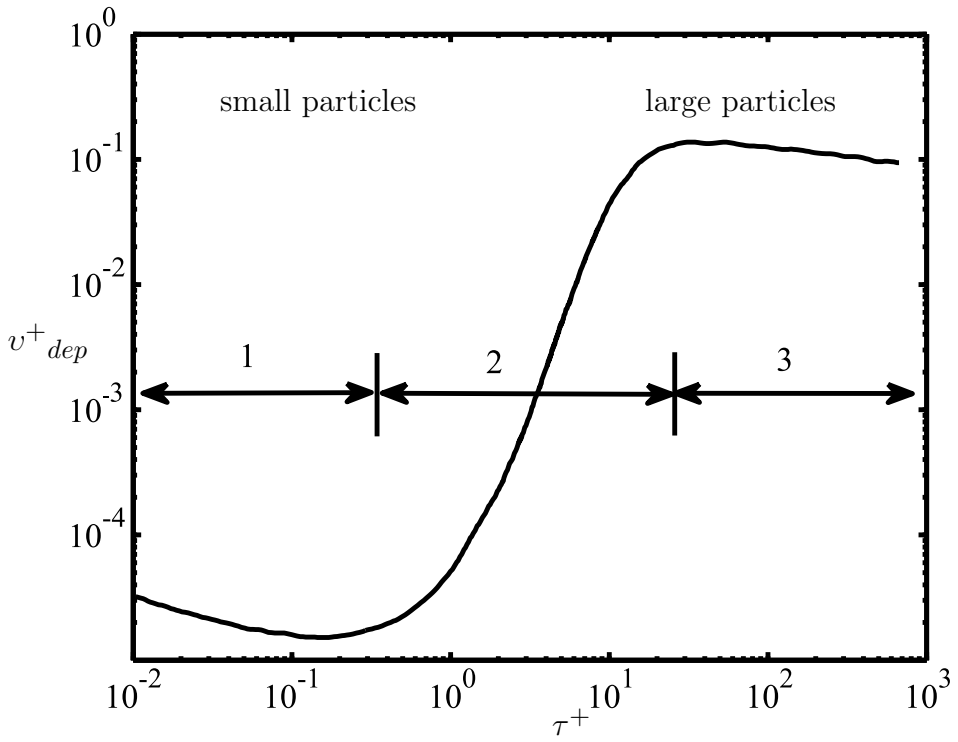

Figure 1.1: Measured deposition velocity v^+_{dep} as a function of particle relaxation time τ^+ in fully developed vertical pipe flow. The regimes are: 1-turbulent diffusion; 2-turbulent diffusion/eddy impaction; and 3-particle inertia moderated (from [41].)

accurately described by a modified Fickian diffusion model, while the behavior of particles of longer relaxation time that are beyond region 1 is more complicated and the solution of two additional momentum equations is required (the reader is referred to Guha's comprehensive article for more details [41] on the subject).

In flows with low concentration ($< 2\%$ volume fraction) of fine particles (< 10 μm diameter), the coupling between the flow and the particles is usually characterized as a one-way coupling, in which the flow and temperature fields drive the motion of particles but the particles have negligible effect on either the flowfield, the temperature field, or each other [41]. As the density of solid particles is much larger than the density of air, the mass-fraction may be quite large even in case of very small volume fractions, so the properties of the air may be replaced by a weighted average values of air and particle properties,

but in higher concentrations the behaviour will be more complex and two-way coupling is recommended [95] . While the equations governing one-way-coupled particle transport can be formulated and simplified in a straightforward manner, few analytical studies of thermophoretic particle transport and deposition have been carried out using the Eulerian approach since the theoretical treatments of Goren [40], who considered similarity solutions to the high-speed compressible flat-plate boundary layer in the absence of Brownian diffusion, and Batchelor and Shen [6] who presented series solutions (with complementary Blasius series calculated by Homsy et al. [51]) and numerical-calculation results for incompressible laminar thermophoretic flows for the geometries of: the flat plate; the cylinder and the body of revolution. Walker et al. [136] carried out a constant-property analysis of the entrance region of a pipe flow that included an asymptotic treatment of the surface diffusive sublayer, and made Lagrangian calculations of deposition efficiency in the developed downstream region. Weinberg [140] also derived mathematically the result for laminar, constant wall temperature pipe flow that the particle concentration at the edge of diffusive sublayer takes the constant value of $c_o T_w/T_o$ at all axial locations when $K_{th}\,\mathrm{Pr} = 1$, but otherwise is not necessarily a constant. In these studies, attention was drawn to the extreme thinness of the surface sublayer within which effects of Brownian diffusion, which are essential for accommodating a surface particle-concentration boundary condition, are as important as those of thermophoresis. In case the of submicron particles, the corresponding Schmidt number is of the order of 10^5 and since the thickness of this sublayer scales in inverse proportion to the particle Schmidt number, its thickness in gas flows laden with fine particles is typically 10^{-4} to 10^{-6} times that of the hydrodynamic boundary layer. Consequently it is extremely difficult to resolve the concentration field in this sublayer in computations.

Thermophoretic particle deposition efficiencies have been measured in a number of ex-

perimental studies. These include the pipe-flow experiments of Romay et al. [107] in which hot air seeded with submicron sodium chloride particles flowed steadily within a long cooled pipe, under both laminar and turbulent conditions, and the studies of Montassier [91] and Stratmann et al. [123] of particle deposition under laminar conditions in the thermal entrance region of pipe flows. Gonzalez et al. [38] have measured the deposition efficiency and uniformity of iron and sodium chloride nano-particles in a precipitator and found good agreement between theoretical and experimental efficiencies. Maynard [86] and Bang et al. [5] have developed thermophoretic precipitators for electron microscopy analysis of ultrafine particles, which yielded deposition that was uniform locally but non-uniform over scales larger than a few microns.

Tsai and Lu [132] have also measured the collection efficiency of submicron sodium chloride and sodium flourescein particles in laminar flow in a plate-to-plate thermophoretic precipitator. Their deposition-efficiency data and those of Messerer et al. [90] are in excellent agreement with the theoretical deposition efficiency obtained from Lagrangian particle trajectory calculations, when the model of Talbot et al. [125] is used to compute the thermophoretic coefficient. More recently, experimental data on deposition efficiency has been supplemented by numerical simulation results for the transport of small particles in computational domains, such as those of He and Ahmadi [48].

There have also been many other studies of related aspects of thermophoretic flows. Rosner [108], and Rosner and Khalil [109] have explored differences between thermophoretic transport of monodispersed and polydispersed aerosol particles, and shown that deposition of some polydispersed particles can be predicted by applying an appropriate correction to a corresponding deposition rate of a monodisperse counterpart. The problem of thermophoretic deposition in open systems under natural convection has been studied as a model problem

for understanding particle deposition onto wafers in micro-electronic fabrication, and for designing effective smoke filters and clean rooms. For example, Chang et al. [13] have carried out numerical calculations to show that the rates of deposition of submicron particles on vertical cooled plates in natural-convection environments are influenced strongly by both thermophoresis and buoyancy. Ye at al. [143] have studied numerically and experimentally the deposition of monodisperse aerosol particles on a heated vertical wafer surface and found good agreement between measured and computed particle deposition velocities. Sasse et al. [112] have investigated particle migration under thermophoretic and buoyant forces to provide guidelines for the design of filters and to predict their efficiency of particle removal. In preparation for the proposed use of extreme ultraviolet lithograthic techniques in making semiconductor wafers, Asbach et al. [4] have discussed how thermal gradients might be applied to repel thermophoretically nanoparticle that might otherwise contaminate masks. Also, the use of thermophoresis as a protective force has been examined at atmospheric pressures by Peterson et al. [100] and at reduced pressures by Choi et al. [17].

The motion of particles suspended in liquids, driven by temperature gradients, is called the Soret or Ludwig-Soret effect. Although Ludwig [79] described this phenomenon several years before Soret, the name "Soret effect" is usually used in recognition of the comprehensive investigations of Soret on separation of various species by temperature gradient [121, 120]. The thermophoretic force is a linear function of temperature gradient in liquids while it is a logarithmic function of temperature gradient in gases, and so there is little overlap between the two research areas. In the current study, we concentrate on particulate gas flows and the reader is referred to the articles of Platten [101] and Parola [99] for more information on thermophoretically-driven particle transport in liquids.

1.1 Soot Particles

Thermophoretic transport and deposition occurs in many engineering applications such as exhaust gas recirculation (EGR) coolers, combustion chambers, thermoelectric devices and industrial heat exchangers. In most of these applications, soot and combustion products deposit on cooled surfaces, which degrades the heat transfer efficiency considerably and can lead to the fouling of flow passages. Soot deposits may also increase the pressure drop along ducts, which can decrease engine efficiency and increase fuel consumption. Moreover, soot deposits are acidic and may cause corrosion of surfaces. Since an understanding of soot particles is useful for understanding these problems, a short description of soot formation and soot properties is given below.

1.1.1 Soot Formation, Coagulation and Aggregation

During combustion, embryonic soot particles are first formed in a process known as nucleation. These particles then grow as a result of the two distinct processes of coagulation and surface growth. In coagulation, two particles collide and stick together to form a larger particle. In surface growth, smaller species (around 1.5 nm) such as gaseous hydrocarbons or small nuclei attach to soot nuclei to form visible soot particles. As these growth mechanisms do not occur monotonically, soot particles have different sizes ranging from 5-200 nm and are usually an agglomeration of spherules that are approximately 30 nm in diameter [103, 118]. Tian et al. [130] used transmission electron microscopy (TEM) to study the morphology of soot aggregates, while Suzuki et al. [124] observed that the thermophoretic transport of an aggregated particle is governed by the primary particle size rather than the aggregate size, which can be a considerable simplification in modeling soot deposition. Maricq measured

both the size and electrical charge distributions of soot particles, using a nano differential mobility analyzer (DMA). He reported that soot particles have bimodal size distributions and are 5-200 nm in diameter. His measurements revealed that most soot particles possess electrical charges but the number of positive and negative charges are almost equal which makes the exhaust soot electrically neutral [84, 85]. The size, morphology and distribution of soot particles may also be affected by other factors which are discussed next.

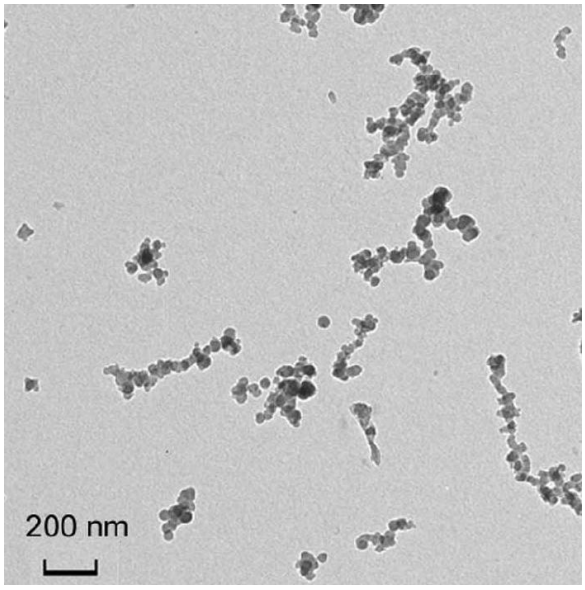

Figure 1.2: TEM image of soot aggregate sampled from an ethylene/air diffusion flame [130]

1.1.1.1 Pressure Effects

Rosner et al. [109] studied the morphology of particle aggregates and discussed the effect of high pressure on their behaviour. They observed that at high pressures the deposition rate of aggregates is considerably greater than spherule deposition and this disparity increases as the pressure increases (Fig. 1.3). At high pressures (such as peak pressures in internal combustion engines which are around 50 bars), preventing the formation of aggregates or breaking them up before thermophoretic deposition (i.e. by decreasing the 'stickiness' of

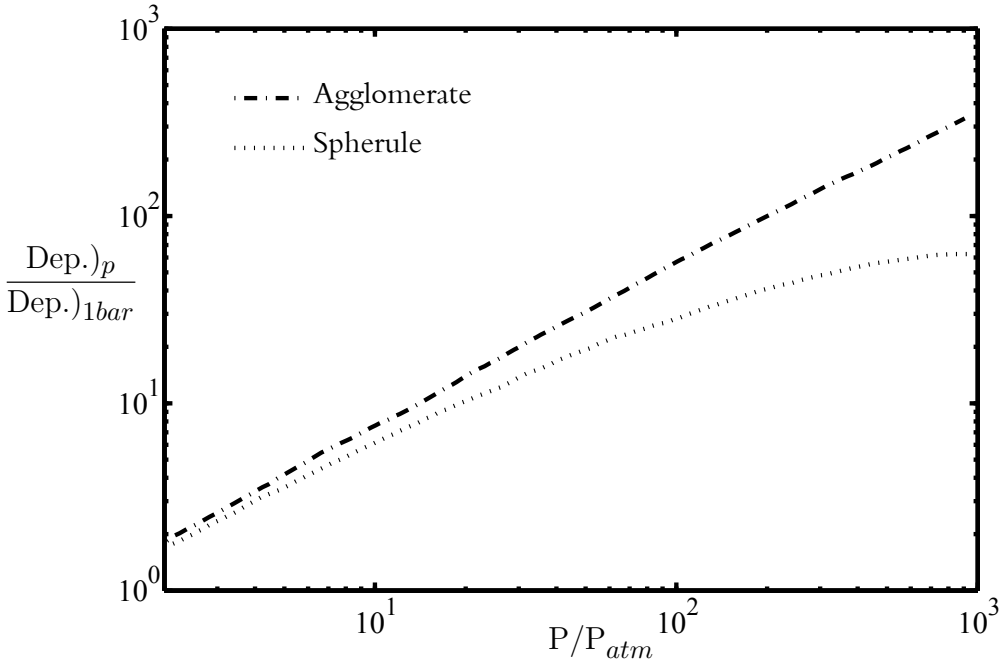

Figure 1.3: The effect of pressure on deposition rate for different morphologies of soot particles

spherules), can decrease the soot deposition rate appreciably. This observation applies to deposits in combustion chambers where high pressures are reached, but not in EGR coolers where the pressures are typically much closer to atmospheric.

1.1.1.2 Effects of Engine Operating Conditions

A comprehensive study was carried out by Neer et al. [96] on the effect of operating conditions on the size, morphology and concentration of sub-micron soot particles in a Diesel engine. They used transmission electron microscopy (TEM) to measure particle concentration, size and morphology and showed that the distribution of spherule size falls within a very narrow band of 20-35 nm, while the aggregate size shows broad variations. They also reported that the sizes of both spherules and aggregates decreased when the engine load was increased. A similar trend was observed when equivalence ratio was increased. In a similar study, Manzello et al. [81, 80] considered the effect of equivalence ratio on the size

distribution of soot particles in a well-stirred reactor (WSR) and noticed a similar trend of increasing average soot particle size with increasing equivalence ratio. They reported that at the equivalence ratio of 1.9 soot particles are 7-8 nm, compared to 15-16 nm for the equivalence ratio of 2.0. In other words, fuel-lean combustion leads to smaller aggregates than fuel-rich combustion.

The geometry of aggregates has been found to have a fractal nature and inferences about their 3-D morphology could be made from 2-D TEM images (see [67, 53] for more details). Neer et al. [96] studied the morphology of aggregates in terms of their fractal properties and reported that their fractal dimension is almost independent of operating conditions, while their fractal prefactor implied that the aggregate formation is mostly due to cluster-cluster collision mechanisms.

1.1.2 Soot Deposit Properties

Several researchers have provided data on the thermal properties of soot deposits, but the discrepancies among the reported values are large. Soot aggregates have irregular shapes so they form layers with high porosities. Their properties may vary significantly depending on the amount of condensed vapor or hydrocarbon. Nishiwaki [97] reported a thermal conductivity of 0.68 W/m-K and a volumetric heat capacity of 250 KJ/m^{3}K for combustion chamber deposits, while Nakamura et al. [94] measured thermal conductivities of around 0.16 W/m-K and heat capacities ranging from 0.96-1.55 J/g-K for the same type of deposits. Konstandopoulos [66] measured the soot deposits in diesel particulate filters (DPF) and observed that the soot cake density varied between 40 and 135 kg/m^3. In a recent study by Lance et al. [72] of thermal properties of EGR cooler deposits, several EGR cooler tubes were exposed to exhaust gas for around 12 hours and the properties of deposits were

measured using the Xenon flash lamp method. It was observed that the heat capacity of these deposits were 0.82-0.87 J/gK which is slightly higher than graphite, and the thermal conductivity was 0.041 W/m-K, which is 50 % higher than air. The soot cake therefore acts as an insulator because of the high porosity of deposits (around 98% porous).

1.2 Other Particles

Other particle-laden flows include air-borne dust in respiratory systems, aerosols, micro-organisms and other toxic and non-toxic materials. The transport and deposition of particles depends strongly on their size. For example, occupational dusts may be 0.001-1000 μm, pollen particles are 20-60 μm, cigarette smoke particles are 0.2-0.6 μm, and viruses and proteins may be in the range 0.001-0.05 μm. In some cases, specific particles may be introduced through the respiratory system for medical purposes (drug delivery). This technique is effective as the human lung has a very large surface area and so provides rapid delivery to the blood flow with minimal side effects. As the temperature gradients within air flows in the lung are very small, the thermophoretic transport is negligible compared to other mechanisms such as inertial impaction, Fickian diffusion and gravitational settling. Several theories and models have been developed for evaluating the deposition of particles in the respiratory system [126, 50].

Flows in gas and steam turbines contain droplets or particles. Experiments show [12, 19, 145] that water droplets in turbines have a wide size range, and that more than 90% of the vapor is in the form of fog which has a very small diameter of 0.05-2.0 μm while the remainder is in the form of coarse droplets of 20-200μm in diameter. In cooled gas turbines the blade is 300-400K colder than the flow, and so thermophoresis is a significant

mechanism in droplet deposition. Aircraft engines have also encountered difficulties when passing through volcanic ash clouds, as suspended and deposited particles may block the cooling holes of the turbine blades. Similar problems may occur in heavily particle-laden flows such as explosive eruptions and sand storms, and can lead to significant damage to airplane engines [29].

1.3 Objectives

While there is a significant body of research on various aspects of particulate flows, there are very few research results that can be used to make reliable engineering predictions of the rate of deposition of particles on a cold surface. Also, while considerable attention has been paid to particle-laden flows in the entrance regions of ducts, or in developing boundary layers, there do not appear to have been any studies of particle concentration fields and particle deposition in fully-developed duct flow. Experimental measurements have generally been restricted measurements of surface deposition rates and deposition efficiencies, and there do not appear to be any measurements of particle concentration profiles in developing or developed duct flows. The objectives of the research presented in this dissertation are therefore:

i) to identify model and constitutive equations to evaluate the thermophoretic mass-flux and deposition accurately;

ii) to develop a reliable engineering technique for making predictions of deposition on cold surfaces in duct flows;

iii) to calculate the shape of particle concentration profiles in fully-developed duct flows; and

iv) to explore unsteady flow effects on thermophoretic particle transport.

We first review the theoretical background of thermophoretic particle transport and the corresponding mass flux and transport equations in Chapter 2. Thermophoretic transport in steady duct flows is then studied using numerical and analytical approaches in Chapter 3, together with a discussion of boundary conditions for computation of thermophoretic flows in Chapter 4. A simple model for particle deposition in turbulent flow is described in Chapter 5, while effects of unsteadiness on thermophoretic transport, including effects of pulsation on both heat and mass transfer, are analyzed in Chapter 6.

Chapter 2

Theoretical Background

In this chapter, the theoretical background for models of thermophoretic force on particles and particulate fluxes is presented together with the governing fluid transport equations and a new definition of thermally driven mass transfer coefficient. The background applies to submicron particles in flows with temperature gradients of at least 10 K/cm, in which thermophoresis is expected to be significant.

2.1 Particulate Fluxes

In the derivation of transport equations for the continuous phase in a multiphase flow, it is necessary to introduce models for the effect of the particulates on the continuous phase and their coupling. In this study of submicron particulate transport, we employ a one-way coupling model in an Eulerian scheme which neglects the effect of particles on the carrier phase and is appropriate for submicron particles. The three main mechanisms of particulate transport [41] are: thermophoresis, turbophoresis, and Fickian diffusion, which will be discussed below.

Turbophoresis is the bulk displacement of particles from regions of higher to lower turbulent kinetic energy. Following Guha [41], turbophoresis is an important mechanism for particles of large time response ($\tau^+ > 1$ in Fig. 1.1) and must be evaluated by solving the particulate momentum equations. In the case of submicron particles such as soot, which

have a short time response, effects of turbophoresis are small and may be neglected.

Fickian diffusion describes molecular transport from regions of higher to lower particle concentration. In turbulent flows, this flux can be approximated by employing a modified Fick's law of diffusion, with an effective turbulent diffusivity:

$$J_r = -(D_B + D_t)\frac{\partial c}{\partial r} \tag{2.1}$$

where J_r is the radial particulate mass flux, D_B is the Fickian, Brownian or molecular diffusivity of particles in the surrounding fluid, D_t is the mean effect of velocity and concentration fluctuations when the flow is turbulent and is modeled as a diffusivity, and c is the local particle concentration in units of density. The molecular or Brownian diffusion D_B is represented by the Einstein equation

$$D_B = \left(\frac{kT}{3\pi\mu d_p}\right) C_c \tag{2.2}$$

where C_c is Cunningham's correction for rarefied-gas effects: $C_c = 1 + 2.7Kn$ [20]. In this equation, k is Boltzmann's constant, μ is the fluid viscosity, d_p is the particle diameter and Kn is the Knudsen number. The turbulent diffusivity D_t is usually modeled empirically [104, 58].

2.1.1 Thermophoresis

Thermophoresis is a phenomenon wherein small particles are driven by molecular collisions in the direction opposite to that of the temperature gradient $\partial T/\partial r$. This effect is a consequence of higher molecular kinetic energies at higher temperatures which impose an unbalanced force

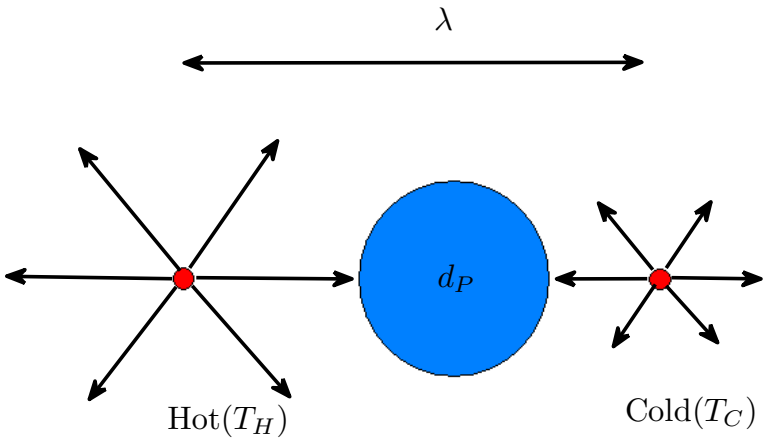

Figure 2.1: Unequal molecular impact on a particle due to the temperature gradient (For interpretation of the references to color in this and all other figures, the reader is referred to the electronic version of this dissertation)

on either side of a particle in a temperature gradient and so drive the particle to the colder zone (see Fig. 2.1). Thermophoresis can be a significant force on sub-micron particles such as soot particles, aerosols, etc, when the temperature gradient exceeds 10 K/cm. It is noticeable that unequal pressures on both sides of the particle will lead to drag force which is important in Lagrangian approach. In the current Eulerian approach a thermophorectic velocity is derived based on the balance between the themophoretic and drag forces that takes care of both effects simultaneously.

The phenomenon of thermophoresis was first investigated as a fundamental physical process by Maxwell (cf. [61]), for flows in which the mean free path of the gas was slightly smaller than the size of particle. He observed that a shear stress is exerted by the gas on the wall in the direction opposite to that of the temperature gradient and, since an equal and opposite shear stress is exerted by the wall upon the gas, a thermal slip occurs towards the

hotter region. Epstein approximated the force exerted on spherical particle in a gas at rest due to temperature gradients [31]. He derived an expression for the thermophoretic force and the subsequent velocity for small Knudsen numbers ($Kn = 2\lambda/d_p$ where λ is the mean free path of the gas) as:

$$F_{th} = -\frac{9\pi\mu\nu d_p \nabla T}{4T_0}\left(\frac{k_g}{k_p + 2k_g}\right) \tag{2.3}$$

where μ is the absolute: viscosity, ν is the kinematic viscosity, d_p is the diameter of particles, T_0 is the mean gas temperature, ∇T is the temperature gradient, and k_g and k_p are the thermal conductivities of the gas and particles respectively. Epstein's formula compares well with experimental data for particles of low thermal conductivity and Knudsen number, but underestimates the thermophoretic force of particles of higher thermal conductivity significantly. A number of attempts have been made to generalize Epstein's relation for higher conductivities which are to be described next. Waldmann extended Epstein's analysis by adding the first term in the expansion of a Sonine polynomial and derived a relation for the thermophoretic force in the asymptotic case of large Knudsen numbers [135].

Brock used a hydrodynamic approach to evaluate the thermal force based on Navier-Stokes-Fourier theory with a slip-corrected boundary condition [9]. Although Brock's results are better than Epstein's results when compared to experimental data, the discrepancy is still considerable. Based on the balance between the thermal force and the Millikan drag, the thermophoretic velocity can be approximated as:

$$v_{th} = -\frac{2C_s\nu\left(\frac{k_g}{k_p} + C_t Kn\right)\nabla T/T_0}{(1 + 2C_m Kn)\left(1 + 2\frac{k_g}{k_p} + 2C_t Kn\right)} \tag{2.4}$$

where C_m=1.14 and C_t=2.18. Derjaguin and Yalamov solved used an approach employing

irreversible thermodynamics and Onsager's reciprocatory relations [26, 27] to deduce that the magnitude of the thermophoretic velocity was

$$v_{th} = -\frac{3\nu\left(\frac{k_g}{k_p} + C_t Kn\right)\nabla T/T_0}{\left(1 + 2\frac{k_g}{k_p} + 2C_t Kn\right)} \tag{2.5}$$

which is similar to the Brock's relation, except for the factor of $(1 + 2C_m Kn)$. Gorelov solved the linearized Boltzmann equation numerically and evaluated the thermophoretic force for two distinct values of k_g/k_p=0.2 and 0.002, but did not present a general relation for evaluation of the thermal velocity [39].

It is desirable to have a simple relation which can predict the thermophoretic force and velocity over a wide range of Knudsen numbers and conductivity ratios. Cha and McCoy [11] and Wood [141] proposed an expression for the thermophoretic force as a function of particle properties and Knudsen number, but their results underestimate the experimental data and fail to approach Waldmann's predictions in the free-molecular regime. Although the CMW (Cha, McCoy and Wood) model underestimates the thermal force, it follows the same trend as the experimental data. Talbot made an interpolation which matched the theory in the asymptotic cases of continuum and free-molecular limits [125]. By assuming that the thermal force is balanced by the Millikan drag, the thermophoretic velocity may be derived as:

$$v_{th} = -K_{th}\nu\frac{\nabla T}{T_0} = -\frac{3C_s\nu\left(\frac{k_g}{k_p} + C_t Kn\right)\left[1 + Kn(A + B.\exp(c_1/Kn))\right]\nabla T/T_0}{(1 + 3C_m Kn)\left(1 + 2\frac{k_g}{k_p} + 2C_t Kn\right)} \tag{2.6}$$

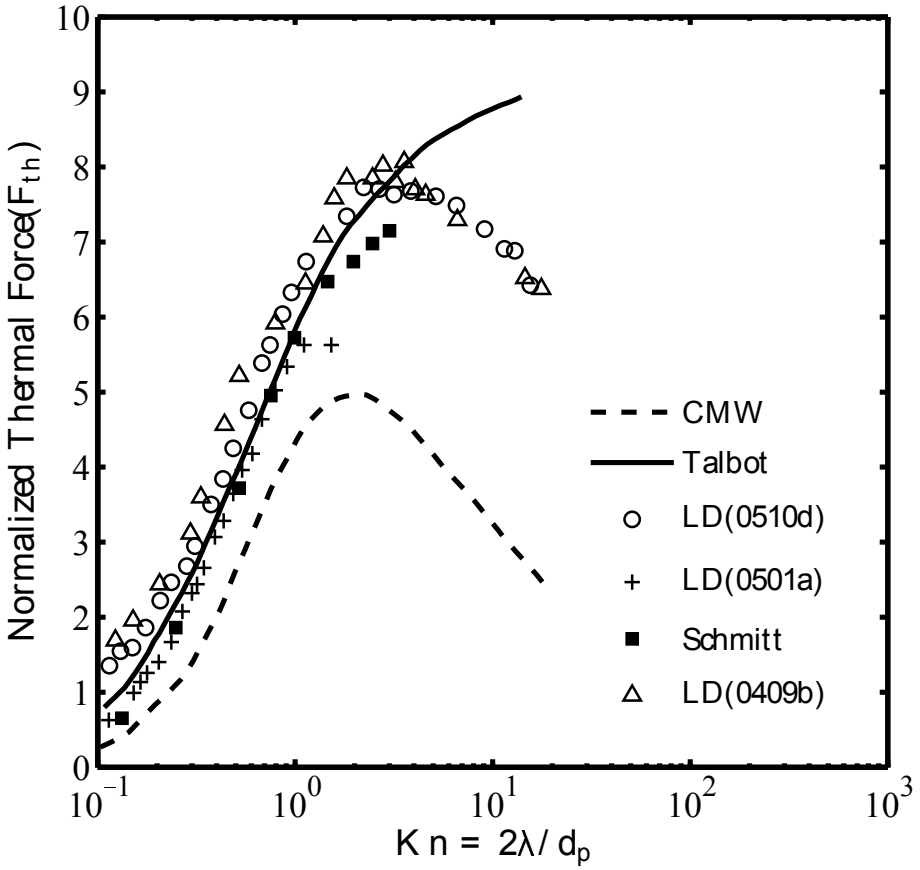

Figure 2.2: Comparison of Talbot and CMW models with the experimental measurements of Li and Davis [75, 74] and Schmitt [114]

This formula compares well with the results reported by Gorelov at $\frac{k_g}{k_p} = .2$ and shows good agreement with the experimental data over a wide range of Knudsen numbers and conductivity ratios [39] and so is used to model thermophoretic particle flux as $J_{th} = -K_{th}\nu c\frac{\partial(Ln(T))}{\partial r}$ and so $J_r = c(v_r + v_{th}) - D\frac{\partial c}{\partial r}$.

In the last two decades, thermophoresis of particles at intermediate Knudsen numbers has been studied extensively and the thermophoretic force has been approximated based on the solution of the linearized Boltzmann equation [119, 142, 78]. Li and Davis measured the thermophoretic force using electrodynamic levitation and showed that kinetic theory models are in good agreement with their experimental data [75, 74] for Knudsen numbers from 0.1 to 10. Sone and Aoki [119], Yamamoto and Ishihara [142], and Loyalka [78] predicted that at high conductivity ratio ($k_p/k_g \gg 1$), negative thermophoresis is possible according to the Boltzmann equation, though this phenomenon has not been reported in experiments. It is noticeable that such a negative thermophoretic force is very small and the precision of measurement instruments may not be sufficient to resolve it.

He and Ahmadi [48] compared Talbot's model with experimental data of Li and Davis and the CMW model. It is seen that the CMW model underestimates the thermal force while the widely used Talbot relation is found to be quite accurate for particles with Knudsen numbers of 3 or less (see Fig. 2.2). Tsai et al. carried out experiments on thermophoresis in a plate-to-plate precipitator and a tube flow for a wide range of Knudsen numbers. They reported that Talbot's formula is accurate and can predict the experimental data with the difference of less than 10% [132, 131]. Similar experiments were conducted by Bueno and Rucadio for submicron aerosols at higher temperature gradients which confirmed the precision of Talbot's formula to within 10% of the experimental data [93]. Kim et al. [62] investigated the transport of sub-micron particles of 0.5<Kn<83 experimentally and modified the original

Talbot equation and the corresponding coefficients of K_{th} as:

$$K_{th} = 2\, C_c\, C_s \frac{k_g/k_p + C_t \mathrm{Kn}}{(1 + 3C_m \mathrm{Kn})\left(1 + 2k_g/k_p + 2C_t \mathrm{Kn}\right)} \tag{2.7}$$

where $C_c = 1 + (1.165 + 0.483e^{-0.997/\ \mathrm{Kn}})\ \mathrm{Kn}$ is the Stokes slip correction for rarefied-gas effects as an improvement on the original model of Cunningham [20], Kn is the particle Knudsen number, C_s, C_t and C_m are thermal slip, temperature jump and momentum exchange coefficients and take values of 1.147, 2.20 and 1.146 respectively [6], while k_g and k_p are the thermal conductivities of the gas and the particles.

Since we are interested in soot, which is an agglomerate of carbon spherules and has an effective Knudsen number of around unity, the Talbot relation seems to be a reliable model for predicting the thermophoretic force and the corresponding velocity and has been used in industrial applications by several researchers [2, 70, 138]. When Kn$\gg$1, in the free molecular regime, Waldmann and Schmitt [134] recommend for the thermophoretic coefficient K_{th} the value of 0.55. In general, a value for K_{th} of 0.5 is a reasonable approximation for Knudsen numbers of 0.5 and higher, while it decreases at lower Knudsen numbers, though a more accurate value of K_{th} could be calculated from Talbot's formula. It is noticeable that in the asymptotic case of large Knudsen numbers Talbot's formula predicts a value of K_{th} of 0.57, independent of particle and flow properties.

In summary, Talbot's relation appears to be the most trustworthy constitutive equation for the prediction of K_{th} for a given particle and Knudsen number, from which the thermophoretic velocity v_{th} and the particulate flux may then be expressed. This flux is used in the following sections to close the particle transport equations.

2.2 Transport Equations

Since particle transport is often of most interest in circular duct flows and within boundary layers, we present the governing fluid transport equations in axisymmetric boundary-layer form. For the case of steady, laminar boundary-layer flow with constant bulk properties and negligible pressure work and body forces, when a one-way coupling between the fluid and particulate phases is justified, the continuous-phase x-momentum and thermal energy equations are:

$$u\frac{\partial u}{\partial x} + \upsilon\frac{\partial u}{\partial r} = -\frac{1}{\rho}\frac{\partial P}{\partial x} + \frac{\nu}{r}\frac{\partial}{\partial r}\left(r\frac{\partial u}{\partial r}\right) \tag{2.8}$$

$$u\frac{\partial T}{\partial x} + \upsilon\frac{\partial T}{\partial r} = \frac{\alpha}{r}\frac{\partial}{\partial r}\left(r\frac{\partial T}{\partial r}\right) \tag{2.9}$$

The species diffusion equation describes particulate transport by advection, diffusion and thermophoresis and so is written in the general boundary-layer flux form:

$$\frac{\partial}{\partial x}(\rho u c) + \frac{\partial}{\partial r}(\rho v c) = -\frac{1}{r}\frac{\partial}{\partial r}(\rho r J_r) \tag{2.10}$$

where J_r is the summation of Fickian and thermophoretic fluxes. After combining with a bulk continuity equation, the particle diffusion equation may be written as:

$$u\frac{\partial c}{\partial x} + \upsilon\frac{\partial c}{\partial r} = \frac{D_B}{r}\frac{\partial}{\partial r}\left(r\frac{\partial c}{\partial r}\right) + \frac{K_{th}\nu}{r}\frac{\partial}{\partial r}\left(\frac{rc}{T}\frac{\partial T}{\partial r}\right) \tag{2.11}$$

where c is the particle concentration. The relative sizes of the thermophoretic and diffusive transport terms on the right-hand side of this equation depend on K_{th} and D_B and so their ratio depends on the dimensionless group $K_{th}Sc$, where Sc is the particle diffusion Schmidt

number. Large values of $K_{th}Sc$ correspond to flows in which thermophoretic effects dominate the diffusive ones. When solving these equations, a symmetry condition is usually applied at the center of the duct, while no-slip boundary condition is applied to the streamwise velocity at the surface while the temperature takes its surface value. The boundary condition for the particulate concentration at or in close proximity to the surface is not well understood and will be discussed in later chapters.

2.3 Thermophoretic Mass-Transfer Coefficient

In heat transfer problems, the effectiveness of heat transfer is described by the heat transfer conductance h. Similarly, the efficiency of thermophoretic mass transfer can be expressed via a mass transfer conductance $\hbar$. Analogous to the heat transfer case, we equate the mass flux with the product of the conductance and the driving force through a model equation. In this case, the particulate mass flux is driven primarily by a temperature difference. If a model equation is proposed in the simple form: $J = \hbar(T_m - T_s)$, where T_m and T_s are the mixed-mean and surface temperatures respectively, and equated to the surface thermophoretic flux

$$J = -K_{th}\nu \frac{c}{T}\frac{\partial T}{\partial r}\bigg|_{r=R} \tag{2.12}$$

the mass-transfer conductance $\hbar$ would depend explicitly on the surface values of c and T and only indirectly on the temperature field. Since it is the role of the flow and temperature fields on conductance that are of most relevance to a coefficient that measures the effectiveness of mass transport, we redefine $\hbar$ in the model equation as $\hbar c_m/T_s$, where c_m is the mixed-mean particle concentration. This modified conductance represents the effectiveness of mass transport without the explicit and obvious effect of T at the surface, and uses c_m in preference

to c_s, as it is more usual for c_m to be known in typical engineering analyses. If the surface mass flux in the revised model equation:

$$J = \frac{\hbar c_m}{T_s}(T_m - T_s) \tag{2.13}$$

is then assumed to be equal to the thermophoretic mass flux in Eq 2.12, the thermophoretic mass transfer conductance $\hbar$ would be:

$$\hbar = -K_{th}\nu \frac{c_s}{c_m} \frac{\partial T/\partial r|_{r=R}}{(T_s - T_m)} \tag{2.14}$$

or as the dimensionless mass-transfer number:

$$\frac{\hbar R}{K_{th}\nu} = \frac{c_s}{c_m} \frac{R\partial T/\partial r|_{r=R}}{(T_s - T_m)} \quad \text{in the model equation} \quad J = \frac{\hbar c_m}{T_s}(T_m - T_s) \tag{2.15}$$

If we recognize that $R\partial T/\partial r|_{r=R}/(T_s - T_m)$ is half the heat-transfer Nusselt number Nu, we can rewrite the dimensionless mass-transfer number and the model equation for surface mass flux as

$$\mathrm{Sh}_{th} = \frac{\hbar D}{K_{th}\nu} = \mathrm{Nu}\,\frac{c_\delta}{c_m} \qquad \text{with} \qquad J_r = \mathrm{Sh}_{th}\left[\frac{K_{th}\nu}{D}\right]\frac{c_m}{T_s}\,(T_m - T_s) \tag{2.16}$$

where we define Sh_{th} as the thermophoretic Sherwood number. Larger values of $\hbar$ correspond to greater thermophoretic mass transfer for a given temperature difference, and so a greater effectiveness of mass transfer or particulate deposition. In this final form of our model equation:

i) $T_m - T_s$ provides the driving force for thermophoretic mass transfer;

ii) Sh_{th} describes the effectiveness of the flow in promoting thermophoretic mass transfer, by convective enhancement of both the normalized surface temperature gradient and the particle concentration at the edge of the diffusion sublayer relative to its bulk value;

iii) $K_{th}\nu/D$ describes physical and thermophysical properties of the particles, the gas and the duct; and

iv) c_s/T_s describes the explicit effects of the surface particle concentration and the surface temperature on mass transfer. The ratio of surface to bulk particle concentration c_s/c_m has no physical meaning but makes it possible to deal with bulk concentration in the model equation (Eq 2.16) instead of near surface concentration, which is more convenient. It is noticeable that in other problems c_s/c_m might change, i.e. in a boundary layer c_s/c_∞ should be used instead of c_s/c_m, where c_∞ is the concentration far from the surface.

In typical applications, surface and bulk temperatures and the bulk concentration are known. The Nusselt number can then be found from convective heat transfer analyses. The principal difficulty in using the proposed model equation lies in determining c_s from c_m by solution of the particle transport equation. In the following chapter, it is shown how this mass-transfer coefficient is used to characterize thermophoretic mass transfer in pipe flow.

Chapter 3

Thermophoresis in Steady Laminar Flows

In this chapter, new solutions are given for the thermophoretic particulate transport equations for two problems. In Section 1, a numerical method is employed to determine the velocity, temperature and particle concentration fields by solving the governing equations for the case of developing laminar flow in a constant-wall-temperature tube. The governing equations are the conservation of mass, momentum, energy and particulate transport equations and they are solved for the case of fully compressible flow in both the entrance and fully developed zones of constant-wall-temperature tube flow. The numerical results are also in good agreement with available experimental data. In Section 2, the particulate transport equation is solved analytically for the simple case of fully developed laminar flow in a constant-wall-temperature tube. The solution is based on the method of series and the results compare well with experimental data.

3.1 Numerical Solution

In this section, a numerical solution is presented for the entrance zone of a circularly symmetric tube, in which the effects of compressibility, temperature-dependence of properties, the entrance zone are considered.

3.1.1 Governing Equations

The governing equations are the Navier-Stokes and the energy equation:

$$\frac{\partial U}{\partial t} + \frac{\partial A}{\partial z} + \frac{\partial B}{\partial r} + \frac{1}{r}\frac{\partial C}{\partial \theta} + \frac{1}{r}D = 0 \tag{3.1}$$

$$U = \begin{bmatrix} \rho \\ \rho u \\ \rho v \\ \rho w \\ \rho E \end{bmatrix} \tag{3.2}$$

$$A = \begin{bmatrix} \rho u \\ \rho uu + p - \tau_{zz} \\ \rho uv - \tau_{rz} \\ \rho uw - \tau_{\theta z} \\ \rho uH + q_z - u\tau_{zz} - v\tau_{rz} - w\tau_{\theta z} \end{bmatrix} \quad B = \begin{bmatrix} \rho v \\ \rho uv - \tau_{rz} \\ \rho vv + p - \tau_{rr} \\ \rho vw - \tau_{\theta r} \\ \rho vH + q_r - u\tau_{rz} - v\tau_{rr} - w\tau_{\theta r} \end{bmatrix}$$

$$C = \begin{bmatrix} \rho w \\ \rho uw - \tau_{\theta z} \\ \rho vw - \tau_{\theta r} \\ \rho ww + p - \tau_{\theta\theta} \\ \rho wH + q_\theta - u\tau_{\theta z} - v\tau_{\theta r} - w\tau_{\theta\theta} \end{bmatrix} \quad D = \begin{bmatrix} \rho v \\ \rho uv - \tau_{rz} \\ \rho vv - \rho ww - \tau_{rr} + \tau_{\theta\theta} \\ 2\rho vw - 2\tau_{\theta r} \\ \rho vH + q_r - u\tau_{rz} - v\tau_{rr} - w\tau_{\theta r} \end{bmatrix}$$

where the total energy is defined as $E = T/[\gamma(\gamma-1)M^2] + 1/2u_iu_i$ with $\gamma = 1.4$, and the total enthalpy is $H = E + p/\rho$. The corresponding stress tensor and heat flux vector components are

$$\tau_{zz} = \frac{2\mu}{3Re}\left[2\frac{\partial u}{\partial z} - \frac{\partial v}{\partial r} - \frac{1}{r}\left(\frac{\partial w}{\partial \theta} + v\right)\right] \tag{3.3}$$

$$\tau_{rr} = \frac{2\mu}{3Re}\left[-\frac{\partial u}{\partial z} + 2\frac{\partial v}{\partial r} - \frac{1}{r}\left(\frac{\partial w}{\partial \theta} + v\right)\right] \tag{3.4}$$

$$\tau_{\theta\theta} = \frac{2\mu}{3Re}\left[-\frac{\partial u}{\partial z} - \frac{\partial v}{\partial r} + 2\frac{1}{r}\left(\frac{\partial w}{\partial \theta} + v\right)\right] \tag{3.5}$$

$$\tau_{rz} = \frac{\mu}{Re}\left[\frac{\partial u}{\partial r} + \frac{\partial v}{\partial z}\right] \tag{3.6}$$

$$\tau_{\theta z} = \frac{\mu}{Re}\left[\frac{\partial w}{\partial z} + \frac{1}{r}\frac{\partial u}{\partial \theta}\right] \tag{3.7}$$

$$\tau_{\theta r} = \frac{\mu}{Re}\left[\frac{1}{r}\left(\frac{\partial v}{\partial \theta} - w\right) + \frac{\partial w}{\partial r}\right] \tag{3.8}$$

$$q_z = \frac{-\mu}{\mathrm{Pe}(\gamma-1)M^2}\frac{\partial T}{\partial z} \tag{3.9}$$

$$q_r = \frac{-\mu}{\mathrm{Pe}(\gamma-1)M^2}\frac{\partial T}{\partial r} \tag{3.10}$$

$$q_\theta = \frac{-\mu}{\mathrm{Pe}(\gamma-1)M^2}\frac{1}{r}\frac{\partial T}{\partial \theta} \tag{3.11}$$

where the Peclet number is assumed to be constant, the molecular viscosity μ depends on absolute temperature raised to some power, and the ideal gas equation of state is used to determine the pressure [111]. The governing equations Eq. 3.1 were discretized using a finite difference method (FDM). A (5,4) Runge-Kutta scheme was used for the temporal discretization (see [10] for more details), and a computer code was written in Fortran to solve the discretized form of the governing equations.

After calculating the temperature and velocity fields, the particle transport was solved using a similar code. As the flow is axisymmetric, the particulate transport equation may be simplified as

$$\begin{aligned}\frac{\partial \rho c}{\partial t} + \frac{\partial \rho c u}{\partial z} + \frac{1}{r}\frac{\partial \rho c r v}{\partial r} = & \frac{\partial}{\partial z}\left(\rho c D \frac{\partial c}{\partial z} + \rho c K_{th} \nu \frac{\partial Ln(T)}{\partial z}\right) \\ & + \frac{1}{r}\frac{\partial}{\partial r}\left(r\left(\rho c D \frac{\partial c}{\partial r} + \rho c K_{th} \nu \frac{\partial Ln(T)}{\partial r}\right)\right)\end{aligned} \tag{3.12}$$

Eq. 3.12 is sufficiently well-behaved that it can be solved by a Eulerian time integration scheme in a simple uniform grid. As the time required for the numerical solution of Eq. 3.12 was much shorter than the time necessary for solving velocity and temperature fields, the steady state values for the velocity and temperature were saved in a file and used by the particulate transport solver.

The boundary conditions of no-slip velocity and constant temperature were imposed at the walls, while the inflow and outflow conditions were imposed according to Rudy and Strikwerda's non-reflecting scheme [110]. The Neumann and the symmetry boundary conditions were imposed at the walls and the centerline respectively. The inflow concentration was assumed to be constant and uniform, while the outflow concentration was obtained via extrapolation.

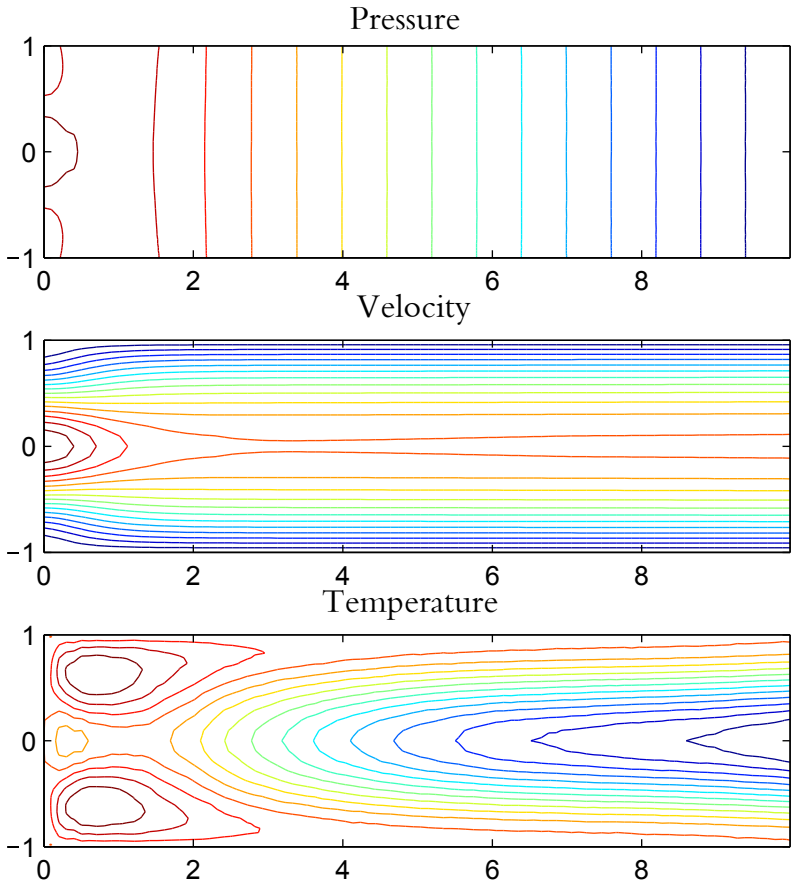

Figure 3.1: Pressure, velocity and temperature contours at steady state for the Poiseuille flow.

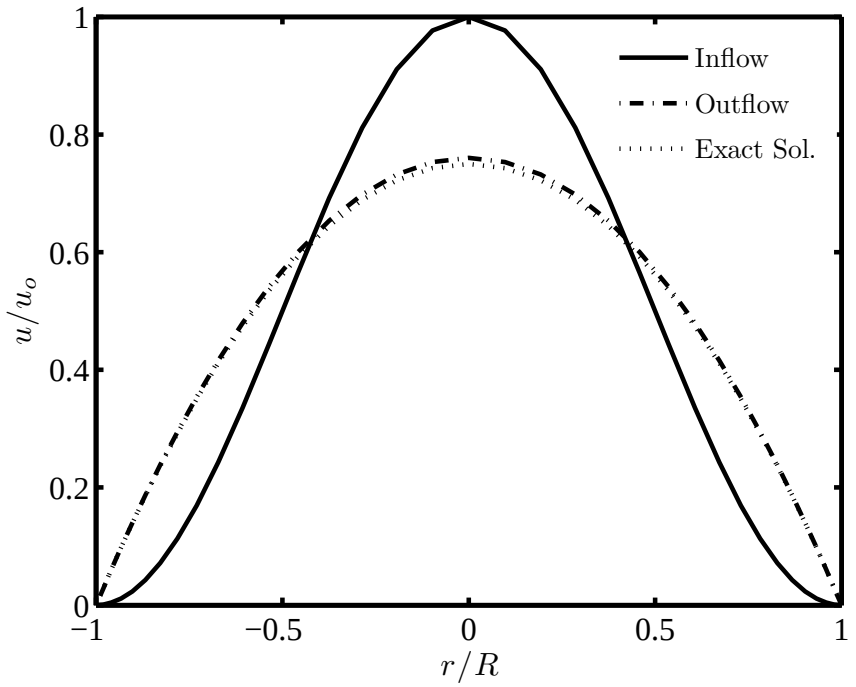

Figure 3.2: Velocity profiles along the tube(x/L=0.0,.33,.66,1.0).

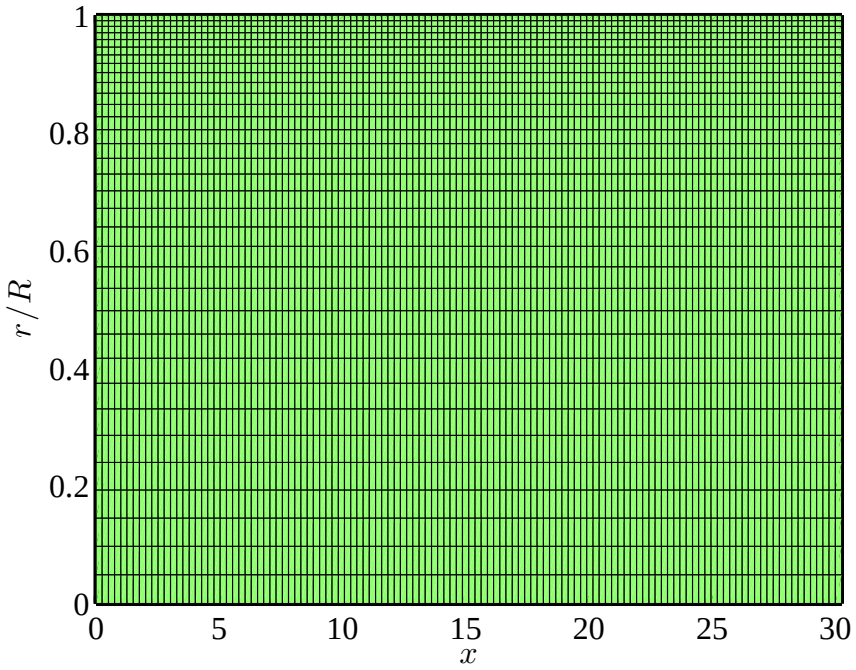

Figure 3.3: Schematic of the computational grid used for calculating the flow field.

3.1.2 Results and Discussion

In order to validate the numerical solver that was developed, a benchmark problem was solved. The chosen problem was low Reynolds number Poiseuille flow with isothermal no-slip walls, which has been studied by Poinsot and Lele [102]. In this problem, the Reynolds number based on the half width of the channel was set to 15, the inflow velocity was cosinoidal while the inflow and the wall temperatures were identical (the interested reader is referred to Poinsot and Lele's article [102] for more details on this Poiseuille problem). Convergence occured when the outflow mass flux approaches the inflow value, and the corresponding pressure, velocity and temperature contours are shown in Fig. 3.1. They compare well with Poinsot and Lele's results. The velocity profiles calculated at inlet and outlet are displayed in Fig. 3.2 and are also similar to those of Poinsot and Lele, and almost identical to the exact solution [102].

After validation, this computer code was used to solve the problem of flow and heat and mass transfer in the entrance zone of a constant-wall-temperature tube. The problem was assumed to be axisymmetric, which eliminated some of the terms in Eq. 3.1. The grid chosen was uniform along the tube, while grid compression was applied in the radial direction. A 2-D grid 121×35 was found to yield good results up to Reynolds numbers of 300, and is shown in Fig. 3.3. As most of the heat transfer and thermal mass transfer occurs in the entrance zone, the length of the domain was chosen so that the thermal developing zone could be captured completely. The code developed was capable of calculating the velocity and temperature fields for Reynolds number of up to 4000 in Cartesian and up to 1400 in cylindrical coordinates. The velocity and temperature fields for a Reynolds number of 300 are shown below.

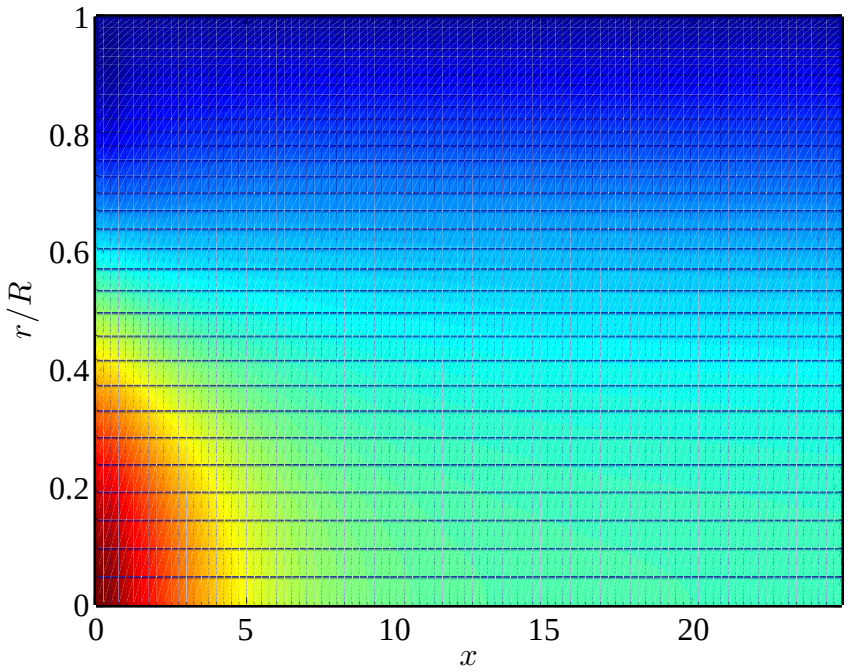

Figure 3.4: Velocity field in a tube at Reynolds number of 300-based on the hydrodynamic diameter of the tube.

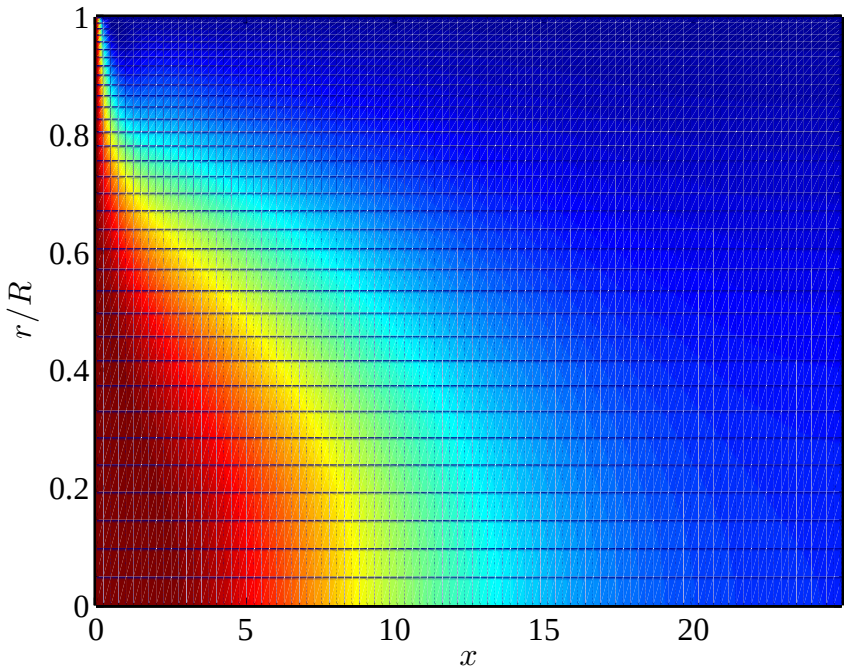

Figure 3.5: Temperature field in a tube at a Reynolds number of 300 based on the hydrodynamic diameter of the tube.

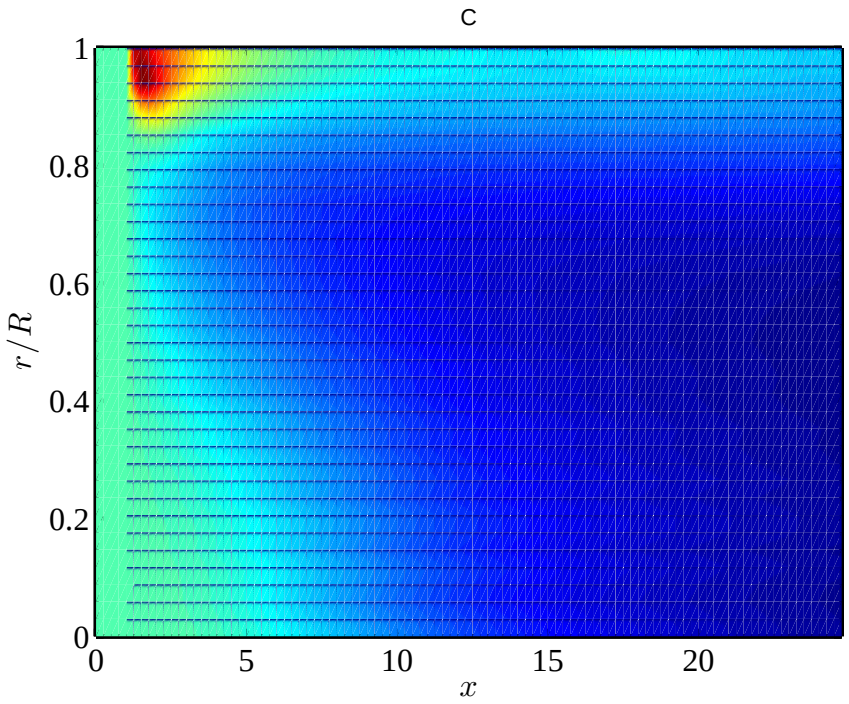

Figure 3.6: Concentration field in a tube at Reynolds number of 300-based on the hydrodynamic diameter of the tube.

The calculated concentration field for the Reynolds number of 300 is shown in Fig. 3.6, from which the mean concentration $c_m(x)$ and the deposition efficiency $\eta(x)$ were calculated. The transport and deposition of sub-micron particles in entrance zones has also been determined by others. Montassier et al. carried out a comprehensive study on the thermophoretic particle deposition in laminar tube flow [91], including a series of experiments and observed that his measurements were in agreement with the theoretical predictions of Stratmann [122] for sub-micron particles, when employing Talbot's formula for K_{th}. Based on these observations, Montassier developed an empirical relation for the deposition efficiency along the tube $\eta(x)$.

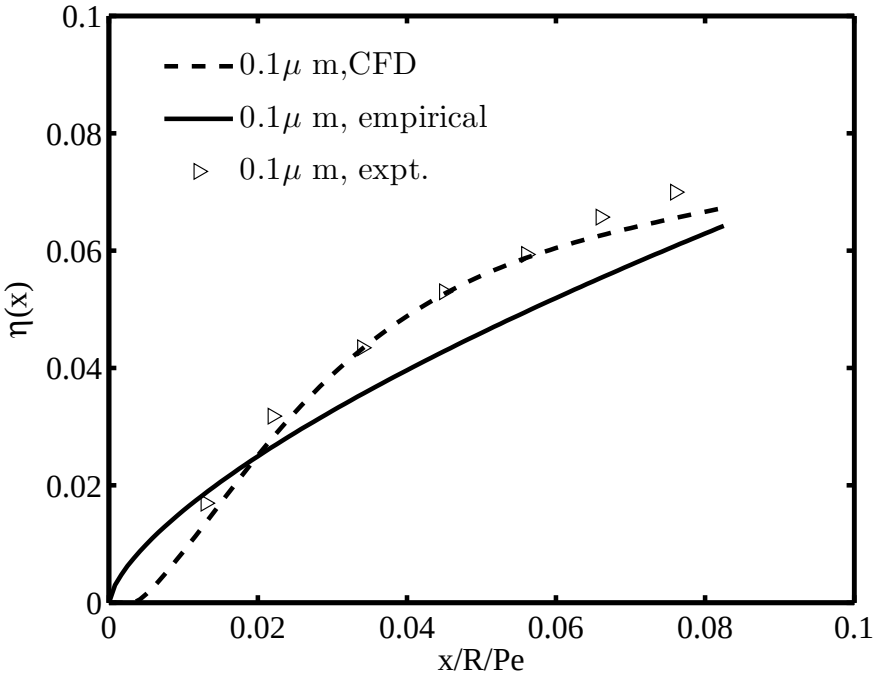

Figure 3.7: Measured deposition efficiencies $\eta(x)$, predicted values based on Eq. 3.13 and the results obtained by numerical solution for particles of $0.1\mu m$ diameter at Re$\simeq$300.

$$\eta(x) = \begin{cases} 3.2\dfrac{\mathrm{Pr}K_{th}}{1+\theta^*}\left(1+\dfrac{1-\mathrm{Pr}K_{th}}{1+\theta^*}\right)\left(\dfrac{x}{R\mathrm{Pe}}\right)^{2/3} & \mathrm{Kn}\geq 0.2,\ \left(\dfrac{x}{R\mathrm{Pe}}\right)<0.15 \\ 1.7\dfrac{\mathrm{Pr}K_{th}}{1+\theta^*}\left(1+\dfrac{1-\mathrm{Pr}K_{th}}{1+\theta^*}\right)\left(\dfrac{x}{R\mathrm{Pe}}\right)^{0.58} & \mathrm{Kn}\leq 0.2,\ \left(\dfrac{x}{R\mathrm{Pe}}\right)<0.15 \end{cases} \tag{3.13}$$

The values of $\eta(x)$ determined by numerical computation, Eq. 3.13 and Montassier's experimental data are shown along the tube (Fig. 3.7). The experiments were carried out in a tube of inner diameter of 2 cm with an air flow of 10^{-4} kg/s containing particles of sodium salt of fluorescein, which corresponded to Re and K_{th} of approximately 300 and 0.5 respectively (the reader is referred to Montassier's article for more details on the experiments [91]). The discrepancy between the computational results and the experimental data is negligible, and Eq. 3.13 is also in good agreement with the experimental measurements. In the current

problem, it is seen that the thermophoretic conductance values are quite different to those obtained in Section. 3.2.2. This discrepancy may be explained based on the fact that in the former case, the temperature and concentration profiles were fully-developed, while in the latter, the mass transfer in the thermal entrance zone is far from fully-developed.

A numerical simulation at Reynolds number of 30 was then carried out for longer tube lengths, when the flow was almost fully developed and the Nusselt number approached a steady value. It was assumed that the fluid viscosity was a power function of temperature as $\frac{\mu}{\mu_0} = \left(\frac{T}{T_0}\right)^{0.7}$, where μ_0 and T_0 are the reference viscosity and temperature. As the flow properties depend on the flow temperature, the Nusselt number was calculated at different temperature ratios and has been compared with the Nusselt number in the case of constant properties Nu_{cp}, where the flow properties are independent of the flow temperature (see Table. 3.1). It is evident that the discrepancy between Nusselt numbers because of temperature dependent properties is very small, making the constant property assumption reasonable.

Table 3.1: Studying the effect of variable properties on Nusselt number

T_s/T_o	Nu_{cp}	Nu	$\mathrm{Nu}/\mathrm{Nu}_{cp}$	Error(%)
0.6	3.52	3.65	1.04	4%
0.7	3.48	3.55	1.02	2%
0.8	3.47	3.51	1.01	1%
0.9	3.45	3.48	1.01	1%
0.95	3.48	3.5	1.01	1%

3.2 Analytical Solution

In this section the transport equations have been simplified considerably so they can be solved by the method of series. The simplifying assumptions and the corresponding analytical

solutions for several typical problems will be discussed in the following.

3.2.1 Effects of Temperature-Dependent Properties

Exact analytical solutions exist for the fully-developed velocity field in laminar pipe flows of constant-density, constant-viscosity Newtonian fluids, and the companion fully-developed temperature field for uniform wall temperature when k and c_p are constant. In gas flows with thermophoresis, in which the temperature gradients are necessarily large, the gas density, viscosity and Prandtl number can vary significantly with surface-normal position. However, the extent to which these property variations affect the resulting velocity and temperature profiles in any particular flow is not clearly understood. We therefore carried out numerical calculations of the Graetz thermal entry-length problem by solving the compressible axisymmetric equations of motion and thermal energy (Eqs. 3.1–3.2), using an ideal gas equation to describe the air density, a Sutherland model for its temperature-dependent viscosity, and a linear Prandtl number dependence on temperature.

The computations were carried out at $\mathrm{Re} = 30$ on a compressed mesh with 35 points in the radial and 121 points in the axial direction ($x/R = 5$), when the ratio of surface-to-inflow temperature (in Kelvin) was set to 0.6 and 0.8. The resulting profiles of temperature and velocity are plotted in Figs. 3.8 and 3.9 and appear to be in very close agreement with the constant-property analytical solutions. Computations of the Nusselt number in this laminar pipe flow with temperature-dependent air properties differed from its constant-property value by less than 4% for $T_s/T_o > 0.6$ and by less than 1% for $T_s/T_o > 0.8$. These results are consistent with the observation of Kays et al. [60] that, as viscosity and conductivity scale with $T^{0.8}$ and density is inversely proportional to T, the temperature dependences of these properties almost compensate for one another, with the result that constant-property

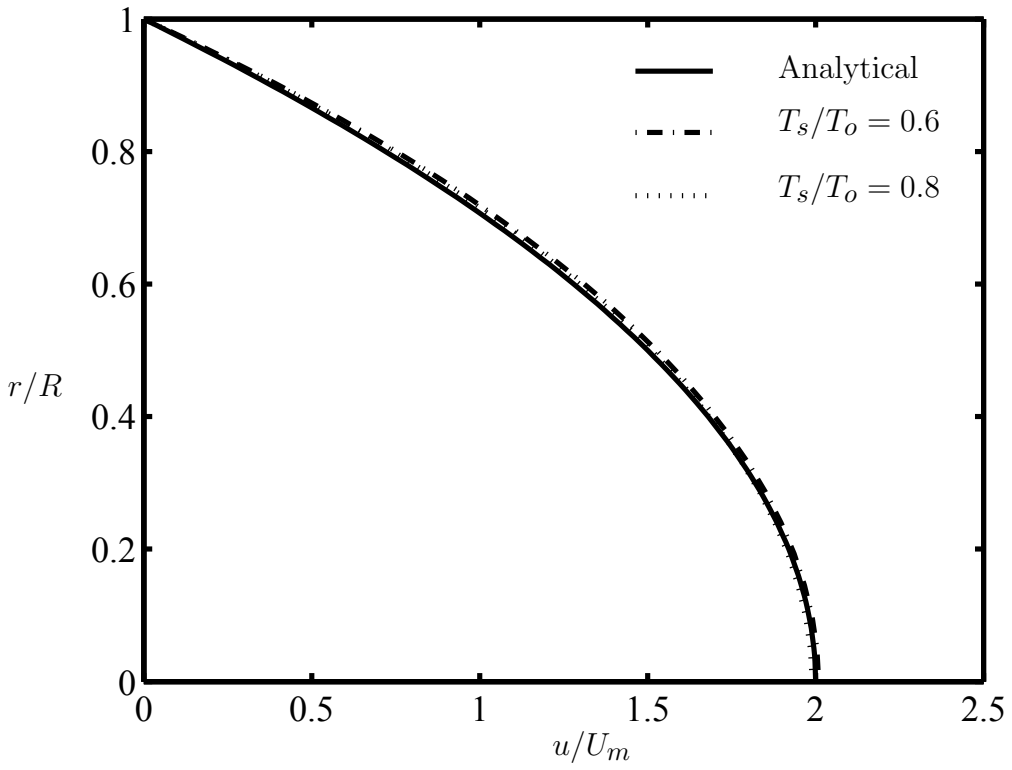

Figure 3.8: Comparison of velocity profiles computed in compressible laminar pipe flows with temperature-dependent properties at $T_s/T_o = 0.6$ and 0.8 with the analytical Poiseuille-flow solution.

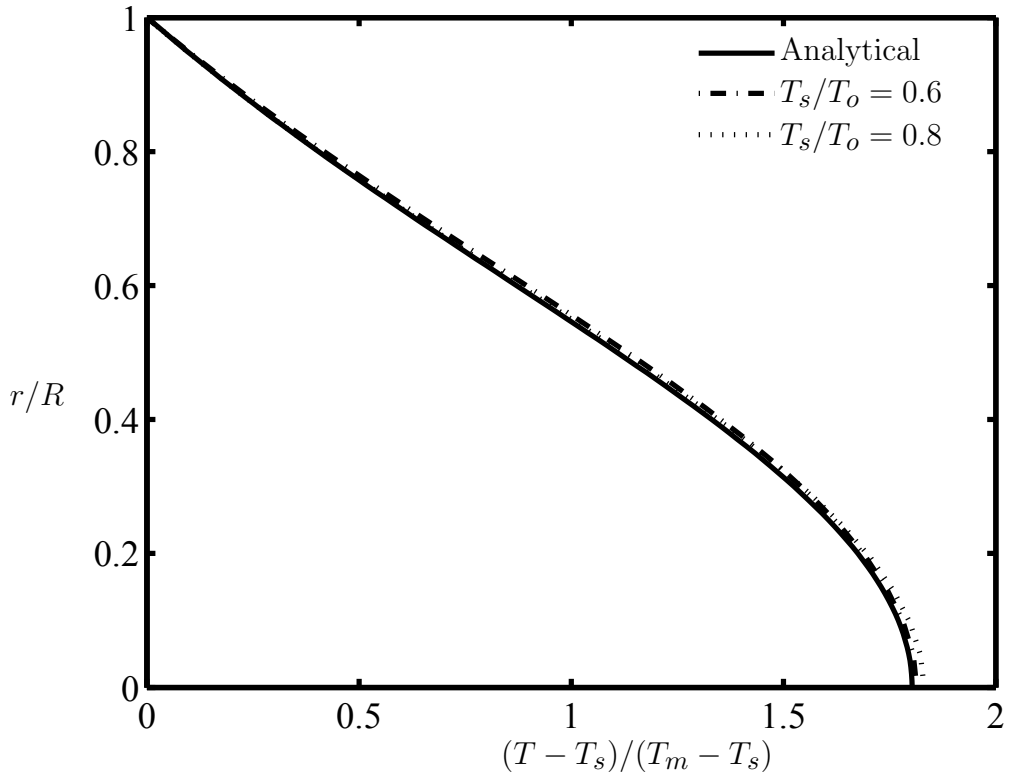

Figure 3.9: Comparison of temperature profiles computed in compressible laminar pipe flows with temperature-dependent properties at $T_s/T_o = 0.6$ and 0.8 with the analytical solution of Shokouhmand and Hooman [116].

solutions can provide quite accurate representations of gas flows with temperature-dependent properties, even when there are large temperature variations across a flow [60].

In the following sections the particle transport equation for the hydrodynamically and thermally fully-developed incompressible tube flow, channel flow and a plate-to-plate precipitator have been solved using series solution. Although the measurement of deposition efficiency is quite convenient, there is almost no experimental data on the shape of concentration profiles in tubes so the full development of the concentration profiles is not well understood. In the following sections, two plausible forms of a fully-developed concentration field are proposed, both of which provide a basis for the particle transport equations to be simplified and solved. These solutions are discussed in the next two sections.

Concentration profiles are considered to be fully-developed when the non-dimensional concentration θ stays invariant in the longitudinal direction. Two possible forms for θ are:

a) $\frac{c_s - c}{c_s - c_m}$, and

b) $\frac{c}{c_m}$

The first form is analogous to that of fully-developed heat transfer, in which the heat flux is driven by a temperature gradient. It is clearly the appropriate form for fully developed particle transport dominated by molecular diffusion, in which case the particle flux scales on the concentration gradient through Fick's law. However, in cases when thermophoresis is dominant, the particle flux depends linearly on the absolute value of particle concentration, and not its gradient, and so a scaling of absolute concentration ratios is proposed. For the first of these proposed conditions for full development of the concentration field, the transport equations for pipe flow are solved based on the assumption of $\theta = (c_s - c)/(c_s - c_m)$. The second fully developed assumption of $\theta = c/c_m$ is then used to solve the pipe flow, channel flow and plate-to-plate precipitator flows, with a series solution. The corresponding results originated from both assumptions will be discussed in the following sections.

3.2.2 Fully-Developed Pipe Flow($\theta = (c_s - c)/(c_s - c_m)$)

We consider the problem of thermophoretic transport of particles from a hot gas to a cold, uniform-temperature wall when velocity and temperature profiles in the outer region can be approximated as their constant-property, fully-developed forms, as discussed earlier. The Nusselt number for this flow is 3.657 [60]. The velocity and temperature profiles can be expressed in terms of the average velocity U_m, the mixed-mean temperature $T_m(x)$ and

$r^+ = r/R$, as

$$u = 2U_m(1 - r^{+2}) \tag{3.14}$$

where U_m is the average velocity and $r^+ = r/R$, and when Brownian diffusion is much less important than thermophoresis, the corresponding particle transport equation may be written as:

$$2U_m(1 - r^{+2}) \left(\frac{\partial c}{\partial x}\right) = \frac{K_{th}\nu}{R^2 r^+} \frac{\partial}{\partial r^+} \left(\frac{c r^+}{T} \frac{\partial T}{\partial r^+}\right) \tag{3.15}$$

The fully-developed temperature profile in this flow has been calculated by Shokouhmand and Hooman [116] as the series solution:

$$\frac{T - T_s}{T_m - T_s} \approx 1.8030 - 3.2966 r^{+2} + 2.3310 r^{+4} - 1.1433 r^{+6} + \ldots = f(r^+) \tag{3.16}$$

We now develop a solution for the concentration field when thermophoretic particle transport takes place in this flows. The presence of thermophoresis implies that significant temperature gradients exist, in which case the flow would not be one with constant properties. The validity of this assumption was discussed in the previous section. The local mixed-mean temperature $T_m(x)$ in Eq. 3.16 may be evaluated by making use of an overall energy balance in the x-direction, from the pipe entrance at $x = 0$, where the fluid temperature is T_o, to any arbitrary downstream location x. Neglecting the thermal entrance effects, the heat-transfer coefficient is constant along the tube, and it is found by integration of the energy balance that

$$\frac{T_m(x) - T_s}{T_o - T_s} = \exp\left(-2\text{Nu } x/[\text{Pe}R]\right) \tag{3.17}$$

where Pe is the Peclet number Pe=$U_m D/\beta$ referenced to the pipe diameter D. Eqs. 3.16 and 3.17 can then be substituted into Eq. 3.15 so that its temperature terms are determined. An

overall particle mass balance over a section through the pipe of differential length dx yields the result

$$\frac{dc_m(x)}{dx} = -\frac{K_{th}\nu}{U_m R^2}\frac{c_s}{T_s}\mathrm{Nu}(T_m - T_s) \tag{3.18}$$

and when this result is substituted in Eq. 3.15, U_m is cancelled and the particulate transport equation is simplified as:

$$-2\mathrm{Nu}c_s\left(r^+ - r^{+3}\right)\frac{\partial c}{\partial x} = \frac{dc_m}{dx}\frac{\partial}{\partial r^+}\left(\frac{r^+ c f'(r^+)}{1 + fe^{-\beta x[T_o/T_s - 1]}}\right) \tag{3.19}$$

where f' is the derivative of f in Eq. 3.16 and $\beta = 2\mathrm{Nu}/(\mathrm{Pe}R)$. In order to solve this particle transport equation, a simplifying assumption about the $\partial c/\partial x$ term is necessary. A dimensionless concentration parameter θ is defined as,

$$\theta = \frac{c_s - c}{c_s - c_m} \tag{3.20}$$

and $\partial\theta/\partial x = 0$ under fully developed conditions. By differentiating Eq. 3.20, it may be seen that a condition for the existence of a fully developed concentration profile is

$$\frac{\partial c}{\partial x} = \frac{dc_m}{dx} = \frac{dc_s}{dx} = g(x) \tag{3.21}$$

where $g(x)$ is any function of x. This condition also implies that $c_s(x) - c_m(x)$ =constant. Numerical simulations of this entrance-length problem show that the concentration profiles reach full development at $x/(\mathrm{Pe}R) \simeq 0.1$. It is important to distinguish this condition for a fully-developed concentration profile from the analogous constant-heat-flux condition for a

fully-developed temperature profile:

$$\frac{\partial T}{\partial x} = \frac{dT_m}{dx} = \frac{dT_s}{dx} = \text{constant} \tag{3.22}$$

This more restrictive requirement of the temperature gradient taking a constant value is a consequence of the overall energy balance and the constant-heat-flux condition and does not apply to the concentration field.

When the additional condition of a fully-developed concentration profile of Eq. 3.21 is applied to Eq. 3.19, it may be integrated once, with the boundary conditions that c remains finite and the temperature is symmetric about $r^+ = 0$, the result is

$$\frac{c}{c_s} = \text{Nu}\left(1 + f(r^+)e^{-\beta x}\left[\frac{T_o}{T_s} - 1\right]\right)\frac{\frac{1}{2}r^{+3} - r^+}{f'(r^+)} \tag{3.23}$$

The concentration ratio c/c_s may then be determined at any x-location by expansion of Eq. 3.23 and takes the form of the analytical series solution:

$$\begin{aligned}\frac{c}{c_s} \;=\; \text{Nu}\Bigg(&0.1516 + 0.2734e^{-\beta x}\left[\frac{T_o}{T_s} - 1\right] + \left\{-0.2500 + 0.1386e^{-\beta x}\left[\frac{T_o}{T_s} - 1\right]\right\} r^{+2} \\ &+ \left\{0.0382 - 0.0345e^{-\beta x}\left[\frac{T_o}{T_s} - 1\right]\right\} r^{+4} + \left\{-0.0171 - 0.0072e^{-\beta x}\left[\frac{T_o}{T_s} - 1\right]\right\} r^{+6} \\ &+ \left\{-0.02316 + 0.005410e^{-\beta x}\left[\frac{T_o}{T_s} - 1\right]\right\} r^{+8} + \ldots\Bigg)\end{aligned} \tag{3.24}$$

Thus the concentration ratio c/c_s evolves as a function of x even though the shape of the concentration profile θ is assumed to have completed its development. Moreover, this ratio is independent of the thermophoretic and viscosity coefficients and is therefore invariant with the size and kind of particle, providing it is one-way coupled with the flow. The ratio c_m/c_s

may be found from the definition of c_m,as

$$\frac{c_m}{c_s} = 4\int_0^1 (r^+ - r^{+3})\frac{c}{c_s}\,dr^+ = \mathrm{Nu}\left[0.20044 + 0.18462e^{-\beta x}(T_o/T_s - 1)\right] \tag{3.25}$$

where the coefficients have been determined from terms up to r^{+20}, for which convergence was achieved to the 5th decimal place. When Nu is set to 3.657 and x is sufficiently large, c_s/c_m approaches 1.364. This asymptotic result tells us that the surface particle concentration is significantly larger than the mixed-mean value. It is important to note that this calculation of c_s does not include any effect of the Fickian diffusion. Therefore it would be expected to describe the edge of a very thin diffusion layer at the surface, rather than at the surface itself. It is this aspect of this solution that explains its apparent contradiction with the $c_s = 0$ boundary condition applied at the surface in other studies. It also implies that the simplification that is sometimes made of a flat concentration profile underestimates deposition in laminar flows. It is noteworthy that, in this determination of $c(x; r^+)/c_s(x)$, no boundary condition was applied at the surface of the tube. As Eq. 3.15 is a first order PDE of concentration only one boundary condition is required, which was the symmetry condition in the centreline in this case. The gradient of the concentration profile at the surface can be found by differentiation of Eq. 3.24 to be

$$\frac{\partial}{\partial r^+}\left(\frac{c}{c_s}\right)\bigg|_{r^+=1} = -\mathrm{Nu}\left[0.02935 + 0.4862e^{-\beta x}(T_o/T_s - 1)\right] \tag{3.26}$$

The results of this section may be used to explore the dependence of the dimensionless mass-transfer conductance $\hbar D/(K_{th}\nu) = (c_s/c_m)\mathrm{Nu}$ on Pe, x/R and T_o/T_s.

3.2.2.1 Development of the Sherwood Number

For the problem of particulate transport in axisymmetric pipe flow with fully developed velocity and temperature profiles, with a hot fluid and a cold constant-temperature pipe surface, the Nusselt number reaches its asymptotic value of 3.657 at approximately $x/(\mathrm{Pe}R) = 0.1$ [60]. When the concentration profile is fully developed, the mass-transfer conductance may be written in dimensionless form, using the pipe diameter as its length-scale, as $\hbar D/(K_{th}\nu) = (c_s/c_m)\mathrm{Nu}$ or

$$\mathrm{Sh}_{th} = \frac{\hbar D}{K_{th}\nu} = \frac{c_s}{c_m}\mathrm{Nu} = \frac{1}{0.20044 + 0.18462e^{-\beta x}(T_o/T_s - 1)} \tag{3.27}$$

Thus, when the concentration profile is fully developed and $x = (\mathrm{Pe}R) > 0.1$, this conductance depends only on the axial dependence of the concentration ratio c_s/c_m. The dimensionless conductance is plotted against $x/(\mathrm{Pe}R)$ in Fig. 3.10, when the ratio of in flow temperature to wall temperature T_o/T_s (in degrees K) takes the values: 1.25; 1.5; 1.75 and 2.0. From this figure, it appears that the conductances at each temperature ratio tend towards an asymptotic value of 5.0 which is reached after a development length of roughly $0.6\mathrm{Pe}R$, when c_s/c_m reaches a fully-developed value of 1.364. Since this concentration entrance length is about six times longer than the thermal development length, the assumption in the preceding analysis of a fully-developed temperature field for the entire flow appears to be a reasonable one. Within the concentration-ratio development region ($x/(\mathrm{Pe}R) < 0.6$), there is a significant effect of the ratio T_o/T_s on the mass-transfer conductance, with higher temperature ratios corresponding to lower conductances at any given axial position. This effect is a consequence of the non-linear temperature dependence of the thermophoresis term in Eq. 3.15 and the x-dependent temperature field of Eq. 3.17. Complete (numerical) so-

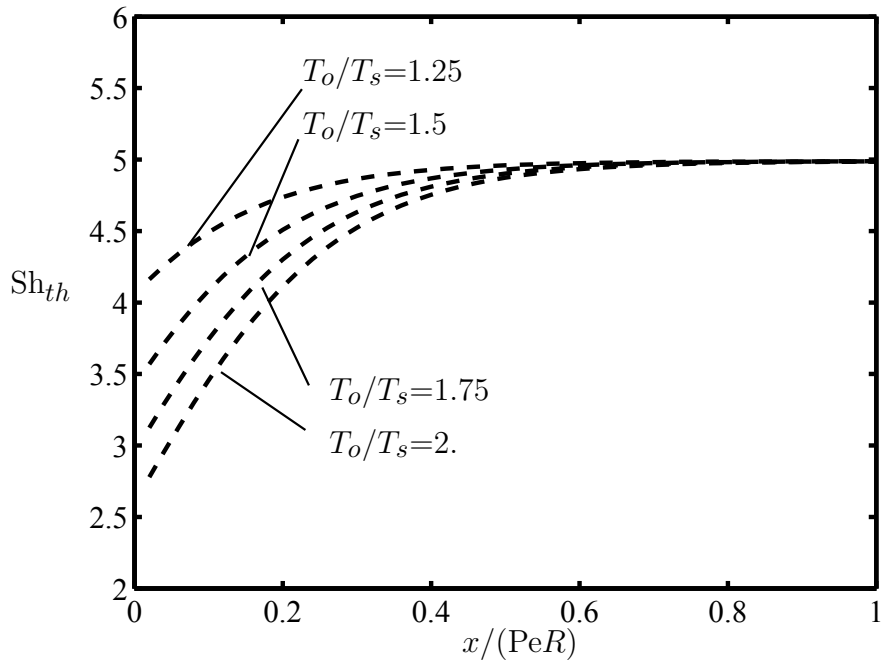

Figure 3.10: Dimensionless mass-transfer conductance $\mathrm{Sh}_{th} = (c_s/c_m)\mathrm{Nu}$ plotted against $x/(\mathrm{Pe}R)$ when T_o/T_s=1.25; 1.5; 1.75; and 2.0.

lutions for the dimensionless mass-transfer conductance in the thermally developing region ($x/(\mathrm{Pe}R) < 0.1$) should, presumably, provide a smooth continuation of each plotted conductance curve to its value at $x = 0$ for whatever in flow conditions might be specified. However, regardless of the inflow conditions, the dimensionless mass-transfer conductance reaches its fully developed value of 5.0 when $c_s/c_m = 1.364$.

3.2.2.2 Development of the Concentration Profile

The dependence of the dimensionless mass-transfer conductance on the concentration field is $\hbar D/(K_{th}\nu) = (c_s/c_m)\mathrm{Nu}$ and has a region of development shown in Fig. 3.10. It is therefore interesting to see how profiles of the particle concentration behave within this development length and so profiles of c/c_m are plotted against r/R in Fig. 3.11 at several axial locations during development, at a representative temperature ratio of $T_o/T_s = 1.5$.

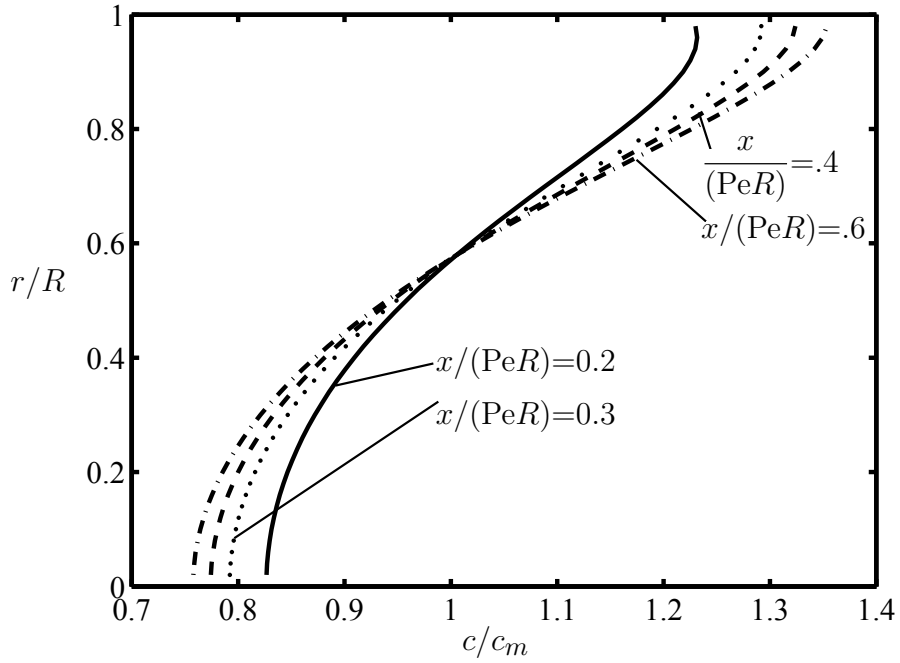

Figure 3.11: Radial profiles of c/c_m plotted at $x/(\mathrm{Pe}R) = 0.2$; 0.3; 0.4 and 0.6, when $T_o/T_s = 1.5$.

It is important to note that while the local ratio c_s/c_m has been found analytically for a thermally and hydraulically developed, particle-laden flow, the absolute value of $c(x;r)$ and the ratio $c(x;r)/c_{mo}$ cannot be found without solving numerically the coupled differential equations of linear momentum, thermal energy, and particle diffusion over a domain from in flow to the x-location of interest. From Fig. 3.11, it can be seen each c/c_m profile takes the shape of a rotated 'S' with the lowest particle concentrations at the pipe center and the highest concentrations at/near the surface. Each profile is flat at the pipe center and almost flat at the surface. The effect of axial development is to steepen the profile, reducing the concentration at the center while increasing it at the surface. In the early stages of development at $x < 0.2\mathrm{Pe}R$, the gradient of the concentration profile is almost zero over a region that extends outward from the surface to roughly $0.9R$. As full development of the concentration profile is reached at $x = 0.6\mathrm{Pe}R$, the concentration gradient at the surface is

not zero but slightly negative.

3.2.2.3 Deposition Efficiency

A small number of experimental studies have been carried out of particle deposition from hot, laminar, particle-laden gas flows to cold pipe walls [107, 91, 123], in which particle transport is characterized in terms of a measured deposition efficiency. This efficiency is defined as the mass flow rate of particles deposited on the wall of the pipe, from the pipe entrance to some downstream location x, divided by the mass flow rate of particles entering the pipe, and can be expressed as

$$\eta(x) = 1 - \frac{c_m(x)}{c_{mo}} \tag{3.28}$$

where c_{mo} is the mixed-mean particulate concentration at the pipe entrance. The ratio $c_m(x)/c_{mo}$ can be determined by integrating from in flow to some arbitrary downstream distance x the overall particulate mass balance for a section of the pipe of differential length dx, which is

$$-U_m R \frac{dc_m(x)}{dx} = 2J \tag{3.29}$$

or, after substitution for the particulate flux at the pipe surface J from Eq. 2.16 and separating variables,

$$\frac{dc_m(x)}{c_m} = -\frac{K_{th}\nu}{U_m R^2} Nu \frac{c_s}{c_m} \left[\frac{T_m(x)}{T_s} - 1\right] dx \tag{3.30}$$

where Nu and c_s/c_m are, in general, functions of x. If constant values of T_s and the surface heat transfer coefficient are assumed for all x, $T_m(x) - T_s$ may be expressed in terms of the

in flow temperature T_o, T_s and x according to Eq. 3.17. Furthermore, if c_s/c_m is taken as its fully-developed value, Eq. 3.30 can be integrated analytically from inflow to some arbitrary downstream distance x and substituted into Eq. 3.28 to yield

$$\eta(x) = 1 - \exp\left\{-\frac{2K_{th}\mathrm{Nu}}{\mathrm{Re}\ R}\left[\frac{T_o}{T_s} - 1\right]\int_0^x \frac{c_s}{c_m} e^{-2\mathrm{Nu}.(\frac{x}{R})/\mathrm{Pe}}\, dx\right\} \tag{3.31}$$

In the case of fully-developed concentration concentration profiles, the corresponding formula for c_s/c_m in Eq. 3.25 may be used and Eq. 3.31 may be integrated analytically from inflow to the arbitrary downstream distance x of the flow to yield

$$\eta(x) = 1 - \left[\frac{1 + 0.9211(T_o/T_s - 1)e^{-2\mathrm{Nu}(\frac{x}{R})/\mathrm{Pe}}}{1 + 0.9211(T_o/T_s - 1)}\right]^{K_{th}\mathrm{Pr}/0.1846\ \mathrm{Nu}} \tag{3.32}$$

As x tends to infinity, corresponding to deposition in long tubes, this efficiency tends towards the asymptotic value of

$$\eta(\infty) = 1 - \left[\frac{1}{1 + 0.9211(T_o/T_s - 1)}\right]^{K_{th}\mathrm{Pr}/0.1846\ \mathrm{Nu}} \tag{3.33}$$

3.2.2.4 Comparison with Experimental Data and Computational Models

The experimental data for deposition efficiency that are most suitable for comparison with theoretical predictions are those of Romay et al. [107] in which hot air seeded with sodium chloride (NaCl) particles (0.1 μm and 0.482 μm diameter) was flowed steadily at Re = 1400 within a 4.9 mm diameter metal pipe, the outer surface of which was cooled by water in the configuration of an annular counter-flow heat exchanger. In these experiments, Romay et al. maintained the inflow temperature of the cooling water at 20^oC while systematically

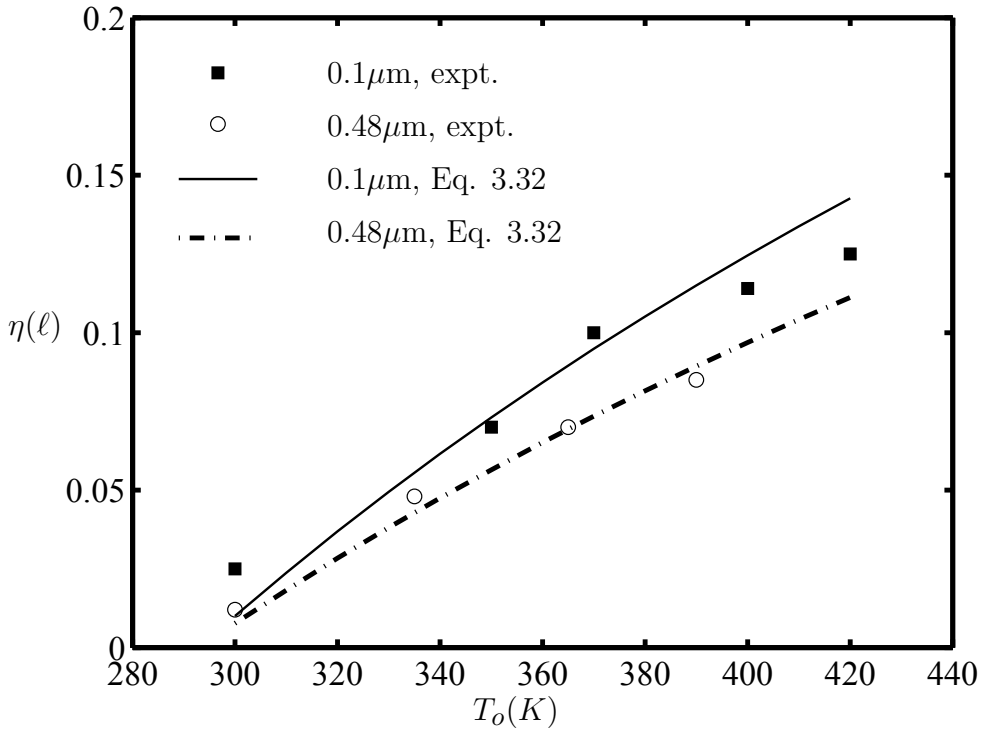

Figure 3.12: Comparison of measured (Romay [107]) and predicted (Eq. 3.32) deposition efficiencies $\eta(\ell)$ of sodium chloride particles from hot air to cold pipe walls at 293 K, as a function of air in flow temperatureT_o

varying the air in flow temperature between 300^oC and 420^oC. The deposition efficiency over the test section of length $\ell = 0.965$ m was determined from measurements of the suspended-particle concentrations at in flow to and out flow from the test section. If it is assumed that the surface of the layer of deposited particles T_s is approximately equal to the temperature of the cooling water, comparisons can be made between Eq. 3.32 and the experimental measurements of deposition efficiency. The deposition efficiency η (Eq. 3.32) was calculated for x= 0.965 m, as a function of T_o, and plotted in Fig. 3.12 for 0.1 μm and 0.482 μm NaCl particles, together with the experimental measurements of Romay et al. From this figure, it is clear that the agreement between theory and experiment is good for both sizes of particle considered, and that the sensitivity of the theoretical prediction to particle size is comparable to that of the experimental data. It is also instructive to use Eq. 3.31 to

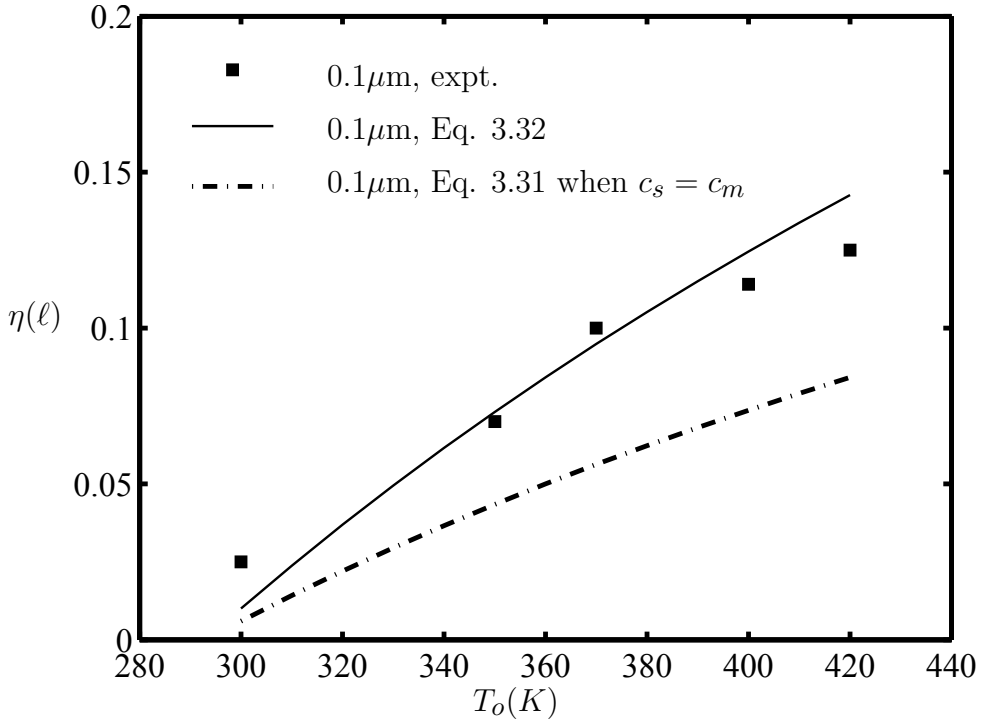

Figure 3.13: Effect of c_s/c_m on the deposition-efficiency predictions of Eqs. 3.31 and 3.32 as a function of air inflow temperature T_o.

explore the significance of the particle concentration profile and of T_s on particle-deposition efficiencies. In Fig. 3.13, the predicted deposition efficiency of Fig. 3.12 is plotted for 0.1 μm NaCl particles, together with the corresponding prediction when c_s/c_m is set to unity in Eq. 3.31 (the uniform concentration assumption). It is clear from this figure that the effect of this assumption is to underestimate the deposition efficiency by approximately 40%.

In the preceding discussion, an attempt was made to compare the development of deposition efficiency η along the tube with results published by other researchers. In the literature, there does not appear to be any experimental data on the spatial development of deposition efficiency along the pipe (Eq. 3.32). However, it is interesting to compare our prediction of $\eta(x)$ with the empirical function proposed by Stratmann et al. [123] as an accurate fit to a large set of computational results. This empirical fit is to numerical solutions to the laminar continuity, Navier-Stokes, thermal energy, and species thermophoretic diffusion equations,

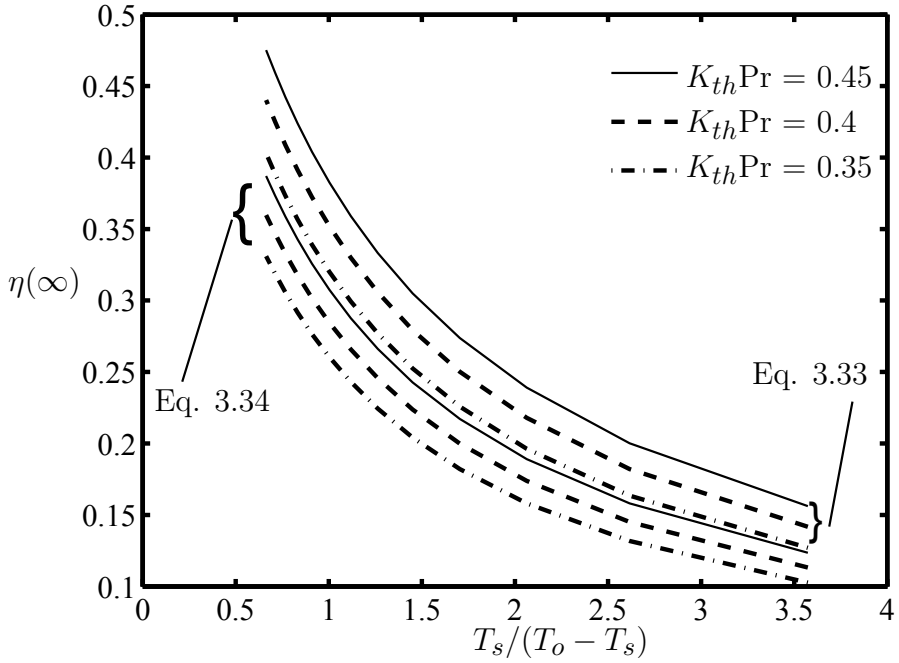

Figure 3.14: Predictions of total deposition efficiency from Eqs. 3.33 and 3.34 as a function of reciprocal temperature difference, for $K_{th}\mathrm{Pr} = 0.35$; 0.40; 0.45.

with temperature-dependent properties and surface boundary conditions of constant temperature and zero concentration, for developing flow along a pipe and takes the form:

$$\eta(\infty) = 1 - \exp\left\{-0.845\left[\frac{K_{th}\mathrm{Pr} + 0.025}{T_s/(T_o - T_s) + 0.28}\right]^{0.932}\right\} \tag{3.34}$$

with x-dependence accounted for by a separate function $\eta(x)/\eta(\infty)$ which was presented graphically in [123]. It is interesting to note that, if the fitted coefficient 0.932 were set to unity, the functional form of this equation would essentially be that which is obtained by integrating Eq. 3.31 when setting c_s/c_m to a constant rather than a function of x. It therefore appears that the four coefficients in Eq. 3.34 account for: *i*) the implicit dependence of c_s/c_m on $T_s/(T_o - T_s)$; *ii*) the effect on η of employing the $c_s = 0$ boundary condition; and *iii*) the effect of temperature-dependent properties on η.

The deposition efficiency $\eta(\infty)$ has been evaluated based on the two mentioned expressions: Eq. 3.34 which is an empirical fit to Stratmann's numerical results and Eq. 3.33 that originates from the series solution presented in this paper; for three various reciprocal temperature differences. These results are shown in Fig. 3.14. While the trends followed by each prediction of $\eta(\infty)$ for different values of K_{th} Pr are very similar, the absolute values of deposition efficiencies predicted according to this study are roughly 30% higher than those of the fit of Stratmann et al. This systematic discrepancy is a consequence of the inclusion of molecular diffusion in the computations of Stratmann and the different treatments of the concentration boundary condition at the pipe surface. As explained in Sec. 3.2.2, our solution for c/c_s requires one integration and the imposition of a single symmetry boundary condition at $r^+ = 0$, yet it yields the results that $c_s \neq 0$ and $\partial c/\partial r|_{r^+=1} \simeq 0$, which are consistent with the deductions of Sec. 3.2.2. If we recall that the thermophoretic flux is equal to $K_{th}\nu c\partial(lnT)/\partial r$, the $c_s = 0$ boundary condition will set this flux to zero at the surface and so the particulate flux will occur only through molecular diffusion. On the other hand, the results that $\partial c/\partial r|_{r^+=1} \simeq 0$ and that c_s is finite at the surface require that there is thermophoretic flux at the surface but that molecular diffusional flux is negligible. The greater size of the surface thermophoretic flux, relative to molecular diffusional flux, in these flows accounts for the greater deposition velocities and efficiencies predicted by the results of this study.

The x-dependence of η is plotted as $\eta(x)/\eta(\infty)$ against $x/(\mathrm{Pe}R)$ in Fig. 3.15 for the model developed in this paper and the x-dependence deduced from the computations of Stratmann et al. The effect on $\eta(x)/\eta(\infty)$ of varying $K_{th}\mathrm{Pr}$ and $T_s/(T_o - T_s)$ between the largest and smallest values they take in the data of Fig. 3.14 is small and of the order of a few thickness of the lines plotted in Fig. 3.15. While the x-dependence of the two

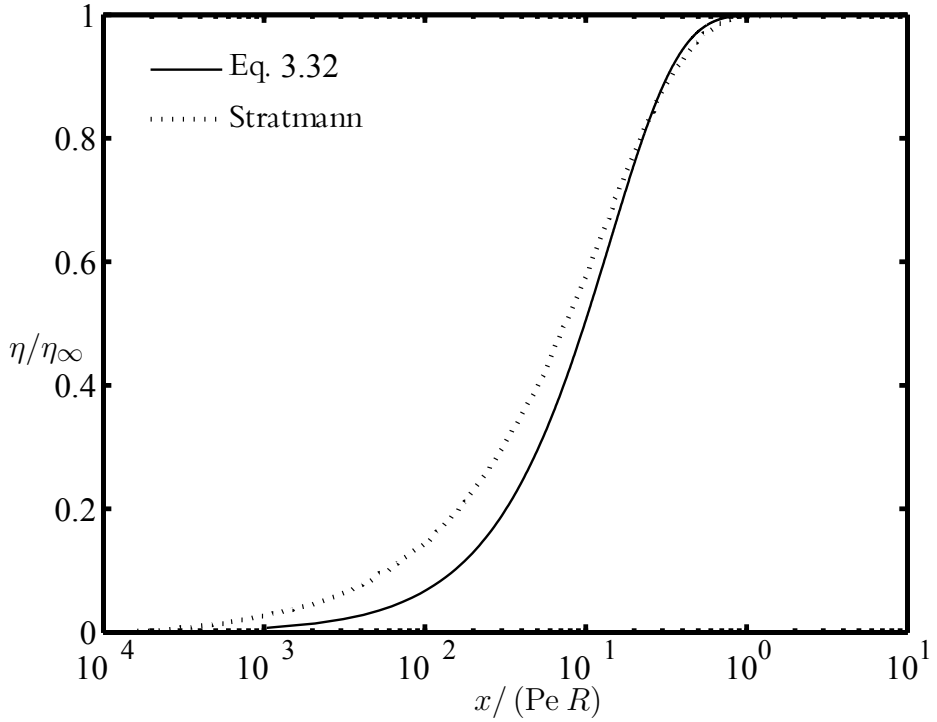

Figure 3.15: Predictions of x-dependence of deposition efficiency from Eqs. 3.32 and 3.34 when plotted as functions of $x/(\mathrm{Pe}R)$.

deposition-efficiency predictions is in good agreement for $x/(\mathrm{Pe}R) > 0.2$, the discrepancies between the two models grow at x-locations closer to the pipe inflow. These discrepancies for $x/(\mathrm{Pe}R) < 0.2$ are unsurprising as the deposition model of this study was developed using a fully-developed temperature profile and so would not be expected to yield accurate results within this region of thermal development. The results presented by Stratmann et al. include entrance zone effects and as the temperature gradients are higher in this zone, the corresponding deposition efficiencies presented by Stratmann et al. have higher values in the entrance zone than our thermally developed solution.

From this analytical solution and comparisons with experimental studies, it appears that the assumption of a fully-developed concentration field, analogous with that of a fully-developed temperature field, leads to good agreement with the limited experimental data

available on deposition efficiency. The second proposed parameter for describing a fully-developed concentration field—the ratio of absolute particle concentrations—is next used to solve the particle transport equation, and is discussed in the following section.

3.2.3 Fully-Developed Pipe Flow($\theta = c/c_m$)

In this section, an analytical solution for the flow in a pipe analogous to that Sec. 3.2.2 is presented, only using a different criterion for fully-development of the particle concentration profile.

As presented in the previous section, the velocity profile in steady, laminar, constant-property, fully-developed flow along a pipe is

$$u = 2U_m\left(1 - r^{+2}\right) \quad \text{and} \quad \frac{T - T_s}{T_m - T_s} = 1.803 - 3.296r^{+2} + 2.331r^{+4} - 1.143r^{+6} + \cdots = f(r^+) \tag{3.35}$$

following Shokouhmand and Hooman [116].

An overall energy balance in the x-direction, from the pipe entrance at $x = 0$ where the fluid temperature is T_o to downstream location x, under the assumption of a constant heat-transfer coefficient (*i.e.* neglecting thermal entrance effects) yields

$$\frac{T_m(x) - T_s}{T_o - T_s} = e^{-2\,\mathrm{Nu}\,x/(\mathrm{Pe}\,R)} \tag{3.36}$$

and an overall particle mass balance over a section of length dx through the outer region requires that

$$\frac{dc_m}{dx} = -\mathrm{Nu}\,\frac{K_{th}\nu}{U_m R^2}\frac{c_s}{T_s}\left(T_m - T_s\right) \tag{3.37}$$

The corresponding particle transport equation will be similar to 3.15.

The x-dependence of the $e^{-\beta x}$ term in Eq. 3.15 precludes an exact analytical solution for a fully developed concentration profile. However, a series approximation to such a solution can be made if the dimensionless concentration profile in the outer region is expressed as $\theta(r^+) = c(r^+, x)/c_m(x)$, with the condition on full profile development that $\partial\theta/\partial x = 0$. The concentration ratio θ is one of absolute values of particle concentration, because the thermophoretic flux depends on the absolute concentration. It follows that the condition for a fully-developed concentration profile is

$$\frac{\partial c}{\partial x} = \frac{c}{c_m}\frac{dc_m}{dx} \tag{3.38}$$

Substitution of this constraint into Eq. 3.15 renders it an integro-differential equation on account of the definition of c_m. It is important to note that the left-hand side of Eq. 3.15 is zero at $r^+ = 1$ irrespective of the full-development assumption. It follows that Eq. 3.38 is applied only when $r^+ < 1$ and not at $r^+ = 1$, where the mathematical result of Weinberg [140] that c_δ is constant when $K_{th}\mathrm{Pr} = 1$ would otherwise implausibly require $dc_m/dx = 0$.

A series solution for the concentration profile may be found by substituting the series $c/c_\delta = c_0 + c_1 r^+ + \cdots$ and Eq. 3.38 into Eq. 3.15 and integrating, subject to the boundary condition that c is symmetric about $r^+ = 0$. The power-series coefficients may be found by equating the left- and right-hand sides of the resulting equation at each power of r^+. Equating terms at ${r^+}^2$ yields the result

$$\frac{c_\delta}{c_m} = \frac{1.803}{1 + 1.803e^{-\beta x}\left[T_o/T_s - 1\right]} \tag{3.39}$$

while equating at even powers of y^+ yields a system of algebraic equations from which

successive values of the series coefficients may be determined, of the form:

$$c_2 = 1.8284 c_0 \left(1 - \frac{3.606 e^{-\beta x} \left[T_o/T_s - 1 \right]}{1 + 1.803 e^{-\beta x} \left[T_o/T_s - 1 \right]} \right) \; ; c_4 = 1.6213 c_2 \left(\cdots \right) - 1.5656 c_0 \left(\cdots \right) \; etc. \tag{3.40}$$

These relationships may be combined with the definition of c_m and the requirement that $c = c_\delta$ at $r^+ = 1$ to yield the complete series solution for c/c_δ to arbitrary order. In the limit of large x, the outer concentration profile takes the form

$$\begin{aligned} \frac{c}{c_\delta} &= 0.3080 + 0.5632 r^{+2} + 0.4324 r^{+4} + 0.0878 r^{+6} - 0.1560 r^{+8} - 0.1915 r^{+10} \\ &\quad -0.1049 r^{+12} - 0.0129 r^{+14} + 0.0738 r^{+16} + \cdots \end{aligned} \tag{3.41}$$

in which case $c_\delta/c_m = 1.803$, $c_\delta/c(0) = 3.247$, $\mathrm{Sh}_{th} = 6.59$ and $\partial c/\partial r \simeq 0$ at $r^+ = 1$. The shape of the profile is independent of the thermophoretic and viscosity coefficients and is therefore invariant with the size and kind of submicron particle in this outer solution.

3.2.3.1 Development of the Sherwood Number and the Concentration Field

It can be shown from the Graetz solution for heat transfer at the pipe entrance that the Nusselt number for fully developed flow in a pipe of uniform wall temperature reaches its asymptotic value of 3.657 at approximately $x/\left(\mathrm{Pe}\, R\right) = 0.1$ [60]. Beyond this x-location, the thermophoretic Sherwood number in Eq. 2.16 can be expressed using Eq. 3.39 as:

$$\mathrm{Sh}_{th} = \frac{6.593}{1 + 1.803\, e^{-\beta x} \left[T_o/T_s - 1 \right]} \tag{3.42}$$

This Sherwood number is plotted against $x/\left(\mathrm{Pe}\, R\right)$ in Fig. 3.16, when the ratio of inflow temperature to wall temperature T_o/T_s (in Kelvin) takes the values: 1.25; 1.5; 1.75 and 2.0.

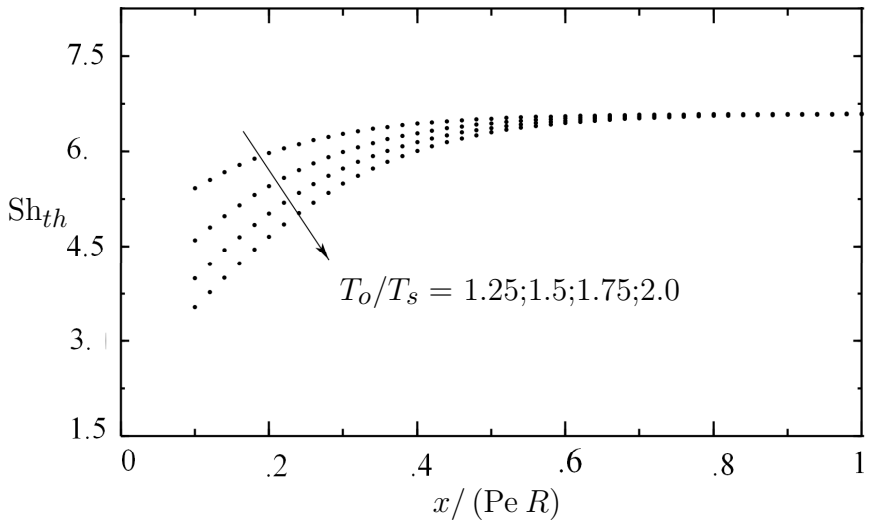

Figure 3.16: Thermophoretic Sherwood number Sh_{th} plotted against $x/\,(\mathrm{Pe}\,R)$ when $T_o/T_s = 1.25$; 1.5; 1.75 and 2.0.

From this figure, it is clear that Sh_{th} at each temperature ratio tends towards an asymptotic value of approximately 6.6, which is reached after a development length of roughly $0.6\,\mathrm{Pe}\,R$, when c_δ/c_m attains a fully-developed value of about 1.8. Since this concentration entrance length is about six times longer than the thermal development length, the assumption in the preceding analysis of a fully-developed temperature field for the entire flow appears to be reasonable.

Within the concentration-ratio development region of $x/\,(\mathrm{Pe}\,R) < 0.6$, there is a significant effect of the ratio T_o/T_s on the Sherwood number, with higher temperature ratios corresponding to lower mass-transfer conductances at any given axial position. However, the particle flux J_r is proportional to the product of Sh_{th} and $T_m - T_s$ and if this temperature difference is replaced by $(T_o - T_s)e^{-2\,\mathrm{Nu}\,x/(\mathrm{Pe}\,R)}$ from Eq. 3.36, the particle flux is still seen to decay almost exponentially with distance along the pipe regardless of the value of T_o/T_s, as shown in Fig. 3.17.

The particle concentration ratio c/c_δ within the concentration development region is

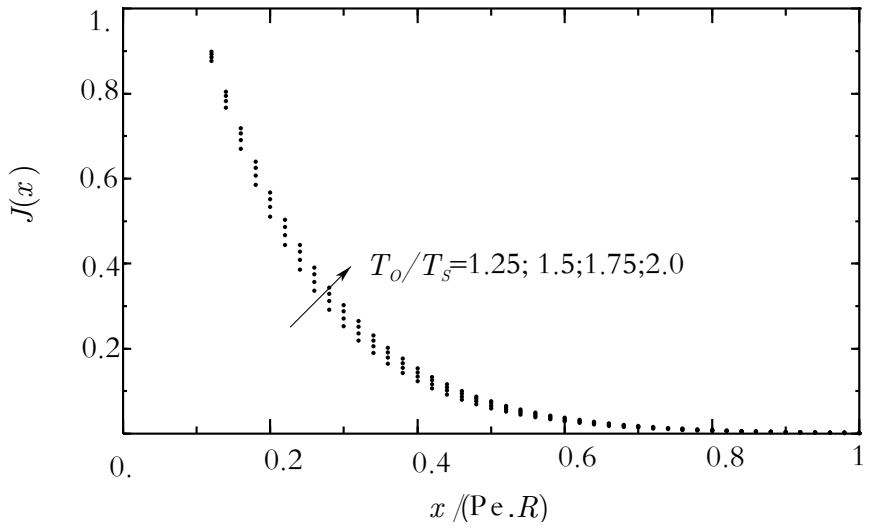

Figure 3.17: Normalized particle flux J plotted against $x/(\mathrm{Pe}\,R)$ when $T_o/T_s = 1.25$; 1.5; 1.75 and 2.0. The flux at each value of T_o/T_s is normalized by its value at $x/(\mathrm{Pe}\,R) = 0.1$.

plotted against r/R in Fig. 3.18 at several axial locations, at a representative temperature ratio of $T_o/T_s = 1.5$. From this figure, it can be seen that each c/c_δ profile takes an 'S' shape, with the lowest particle concentrations at the pipe center and the highest concentrations at the edge of the surface diffusion sublayer. The effect of axial development is to stretch the profile and reduce the concentration at the pipe center, with the asymptotic shape of the profile at large x matching the one plotted at $x/(\mathrm{Pe}\,R) = 0.8$. Thus Sh_{th}—the particle-deposition effectiveness, a dimensionless measure of $J\,T_s/(c_m\Delta T)$—increases with x during development because J does not decrease as rapidly as the product of c_m and ΔT. At complete development, when $x/(\mathrm{Pe}\,R) > 0.6$, Sh_{th} reaches its asymptotic value of 6.59 and J thereafter decreases with x at the same rate as $c_m\,\Delta T$.

It can also be seen from Fig. 3.18 that as $x/(\mathrm{Pe}\,R)$ increases, the radial gradient of the concentration profile at $r = R$—the edge of the diffusion sublayer—tends to zero. This result appears to be a consequence of complete development of the outer concentration profile. It also provides an outer boundary condition for calculation of the inner diffusive sublayer

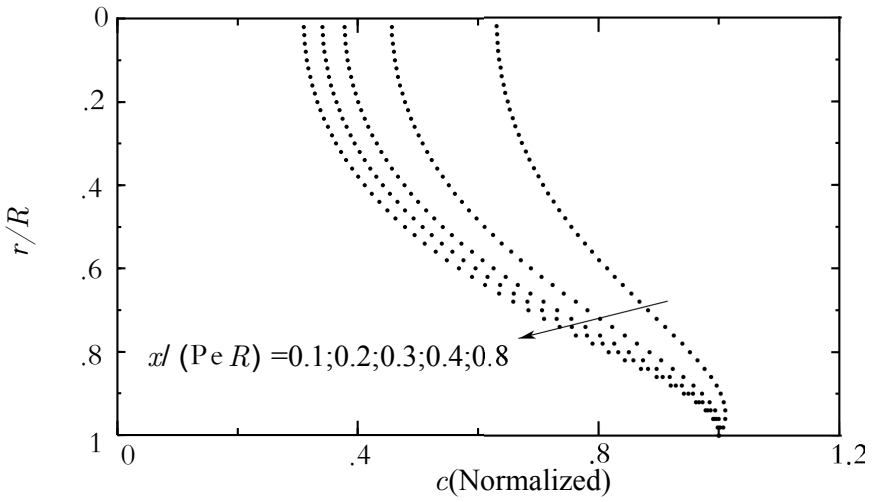

Figure 3.18: Radial profiles of normalized $c(c/c_\delta)$ plotted at $x/\,(\mathrm{Pe}\,R) = 0.1$; 0.2; 0.3; 0.4 and 0.8, when $T_o/T_s = 1.5$.

that is independent of x and so is compatible with a fully-developed sublayer concentration profile. At present, there do not appear to be any experimental measurements of particle-concentration profiles for comparison with these theoretical results.

3.2.3.2 Particle Deposition Efficiency and Concentration Profile Development

The efficiency of particle deposition at some axial position x is defined as the mass flow rate of particles deposited on the wall of the pipe, from the pipe entrance that location, divided by the mass flow rate of particles entering the pipe, and is expressed as

$$\eta(x) = 1 - \frac{c_m(x)}{c_{m_0}} \tag{3.43}$$

where $c_{m_0} = c_0$ and is the mixed-mean particulate concentration at the pipe entrance. It is found most readily from Lagrangian particle-trajectory calculations such as those of Walker

et al. [136], whose numerical results appear to be in good agreement with the formula

$$\eta(x) = \mathrm{Pr} K_{th} \phi_0 \left[T_o/T_s - 1\right] \left(1 - e^{-2\,\mathrm{Nu}\,x/(\mathrm{Pe}\,R)}\right) \tag{3.44}$$

in which ϕ_0 is the value of c_δ/c_0 obtained from a similarity solution for thermophoretic transport in the concentration entrance zone. They also agree with the experimental deposition-efficiency measurements of Romay et al.[107]. If we note that

$$\frac{d\eta}{dx} = -\frac{1}{c_0}\frac{dc_m}{dx} \tag{3.45}$$

we can equate values of dc_m/dx in the derivative of the approximate deposition-efficiency formula of Walker et al.[136] and in the overall particle mass balance (Eq. 3.37) to yield the result that $c_\delta(x)/c_0 \simeq \phi_0$, from which it follows that $c_\delta(x)$ is approximately constant.

It is important to note that Eq. 3.44 can be obtained as a mathematical solution to the particle transport equations for this flow only for the case of $K_{th}\mathrm{Pr} = 1$, when c_δ can be shown to be constant. At other values of $K_{th}\mathrm{Pr}$, c_δ is not necessarily a constant. The observation that Eq. 3.44 is in good agreement with numerical solutions for $\eta(x)$ for a range of values of $K_{th}\mathrm{Pr}$ merely implies that, for the purposes of matching deposition-efficiency data, c_δ can usefully be *approximated* as if it were a constant, even when $K_{th}\mathrm{Pr} \neq 1$. Thus if c_δ is approximated in this manner, the profiles of c/c_δ in Fig. 3.18 are approximately profiles of c each of which is normalized by the same value, and therefore describe the progressive reduction of c in the outer flow with increasing $x/\left(\mathrm{Pe}\,R\right)$. In the limiting case of very large x, when the gas temperature equilibrates with the wall temperature and c becomes small, thermophoresis no longer dominates diffusion in the outer flow and these results for profile

shape and for the x-dependence of c_δ would not apply.

From the results of thi ssection and the previous one, it appears seen that both proposed criteria for the full development of the particle concentration field lead to results with similar trends, which are both in reasonable agreement with what limited data are available on particle deposition efficiency. The approach based on a ratio of absolute concentration $\theta = \frac{c}{c_m}$, consistent with the thermophoretic flux dependence on absolute concentration, resulted in a mass-transfer effectiveness of Sh_{th}=5.0. The approach analogous with the dimensionless temperature of diffusive thermal, $\theta = \frac{(c-c_s)}{(c_m-c_s)}$, resulted in Sh_{th}=6.6. The simplified transport equation (Eq. 3.15) was also solved by a finite difference code and yielded the result Sh_{th}=6.4. However, since the appropriateness of wall boundary conditions for this computations (which are discussed in a later chapter) is not not clear, it is difficult to say which of the criteria for full development is more rational. These matters are discussed further in the following section, when the deposition efficiencies and particle transport in a channel flow and a plate-to-plate precipitator are considered.

3.2.4 Fully-Developed Channel Flow

The problem of thermophoretic transport of particles in a gas flowing between two parallel plates at the same uniform temperatures can be solved in the outer region in a similar manner, when the velocity and temperature profiles can be approximated as their constant-property fully-developed forms. This thermophoretic transport problem is similar to the pipe flow when r and R are replaced by y and the channel half-width h.

The Nusselt number $\hbar 4h/k$ for this flow is 7.54 [60]. The velocity and temperature profiles in fully developed flow can be expressed in terms of the average velocity U_m, the mixed-mean

temperature $T_m(x)$, and $y^+ = y/h$, as

$$u = \frac{3}{2} U_m \left(1 - {y^+}^2\right) \quad \text{and} \quad \frac{T - T_s}{T_m - T_s} = 1.319 - 1.865 {y^+}^2 + 0.750 {y^+}^4 - 0.246 {y^+}^6 + \cdots = f(y^+) \tag{3.46}$$

when the series form of the temperature profile is found using the approach of Shokouhmand and Hooman [116].

An overall energy balance from the channel entrance ($T = T_o$ at $x = 0$) to x, under the assumption of a constant heat-transfer coefficient yields

$$\frac{T_m(x) - T_s}{T_o - T_s} = e^{-\mathrm{Nu}\, x/(2\mathrm{Pe}\, h)} \tag{3.47}$$

and an overall particle mass balance over a section of length dx through the outer region requires that

$$\frac{dc_m}{dx} = -\mathrm{Nu}\, \frac{K_{th}\nu}{4U_m h^2} \frac{c_\delta}{T_s} \left(T_m - T_s\right) \tag{3.48}$$

After substitution of Eqs. 3.46, 3.47 and 3.48, the outer particle transport equation is written as

$$-\frac{3}{8}\, \mathrm{Nu}\, c_\delta \left(1 - {y^+}^2\right) \frac{\partial c}{\partial x} = \frac{dc_m}{dx}\, \frac{\partial}{\partial y^+} \left(\frac{c\, f'(y^+)}{1 + f(y^+) e^{-\beta x} \left[T_o/T_s - 1\right]} \right) \tag{3.49}$$

where f' is the derivative of f in Eq. 3.46 and $\beta = \mathrm{Nu}/\left(2\, \mathrm{Pe}\, h\right)$.

When the dimensionless concentration profile in the outer region is expressed as $\theta(y^+) = c(y^+,\, x)/c_m(x)$, with the fully-developed condition that $\partial\theta/\partial x = 0$ substituted into Eq. 3.49, a series solution to the resulting integro-differential equation may be found by substituting the series $c/c_\delta = c_0 + c_2 {y^+}^2 + \cdots$ into Eq. 3.49, integrating subject to the boundary condition that c is symmetric about $y^+ = 0$, and equating the left- and right-hand sides of the resulting

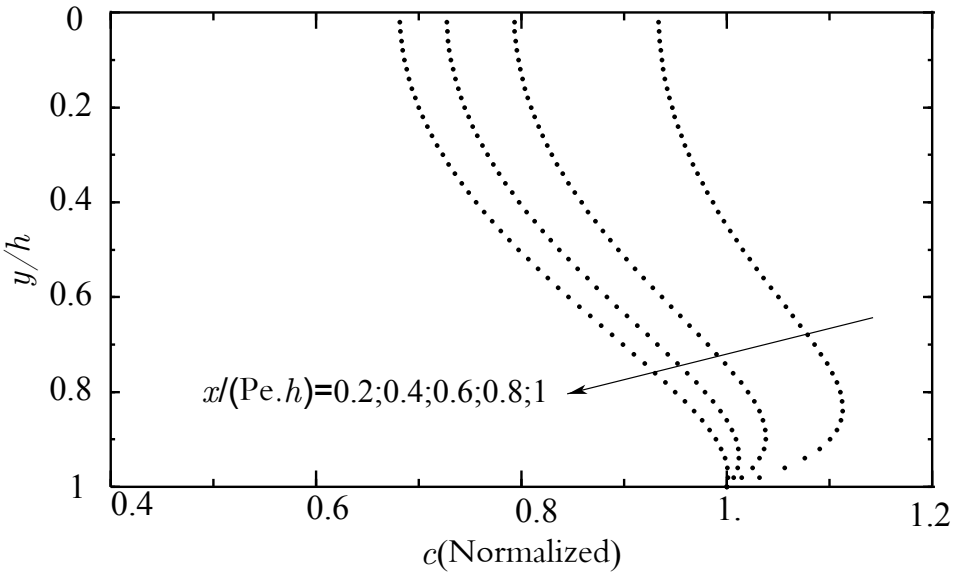

Figure 3.19: Profiles of normalized c (c/c_δ) plotted at $x/(\mathrm{Pe}\, h) = 0.2$; 0.4; 0.6; and 1.0, when $T_1/T_0 = 1.5$.

equation at each power of y^+.

Equating terms of order y^+ yields the result

$$\frac{c_\delta}{c_m} = \frac{1.319}{1 + 1.319e^{-\beta x}\,[T_o/T_s - 1]} \quad \text{or} \quad \mathrm{Sh}_{th} = \frac{9.945}{1 + 1.319e^{-\beta x}\,[T_o/T_s - 1]} \tag{3.50}$$

while equating at odd powers of y^+ enables successive values of the series coefficients to be determined to arbitrary order. In the limit of large x, the outer concentration profile takes the form

$$\frac{c}{c_\delta} = 0.6685 + 0.4722y^{+2} + 0.0257y^{+4} - 0.1144y^{+6} - 0.0623y^{+8} + 0.0103y^{+10} + \cdots \tag{3.51}$$

in which case $c_\delta/c_m = 1.319$, $c_\delta/c(0) = 1.496$, $\mathrm{Sh}_{th} = 9.945$ and $\partial c/\partial r \simeq 0$ at $y^+ = 1$.

The particle concentration ratio c/c_δ within the concentration development region is plotted against y/h in Fig. 3.19 at several axial locations, at a representative temperature

ratio of $T_o/T_s = 1.5$. It can be seen that each c/c_δ profile also takes an 'S' shape, with the lowest particle concentrations at the channel center. However, the effect of axial development is to collapse the near-surface peak in concentration towards the wall while reducing the concentration at the channel center. The asymptotic shape of the profile at large x matches that at $x/(\mathrm{Pe}\, h) = 1.0$, when development is complete. As was the case for pipe flow, the particle-deposition effectiveness Sh_{th} increases with x during development because the flux J does not decrease as rapidly as the product of c_m and ΔT, whereas, after complete development, Sh_{th} reaches its asymptotic value of 9.95 and J thereafter decreases with x at the same rate as $c_m\, \Delta T$. There do not appear to be any experimental measurements with which these concentration-profile results can be compared.

3.2.4.1 Particle Deposition Efficiency and Concentration Profile Development

The x-derivative of the particle-deposition efficiency is

$$\frac{d\eta}{dx} = -\frac{1}{c_0}\frac{dc_m}{dx} \tag{3.52}$$

into which dc_m/dx can be substituted from the overall particle mass balance (Eq. 3.48) to yield the result

$$\frac{d\eta}{dx} = \frac{c_\delta}{c_0}\mathrm{Pr}K_{th}\left[\frac{T_o}{T_s} - 1\right]\frac{\mathrm{Nu}}{2\mathrm{Pe}h}\, e^{-\mathrm{Nu}\, x/(2\mathrm{Pe}\, h)} \tag{3.53}$$

If $c_\delta(x)/c_0$ is assumed to take a constant value, Eq. 3.53 can be integrated, subject to the initial condition that $\eta(0) = 0$, to yield the channel-flow deposition efficiency

$$\eta = \frac{c_\delta}{c_0}\mathrm{Pr}K_{th}\left[\frac{T_o}{T_s} - 1\right]\left(1 - e^{-\mathrm{Nu}\, x/(2\mathrm{Pe}\, h)}\right) \tag{3.54}$$

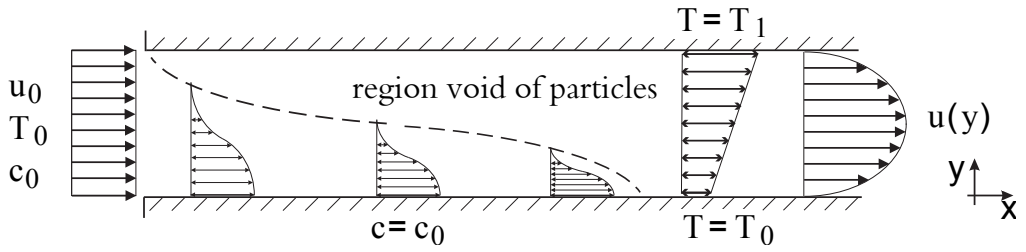

Figure 3.20: Thermophoretic particle transport in a plate-to-plate precipitator.

Although the analysis of Weinberg [140] can be extended readily to constant wall-temperature channel flow to show that c_δ is constant when $K_{th}\mathrm{Pr} = 1$, there do not appear to be any particle-trajectory calculations for this flow that would support or refute these conjectured deposition efficiency or $c_\delta(x)$ results. However, if these deposition-efficiency results are accurate approximations at values of $K_{th}\mathrm{Pr}$ other than one, as was the case for their pipe-flow counterparts, then the profiles of c/c_δ in Fig. 3.19 are profiles of c each of which is normalized by approximately the same value, and therefore approximate the reduction of c in the outer flow with increasing $x/\left(\mathrm{Pe}\, h\right)$.

3.2.5 Plate-to-Plate Thermophoretic Precipitator Flow

Thermophoretic deposition in a plate-to plate precipitator with the geometry of a channel of width H, a hot wall at T_1, and a cold wall at T_0 (Fig. 3.20), has been studied by Tsai and Lu [132]. Within this fully-developed velocity/temperature field, the linear temperature profile allows particle trajectory calculations to be carried out analytically to yield the exact deposition-efficiency result

$$\eta = \frac{K_{th}}{\mathrm{Re}}\left[\frac{T_1}{T_0} - 1\right]\frac{x}{H} \tag{3.55}$$

where Re is the Reynolds number referenced to mean velocity and channel width H. This expression for deposition efficiency is in excellent agreement with the experimental measure-

ments of Messerer *et al.* (2003). Deposition is complete when $x/H = (\mathrm{Re}/K_{th})/\left[T_1/T_0 - 1\right]$. This flow is more difficult to analyze in an Eulerian frame because a region void of particles develops along the hot wall and grows to fill the precipitator. This region is delineated from the particle-laden flow by the trajectory line of particles which enter the channel adjacent to the hot wall, as sketched in Fig. 3.20. However, by combining Lagrangian and Eulerian analyses, one can determine Sh_{th} and gain a better understanding of this flow.

3.2.5.1 Particle Deposition Efficiency and Concentration Profile Development

By combining the result that

$$\frac{d\eta}{dx} = -\frac{1}{c_0}\frac{dc_m}{dx} \tag{3.56}$$

with the deposition efficiency of Eq. 3.55 and the overall particle mass balance for this flow (with particle deposition only at the cold surface):

$$\frac{dc_m}{dx} = -\frac{K_{th}}{\mathrm{Re}\, H}\left[\frac{T_1}{T_0} - 1\right] c_\delta \tag{3.57}$$

it can be shown that $c_\delta(x) = c_0$ in this flow, and that c_m therefore decreases linearly with x and that the particle deposition rate is uniform, regardless of the value of $K_{th}\mathrm{Pr}$. It follows that the thermophoretic Sherwood number is

$$\mathrm{Sh}_{th} = \frac{1}{1 - (K_{th}/\mathrm{Re})\left[T_1/T_0 - 1\right](x/H)} \tag{3.58}$$

for which concentration profiles and the trajectory of particles introduced to the flow at the hot wall are sketched in Fig. 3.20. The thermophoretic Sherwood number for this flow takes a value of unity at the precipitator's entrance and becomes infinitely large at the point at

which deposition is theoretically completed. This progressive increase in particle-deposition effectiveness with downstream distance reflects the effect of thermophoresis in concentrating the particulate field closer to the cold wall with increasing x. Thus, in a flow with a uniform temperature difference, and a bulk particle concentration c_m that *decreases* with x, the effectiveness of particle deposition Sh_{th} must *increase* with x to maintain a uniform particle deposition flux.

3.2.6 Concluding Remarks

In this section, we have presented new analytical solutions in the form of series for the concentration profile c/c_δ in laminar, submicron-particle laden, one-way coupled, fully-developed pipe and channel flows, in which particulate flux is driven by thermophoresis from a hot fluid to a cold wall at a constant surface temperature. These solutions extend through the outer, thermophoretically-dominated region of the flow to the edge of the thin surface sublayer within which effects of Brownian diffusion become important. They can be used to provide boundary conditions for analyses of the concentration field within this sublayer, as well as for inflow and boundary conditions for computational studies of thermophoretically driven flows, in which a boundary condition at the edge of the surface sublayer is often required because the computational cost of resolving the diffusional sublayer can be excessive. The solutions can also be used to determine particle concentrations at the edge of the surface sublayer from measurements made at the center of a pipe or channel, and hence provide an indirect technique for deducing particulate deposition fluxes in these flows. The solution procedure presented in this paper can also be applied to other fully-developed problems such as channel flows with two cold walls *etc.*, though achieving smooth solutions from summations of terms to arbitrary order may require methods for recovering accurate approximations to

exact solutions for slowly convergent or divergent series, such as Shanks transformations or Pade approximant summations.

In the developing flat-plate boundary layer (details of which are provided as supplemental information), the free-stream concentration exceeds c_δ whereas, in the fully-developed pipe and channel flows, c_δ exceeds its bulk and centerline values. In fully developed flows, with no surface-normal bulk velocity, these concentration-profile shapes are a consequence of the thermophoretic effect of promoting the highest particle concentrations at the edge of the surface diffusive sublayer whereas, in the developing boundary layer, the advective surface-normal velocity v overwhelms this effect and yields the lowest particle concentrations at the edge of this surface sublayer. Since the entrance regions of pipe and channel flows can be thought of as boundary layers that eventually merge at the center of the duct, this finding implies that the concentration profiles in such flows undergo an inversion during development, from low concentrations near the cold surface and high concentration in the bulk flow at entry, to low concentrations in the bulk and high ones near the cold surface at full development.

An engineering approach to thermophoretic mass transfer, analogous to that of convective heat transfer, has been presented that permits the effectiveness of thermophoretic mass transfer to be compared from one flow to another, by factoring out the flow-specific effects on conductance of surface temperature and particle concentration. In this approach, the deposition mass flux $\dot{m}''$ is described by the model equation

$$\dot{m}'' = \frac{\hbar c_m}{T_s} \left(T_m - T_s \right) \tag{3.59}$$

in which the conductance $\hbar$ is expressed in the dimensionless form of the thermophoretic

Sherwood number

$$\mathrm{Sh}_{th} = \frac{\hbar D}{K_{th}\nu} \qquad \text{where} \qquad \mathrm{Sh}_{th} = \mathrm{Nu}\frac{c_\delta}{c_m} \tag{3.60}$$

This thermophoretic Sherwood number provides physically meaningful characterizations of the deposition effectiveness in laminar pipe, channel, plate-to-plate precipitator, and flat-plate boundary-layer flows. It is used to illustrate how in duct flows the effectiveness of particle deposition increases with downstream difference, reaching an asymptotic value of $\mathrm{Sh}_{th} = 6.59$ in pipes and $\mathrm{Sh}_{th} = 9.95$ in channels, when the particle concentration profile reaches full development for $x/\left(\mathrm{Pe}\, R\right) > 0.6$.

A knowledge of the thermophoretic Sherwood number can also be used to calculate the particle deposition flux from bulk-flow information and comparisons of Sh_{th} and $\hbar$ can be made for different flow geometries to determine which is the more (or less) effective in depositing particles from hot gases to cold surfaces. For example, if a comparison is made fully-developed constant-wall-temperature pipe ($\mathrm{Sh}_{th} = 6.6$) and channel ($\mathrm{Sh}_{th} \simeq 9.95$) flows on the basis of equal hydraulic diameters, it can easily be shown that $\hbar$ is 1.51 times larger for the channel flow and so the channel is more effective in promoting thermophoretic mass transfer under this constraint. From the definition of the thermophoretic Sherwood number, it is also clear that in steady laminar flows convective heat transfer effectiveness and thermophoretic mass transfer effectiveness are very closely coupled, and that increasing/decreasing one necessarily increases/decreases the other.

Chapter 4

The Surface Boundary Condition for the Particle Transport Equation

The transport equation (Equation 2.11) for particulate flows affected by both molecular diffusion and thermophoresis is an advection-diffusion equation with an additional source term, so two boundary conditions are required for the solution, such as the particulate concentration or its normal derivative at the center of the duct and at the surface. A no-flux condition is applied at the center of the duct to enforce symmetry. However, the exact form of the near surface boundary condition is less clear. Several approaches for predicting the transport of fine particles adjacent to the surface have been presented which will be discussed in details. The particle transport equation has been solved using both compressible and incompressible numerical codes, and several different surface boundary conditions so that the effect of each boundary condition on the computed concentration profiles could assertained.

4.1 Concentration Profiles in Compressible Flows

The compressible solver used to compute the entrance-zone flow in a tube discussed in Section. 3.1 was used to calculate the velocity, temperature and concentration fields. When using this compressible solver, it was necessary to include a small amount of (molecular)

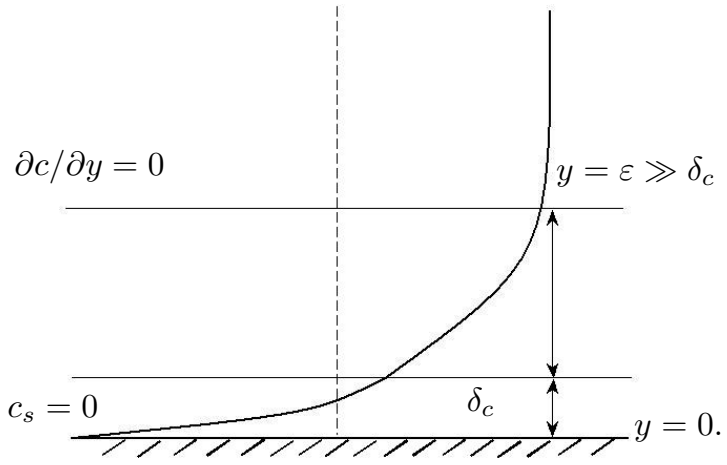

Figure 4.1: Concentration profile in proximity to the surface based on the Levéque method for temperature and concentration close to the inlet [136].

diffusion to stabilize the code in order to reach convergent solutions at reasonable computational cost. To avoid such numerical difficulties, it was assumed that Sc=120. Various boundary conditions were then imposed at the cold duct surface and their effects on the resultant concentration profiles are discussed in the following section.

4.1.1 Zero Particle Concentration at the Surface ($c_s = 0.$)

The condition of zero particle concentration at the surface has been used extensively in the literature [122, 123, 137, 44]. This condition originates from the assumption that all submicron particles that make contact with the surface attach to it immediately and so are no longer present in the gas phase. Walker et al. [136] proposed an analytical solution based on the Levéque approximation of the temperature and concentration fields close to the inlet which was restricted to a very thin surface diffusion layer, with zero particle concentration at the wall. Walker's analytical solution showed that the concentration at the outer edge of

the diffusion layer possessed a finite value which could be calculated numerically. At long longitudinal distances the requirements for the Levéque approximation did not apply so a Lagrangian approach was used to evaluate the deposition efficiencies. It was observed that the deposition efficiencies determined from the analytical solution were almost the same as those found from the results of numerical calculations near the inlet ($z/Pe < 10^{-3}$), although the discrepancy grew with increasing distance from the inlet. Walker's solution yielded large concentration gradients across the diffusion layer which has a thickness δ_c of order $Sc^{-1}Pe^{-1/3}$, shown in Fig. 4.1. A similar boundary condition was used in the more recent numerical simulations of Walsh et al. [137] and Gutti and Loyalka [44]. In the case of large Schmidt numbers (thermophoresis-dominated), very high concentration gradients are evident in this diffusion layer. At smaller Schmidt numbers–where thermophoresis and Brownian diffusion are of the same order of magnitude; concentration profiles based on the zero wall concentration vary smoothly. In the case of fine particles, the concentration boundary layer is extremely thin and a very fine mesh is required close to the surface to capture the high gradients, which results in a significant increase in the computational cost. The experimental measurements of Lee and Hanratty on droplet deposition [73] showed that the widely used boundary condition of $c_s = 0$ is only approximately correct in the case of very small droplets driven to the wall by Brownian diffusion. Some practical approximations to this boundary condition are discussed below.

4.1.2 Particle Flux Conservation at the Surface

A second possible boundary condition can be derived by considering the simplified form of the particle continuity equation as the surface is approached. The concentration profile is expected to change smoothly. As the surface is approached, the convective terms must

diminish as a result of the no-slip condition on velocity. At locations beyond the edge of the diffusive sublayer, where thermophoresis dominates molecular diffusion, the gradient of thermophoretic flux in longitudinal direction is small compared to the radial direction and, since variations in fluid density are small at low Mach numbers, the divergent of the thermophoretic fluxes should be approximately zero. Therefore Eq. 3.12 should simplify to $\partial(r.c.v_{th})/\partial r = 0$ where v_{th} is the thermophoretic velocity.

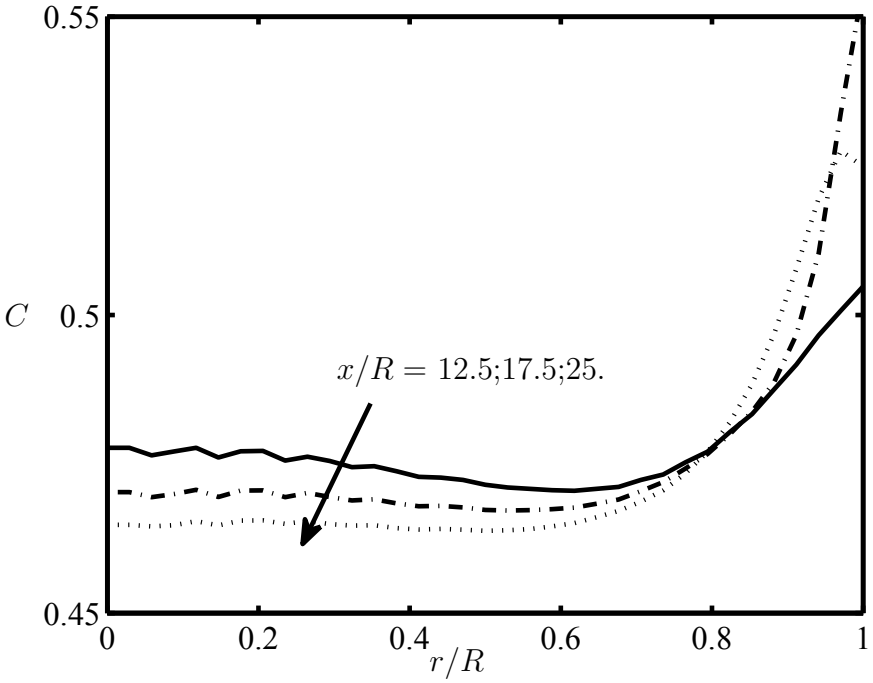

Figure 4.2: Development of concentration profiles along the tube at Re=300, Sc=120 based on the conservation of flux at approach to the cold surface

Young et al. made a comprehensive study of the deposition of particles in turbulent flows and suggested that a $c_s = 0$ boundary condition was not valid, even in diffusion dominated flows [144]. Guha [41] proposed that in the limiting case of very small particles, their concentration at the surface approaches zero and in the strictly inertial limit of very large particles, the appropriate surface boundary condition is $\partial c/\partial r = 0$. Interestingly enough, when he calculated the efficiency of deposition of particles (for which several sets of experimental

data are available) in simple flows, he found that changing from one boundary condition to another had a negligibly small effect on the efficiency. For submicron particles with thermophoresis as the dominant transport mechanism, the condition of zero concentration at the surface is difficult to apply, and other conditions applied at a short distance from the wall may be more suitable for both analysis and computation.

4.1.3 A Kinetic Theory Analogy at the Surface

A concentration boundary condition for submicron particle transport that considers both diffusion and thermophoresis is now considered. It is based on a proposed analogy between the behavior of submicron particles in a gaseous medium and the behavior of molecules in a gas, as described by kinetic theory, and is an extension to the model developed by Young et al. [144] (see Appendix A for details). It is assumed that the thermophoretic velocity of particles can be described by the standard constitutive equation, with Talbot's formula used to determine the thermophoretic coefficient. Following Young's approach, it is assumed that each particle's velocity is described by a Maxwellian distribution centred around the sum of the convective and thermophoretic velocities ($v_r + v_{th}$). This analogy between molecular and particle distributions cannot be justified rigorously and is a topic for further research.

In order to understand the behaviour of particles close to the surface, it is useful to consider heat and particle mass transfer based on both the kinetic-theory analogy and continuum theory approaches. Transport phenomena involving particles and the surrounding gas tend to depend strongly on the Knudsen number. For $Kn \ll 1$ molecular collisions are so frequent that the flow may be considered as a continuum medium while for $Kn \gg 1$—which is referred as free-molecular regime—the collisions between the surrounding gas molecules and the particles dominate molecule/molecule collisions. The continuum theory is used in the

continuum regime while the kinetic approach may be more applicable in the free-molecular regime. The intermediate range of Knudsen numbers (or Knudsen regime) is more complicated and has been subject of extensive studies in the past decades, which are mostly based on the solution of the Boltzmann equation [22] which is a non-linear integro-differential equation. Bhatanagar, Gross and Krook simplified the original Boltzmann equation by assuming that molecules possess a Maxwellian distribution after replenishing collisions, which is known as the BGK approximation and is widely used as a convenient substitute for the original Boltzmann equation [7, 16].

For submicron particles such as soot spherules which are around 30 nm in diameter in air, with a mean free path of air ranging from 70 nm-60 μm–depending on temperature and pressure, the corresponding Knudsen number is greater than one and lies in the free-molecular or transition regime. The corresponding thermophoretic surface-normal flux at the surface takes the form:

$$J_r = \left[c(\upsilon + \upsilon_{th}) - D\frac{\partial c}{\partial r}\right]_{r=R} = \left[\frac{c}{2}(\upsilon + \upsilon_{th})\left(1 + erf\{M_r\} + \frac{e^{-{M_r}^2}}{\sqrt{\pi}M_r}\right)\right]_{r=R} \tag{4.1}$$

where υ and υ_{th} are the convective and thermophoretically induced components of the radial velocity and $M_r = (\upsilon + \upsilon_{th})/\sqrt{2kT/m_p}$. In the limiting case in which the sum of the convective and thermophoretic fluxes greatly exceeds the molecular diffusive one, corresponding to $K_{th}Sc \gg 1$, at $r = R$

$$M_r \to \infty, \quad erf\{M_r\} \to 1 \quad \text{so} \quad e^{-{M_r}^2} \to 0 \tag{4.2}$$

and the surface boundary condition simplifies to $\partial c/\partial r|_{r=R} = 0$. It is interesting to note

that, in the other limiting case in which molecular or Brownian diffusion is dominant and $K_{th}Sc$ is not large, at $r = R$

$$M_r \to 0, erf\{M_r\} \to 0 \quad \text{so} \quad e^{-{M_r}^2} \to 1 \tag{4.3}$$

and the boundary condition would be simplified as

$$D\frac{\partial c}{\partial r}\bigg|_{r=R} = c\sqrt{\frac{kT/m_p}{2\pi}}\bigg|_{r=R} \tag{4.4}$$

which is similar to the expression used in the theory of gases to relate the diffusive flux and the rate at which particles are projected towards the surface. It is seen that even in the case of pure Brownian diffusion, the kinetic-theory model does not yield the $c = 0$ boundary condition, which has been widely used in previous continuum-level studies (see, for example, [41, 70]), consistent with the observations of Lee and Hanratty for droplet deposition [73]. It is noticeable that this boundary condition describes the transport of particles at approach to a perfectly absorbing surface. While some researchers have assumed that all small particles adhere to the surface [133, 98], others have proposed a sticking efficiency for particle surface attachment [30, 21]. In order to capture phenomena like rebouncing and resuspension, it seems that more advanced versions of kinetic theory and molecular dynamics approaches [113, 65, 22] are needed, or better empirical models [18]. Nonetheless, this boundary condition can be easily imposed on the surface and does not require a fine mesh. The concentration profiles based on this concentration boundary condition at the wall is shown in Fig. 4.3

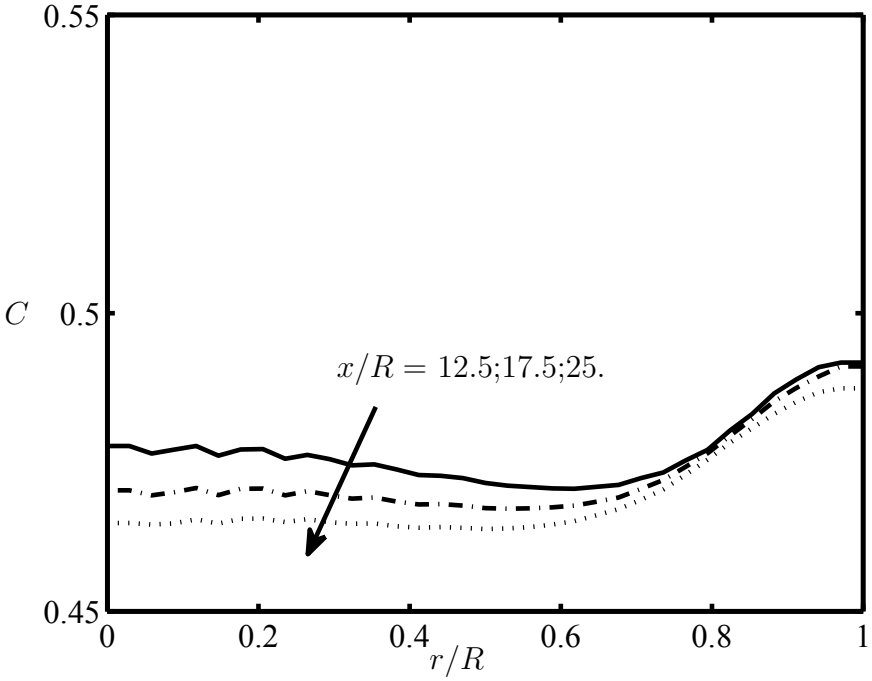

Figure 4.3: Development of concentration profiles along the tube at Re=300, Sc=120 based on the analogy to kinetic theory (Neumann boundary condition) at approach to the cold surface

4.1.4 The Extrapolation Boundary Condition

As the behavior of the particle concentration profile can be difficult to prescribe near the surface, a simpler approach is to impose a weak boundary condition, by extrapolating the concentration at the surface from its values further away. This scheme, which exploits the assumed smoothness of the particle concentration profile, is easy to implement and has low computational cost. The particular extrapolation scheme used is:

$$c(i, n_r) = 2.c(i, n_r - 1) - c(i, n_r - 2) \tag{4.5}$$

The density, velocity and temperature field were then solved over the computational domain with this concentration boundary condition and are shown in the following figures.

It can be seen from these figures that the effect of the extrapolation boundary condition is

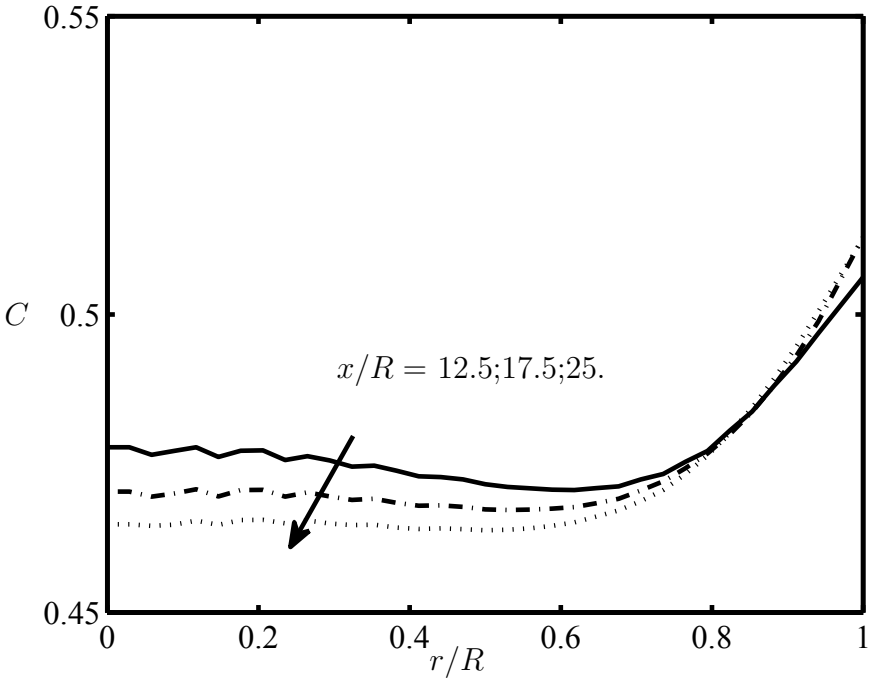

Figure 4.4: Development of concentration profiles along the tube at Re=300, Sc=120 based on the weak boundary condition at approach to the cold surface

restricted to the concentration boundary layer at the surface and scarcely affects the inner zone. The corresponding rate of particle deposition appears to be quite insensitive to the various boundary conditions applied at the surface(see Fig. 4.5)

4.2 Theoretical Concentration Profiles

Theoretical particle concentration profiles for fully developed pipe flow were presented in section 3.2.2, as a series solution to the governing thermophoretic particle transport equation. These results were based the assumption of no molecular diffusion beyond the surface sublayer, with particle transport driven only by convection and thermophoresis. In this case the transport equation is a first-order PDE which requires a single boundary condition in

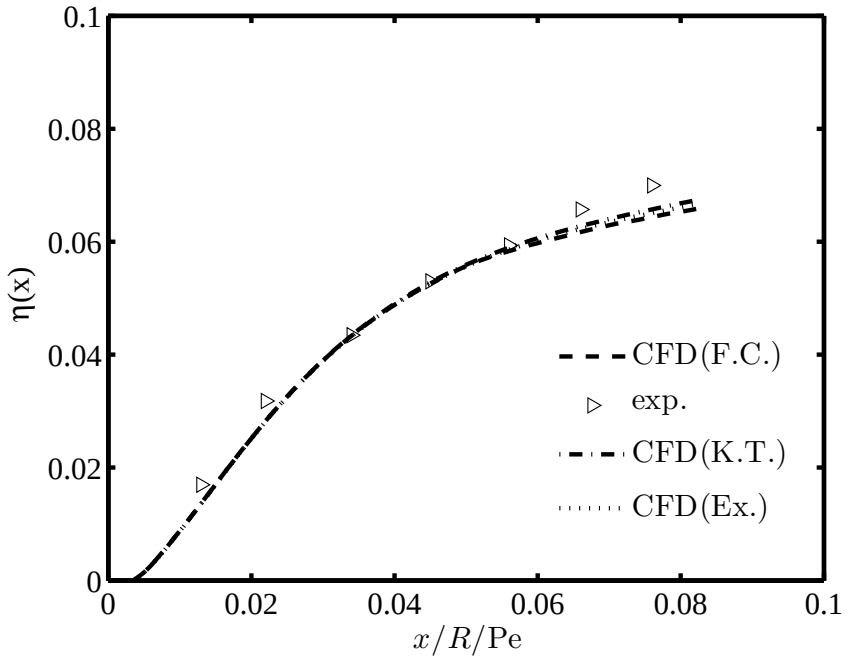

Figure 4.5: Effect of different boundary conditions on the overall deposition efficiency $\eta(x)$, in the entrance zone of a compressible flow at Re=300

the surface-normal direction. Therefore a symmetry boundary condition at the centreline is sufficient for the solution of particle transport PDE and the governing equations determine the behavior of concentration profiles at approach to the surface. The results presented in Fig. 3.11 show that the concentration profiles are smooth near the surface. It is also noticeable that although no Neumann condition is imposed at the cold surface, it appears that $\partial c/\partial y \simeq 0$. This observation is consistent with the boundary condition obtained from the analogy with kinetic theory, which may then be a reasonable approximation.

4.3 Concentration Profiles in Incompressible Flows

In this section, the concentration profiles deduced from numerical solutions to the incompressible particle transport equation are considered. The one-way coupling between the

particle transport equation and the thermal energy and Navier Stokes equations allowed the solutions for fully developed velocity and temperature profiles in a tube, described in section 3.2.2 to be used as inputs. The numerical code was therefore simple and fast and so, by decreasing the time steps sufficiently, it could solve for transport with infinitesimally small (Sc=10^5) diffusion in a reasonable time, without encountering stability problems. The boundary conditions described in the previous section were imposed on the cooled surface and the corresponding effect on the concentration profiles and the deposition efficiency was investigated. As discussed in the previous section, the c_s=0 wall boundary condition resulted in an extremely thin concentration boundary layer adjacent to the wall which required a very fine mesh. Its effect appeared to be limited to the immediate vicinity of the wall without having a noticeable effect on the concentration in the core region. This boundary condition results in a very slow computation, as noted by others [136, 137]. Other boundary conditions are discussed below:

A) Flux Conservation Boundary Condition:

The assumption of particulate flux conservation in the surface-normal direction results in the surface boundary condition: $\partial(r.c.v_{th})/\partial r = 0$, where v_{th} is the thermophoretic velocity. The concentration profiles calculated in this fully-developed incompressible pipe flow are shown in Fig. 4.6. It appears that spurious oscillations occur in the concentration field near the surface. These oscillations, which were not evident when the $c_s = 0$ condition was employed, imply that additional diffusional damping would be required for a flux-conservation boundary condition to be used effectively.

B) Extrapolation Boundary Condition:

The thermophoretic particle transport is a first order PDE and so it seems reasonable to assume that the particle concentration profile change smoothly/monotonically at approach

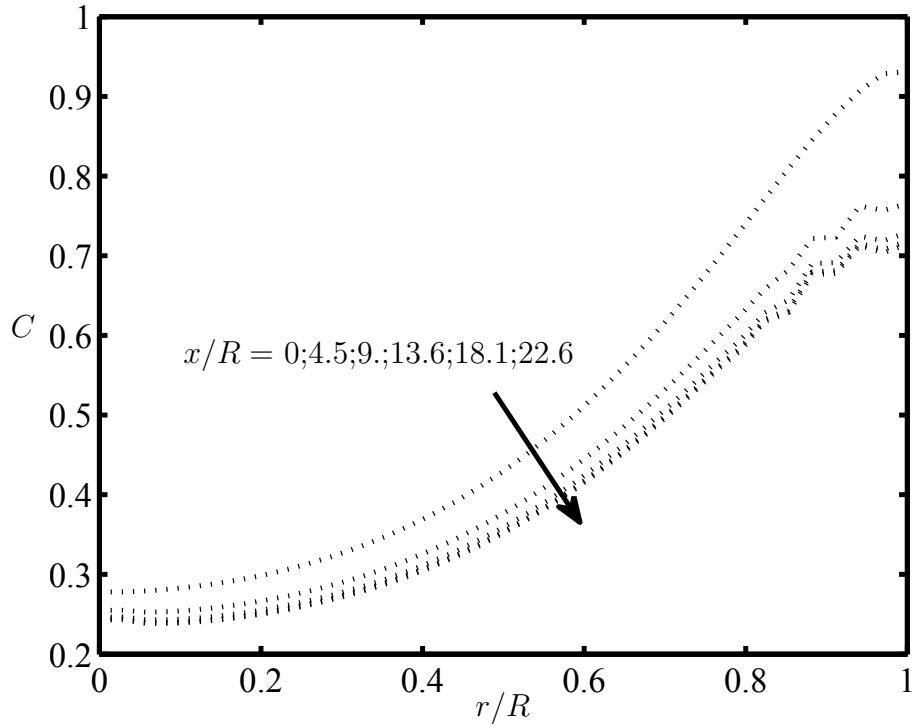

Figure 4.6: Development of concentration profiles along the tube at Re=30, Sc=∞, when a conservation of particle flux condition is applied at the surface

to the wall. This expected smoothness suggests that the concentration at the surface might be extrapolated from the near-surface concentration field. The extrapolation is similar to assuming a weak boundary condition on the surface and letting the governing equations decide the near wall behavior. The concentration profiles calculated with this boundary condition are shown in Fig. 4.7

C) Kinetic Theory Analogy:

By making an analogy between particles and molecules (with an assumed Maxwellian distribution), a general boundary condition was be derived which was simplified to the Neumann condition on the wall in the case of zero or infinitesimally small diffusion. The corresponding concentration profiles computed with this boundary condition are shown in Fig. 4.8. It is seen that the concentration profiles vary smoothly near the surface although there is no diffusion in the system. Thus this boundary condition yields physically plausible results in

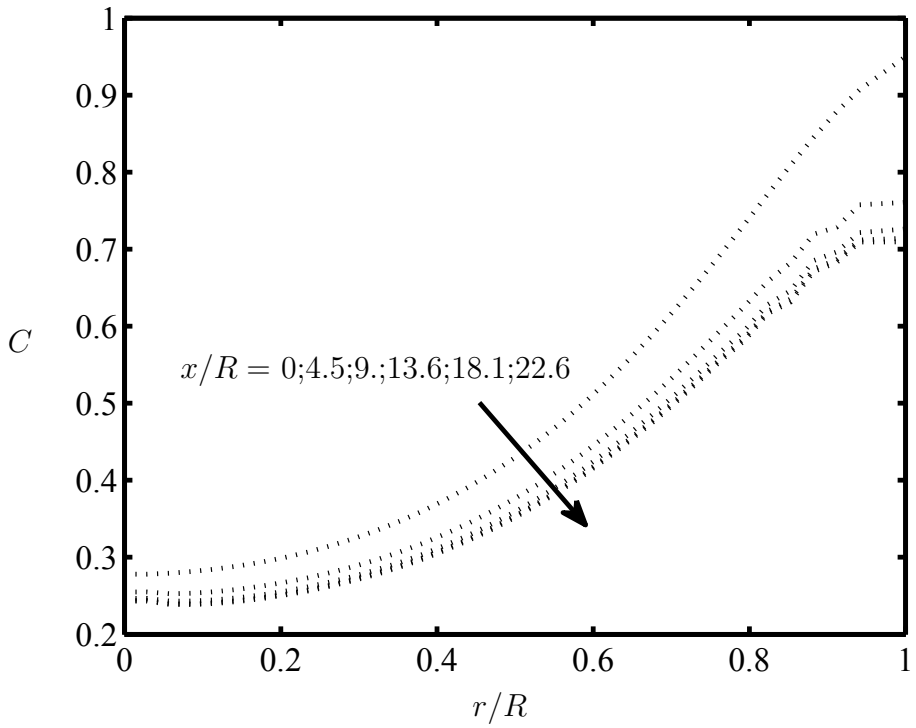

Figure 4.7: Development of concentration profiles along the tube at Re=30, Sc=∞ when a weak (extrapolation) boundary condition is applied near the surface

this fully developed flows. However, the validity of the analogy upon which the condition is based is questionable and more research into the physical basis for this boundary condition is required, as well as its testing in other flows.

The corresponding deposition efficiencies computed by each of these approaches are shown in Fig. 4.9. It is almost impossible to distinguish between these deposition efficiencies according to the boundary conditions used in their calculation, which tends to confirm that the effects of different boundary conditions are limited to the immediate vicinity of the surface.

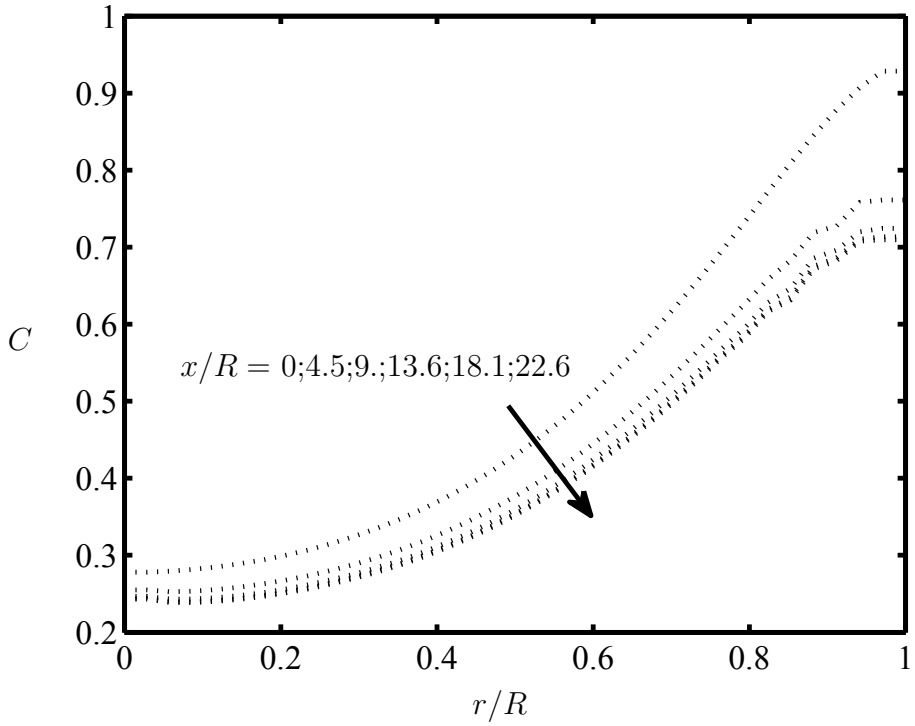

Figure 4.8: Development of concentration profiles along the tube at Re=30, Sc=∞ when a boundary condition based on an analogy with kinetic theory (Neumann condition) is applied at the surface

4.4 Discussion

There is currently no exact prescription for the concentration boundary condition at the surface in thermophoretic flows. Walker et al. [136] introduced the concept of a diffusion sublayer with a very small thickness δ_c adjacent to the surface, within which the particle concentration changes sharply from a finite value at the edge of the sublayer to zero at the wall. The particle flux towards the surface at the edge of the diffusion layer is $J_{\delta_c} = c_{\delta_c} v_{th}$ and the flux at the wall is $J_s = c_s v_{th} - D_B \frac{\partial c}{\partial r}$. The boundary layer approximation that $\partial J/\partial x \simeq 0$ requires that $\partial J/\partial y \simeq 0$, which leads to the conclusion that $J_{\delta_c} = J_s$. In other words, the particulate flux is almost constant within the diffusion layer and just changes from thermophoretic flux to diffusional flux. Thus the particulate flux may be determined at δ_c without solving the particle transport equation in the diffusion layer. It is for this

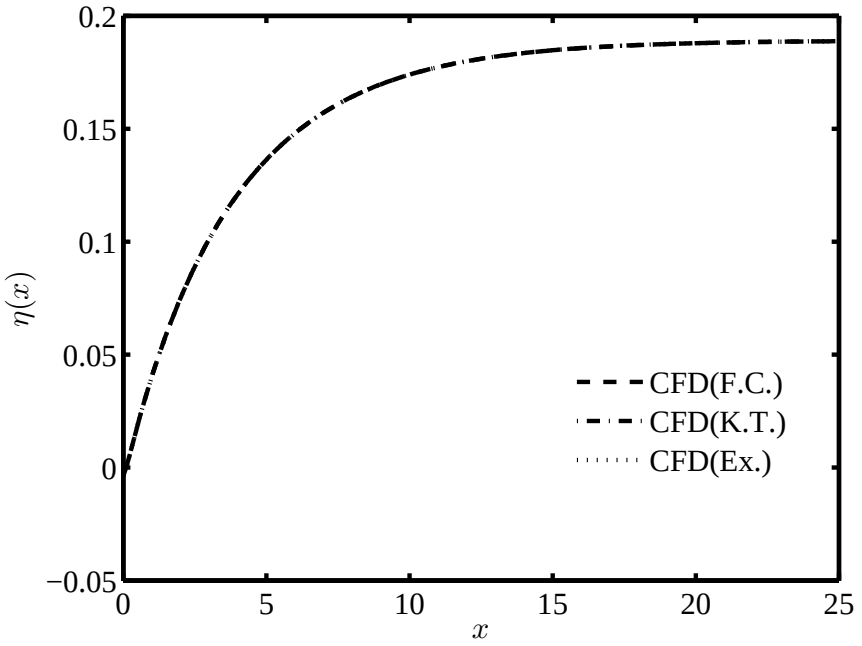

Figure 4.9: Effect of different boundary conditions on the overall deposition efficiency $\eta(x)$, in the fully developed region of an incompressible pipe flow at Re=30

reason that, in both the entrance zone and fully developed cases, it is seen that the overall deposition efficiency changes only slightly when a different surface boundary condition is used, even though there are more significant changes in the particle concentration profile.

The $c_s = 0$ condition appears to be a practical and reasonable boundary condition in case of small Sc numbers (Sc<20). For larger Sc numbers, it leads to the formation of an extremely thin diffusion layer which is hard to resolve at reasonable computational cost. The extrapolation of the concentration field at the surface is a weak boundary condition appears to yield reasonable results as the transport equation is a first order PDE and does not require a wall boundary condition. The Neumann boundary condition, which is a simplification deduced from an analogy between particle motion and the kinetic theory of molecules, yields concentration profiles which are quite similar to those computed using extrapolation. However, a more comprehensive study of this approach in a range of different flows is nec-

essary if further conclusions are to be drawn. The boundary condition derived based on the conservation of flux can also yield generally acceptable results, but it ca also causes spurious oscillations in the concentration field, especially at high particle Sc numbers. However, for high Sc numbers, the imposition of a weak boundary condition is easy to implement, and leads to smooth, accurate results and is recommended, while the widely-used $c_s = 0$ condition appears to give trustworthy results at lower Sc numbers (Sc<20).

Chapter 5

Thermophoresis in Steady Turbulent Flows

In the majority of industrial and scientific applications, the flows in which particulate transport takes place are turbulent. Thakurta et al. investigated the deposition of small particles in turbulent channel flows using direct numerical simulation [129]. They reported that in order to calculate the fluxes in turbulent flows, the coefficient of Brownian diffusivity D_B should be replaced by $(D_B + D_t)$ where D_t is the turbulent diffusivity, but the thermophoretic flux will stay proportional to kinematic viscosity ν and no modification is required to take care of turbulent effects. Thakurta et al. also noticed that in turbulent flows the thermophoretic flux changes due to changes in the mean temperature values and the effects of instantaneous oscillations in temperature will cancel out . These phenomena could be explained based on the fact that the logarithmic function decreases the amplitude of the temperature oscillation in turbulent flows and acts similar to a strong damper, so a good approximation of the mean temperature values would be enough for calculating the thermophoretic fluxes in turbulent flows. Dehbi [25] solved the Langevin equations for the turbulent flow velocities which were added to the mean velocity values obtained from the Fluent 6.3 commercial code. Dehbi applied his particle transport closure to several different problems with complex geometries and in each case found reasonable agreement with data

obtained by other methods [24, 23]. His simulations showed that for particles with short relaxation times such as soot, oscillations that appear as turbulent diffusivity have a considerable effect on simulation results. The most significant role of turbulent diffusivity is to smooth out concentration profiles, especially near the wall, which lowers the deposition efficiency (as shown in Fig. 5.1). Based on Dehbi's simulations of particles with short relaxation times, it appears that in turbulent wall-bounded flows, the concentration next to the wall is almost equal to the mixed-mean concentration c_m in the boundary layer. The time-averaged concentration field may then be modeled as if uniform in the surface-normal direction. However, larger particles were shown to accumulate near the wall. A similar trend is seen in the direct numerical simulation (DNS) results reported by Thakurta et al. [129]. Dehbi's results appear to explain why Romay's 1-D model, which is based on the assumption of a flat profile, can predict the deposition efficiency of sub-micron particles reasonably accurately [107].

$$\frac{dc_m}{dx} = -\frac{2}{U_m R}(J_r)_{r=R} \simeq -\frac{2c_m}{U_m R}(v_{th})_{r=R} \tag{5.1}$$

$$\frac{dT_m}{dx} = \frac{2Nu}{PeR}(T_s - T_m) \tag{5.2}$$

In wall-bounded flows, when condensation is negligible, diffusion acts to keep the concentration of particles uniform across the span of the flow, whereas thermophoresis drives particles from the hot gas towards the cold wall. The conservation of particle mass and the First Law of thermodynamics describing these processes may be written as: Eq. 5.2 may be integrated to evaluate the mean value of the temperature T_m at any longitudinal distance and can be

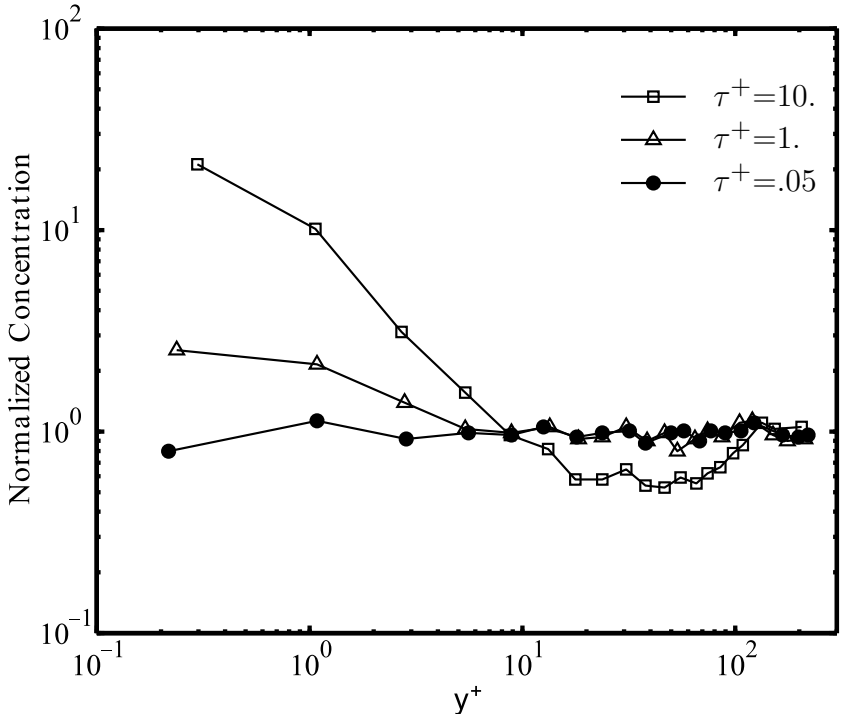

Figure 5.1: Normalized concentration profiles for different particle inertias (from [25].)

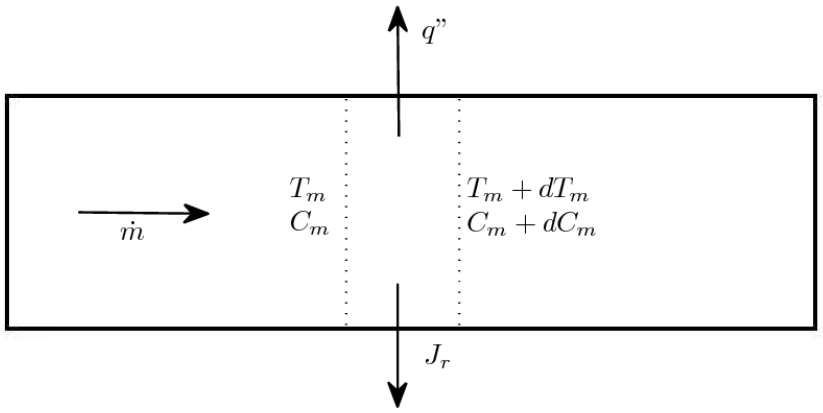

Figure 5.2: 1-D schematic of heat and mass transfer in a pipe

rewritten as:

$$\frac{T_m(x) - T_s}{T_o - T_s} = \exp\left(-\frac{1}{\dot{m} C_p \overline{R}_{tot}}\right) \tag{5.3}$$

where $\overline{R}_{tot} = \sum R$ is the total thermal resistance. As discussed in Chapter 2, the thermophoretic velocity may be written as:

$$v_{th} = -\frac{K_{th}\nu}{T}\frac{\partial T}{\partial r}. \tag{5.4}$$

Furthermore

$$k_f \left(\frac{\partial T}{\partial r}\right)_{r=R} = h(T_s - T_m) \tag{5.5}$$

so the thermophoretic velocity towards the wall is:

$$v_{th}|_{r=R} = \frac{K_{th}\nu h}{k_f}\left(1 - \frac{T_m}{T_s}\right) \tag{5.6}$$

where the convective heat transfer coefficient h can be found from several sources [117, 37] and k_f is the thermal conductivity of the flow. As the spanwise temperature gradient, which is the driving force for the thermophoretic deposition, can be especially high near the inlet, it is important to describe h accurately within the thermal entry region using relations reported in Kays [60, 54]. Based on the Graetz and extended Leveque solutions, Shah [115] reported the local Nusselt number in the thermal entrance zone of a tube to be:

$$\mathrm{Nu}_{x,T} = \begin{cases} 1.077(x^*)^{-1./3} - 0.7 & \text{for } x^* \leq 0.01 \\ 3.657 + 6.874(1000x^*)^{-0.488}\exp(-57.2x^*) & \text{for } x^* > 0.01 \end{cases} \tag{5.7}$$

and the mean Nusselt number to be

$$\mathrm{Nu}_{m,T} = \begin{cases} 1.615(x^*)^{(-1./3)} - 0.7 & \text{for } x^* < 0.005 \\ 1.615(x^*)^{(-1./3)} - .2 & \text{for } 0.005 < x^* < 0.03 \\ 3.657 + .0499./(x^*) & \text{for } 0.03 < x^* \end{cases} \tag{5.8}$$

where $x^* = x/D/\mathrm{Pe}$ and $\mathrm{Nu}_{x,T}$ and $\mathrm{Nu}_{m,T}$ are the local and mean Nusselt numbers respectively. Reynolds [106] proposed a relation for the turbulent thermal entrance length which can be combined with the Dittus-Boelter equation as:

$$\mathrm{Nu}_{x,T} = 0.023\mathrm{Re}^{0.8}\mathrm{Pr}^{0.3}\left(\frac{1 + 0.8(1 + 70000\mathrm{Re}^{-1.5})}{(x/D)}\right) \tag{5.9}$$

while the mean Nusselt number may be calculated by making use of Al-Arabi's relation as [3];

$$\mathrm{Nu}_{m,T} = 0.023\mathrm{Re}^{0.8}\mathrm{Pr}^{0.3}\left(1 + \frac{C_1}{(x/D)}\right) \text{ where } C_1 = \frac{(x/D)^{0.1}(0.68 + \dfrac{3000}{\mathrm{Re}^{0.81}})}{\mathrm{Pr}^{(1/6)}} \tag{5.10}$$

With these Nusselt number relationships, the heat-transfer coefficient h can be determined and substituted into Eq. 5.6, after which $c_m(x)$ can be found by integrating Eq. 6.7. The deposition efficiency $\eta(x)$ can then be evaluated as

$$\eta(x) = 1 - \frac{c_m(x)}{c_m(0)} \tag{5.11}$$

5.1 Comparison with Experimental Data for Turbulent Flows

In order to validate the capabilities of this uniform concentration model, we compare its predictions with published experimental data on turbulent flows. The data chosen are those of Romay's and the results of the turbulent-flow experiment TT28 of the TUBA program (the TUBA-TT28 data) [107, 52].

5.1.1 Comparison with Romay's Data

Romay et al. measured the deposition efficiency of particles in a 0.965 m long, 0.49 cm ID pipe. Their experiments were carried out in both the laminar and turbulent regimes, at Reynolds numbers of up to 9700. The particles used were sodium chloride or polystyrene latex spheres of 0.1–0.7 μm diameter and the deposition efficiency $\eta(\ell)$ was measured directly [107]. The measured values of $\eta(\ell)$ and the predicted values based on the 1-D model at Re$\simeq$ 5500 and 9700 at different inlet temperatures are plotted in Figs. 5.3 and 5.4. It is seen that the results of the 1-D model are in good agreement with the experimental data at both Reynolds numbers.

5.1.2 Comparisons with TUBA-TT28 Data

The TT28 is a test the TUBA programme in which the thermophoretic deposition has been measured in each of 13 sections of a 1 m long pipe of 1.8 cm ID. The aerosol used was CsI in a carrier gas of air that flowed at a Reynolds number of 4300. The results of the TUBA-TT28 experiment have been used widely to validate other deposition models [28, 52]. The corresponding values of $\eta(x)$ along the tube based on the 1-D model and the

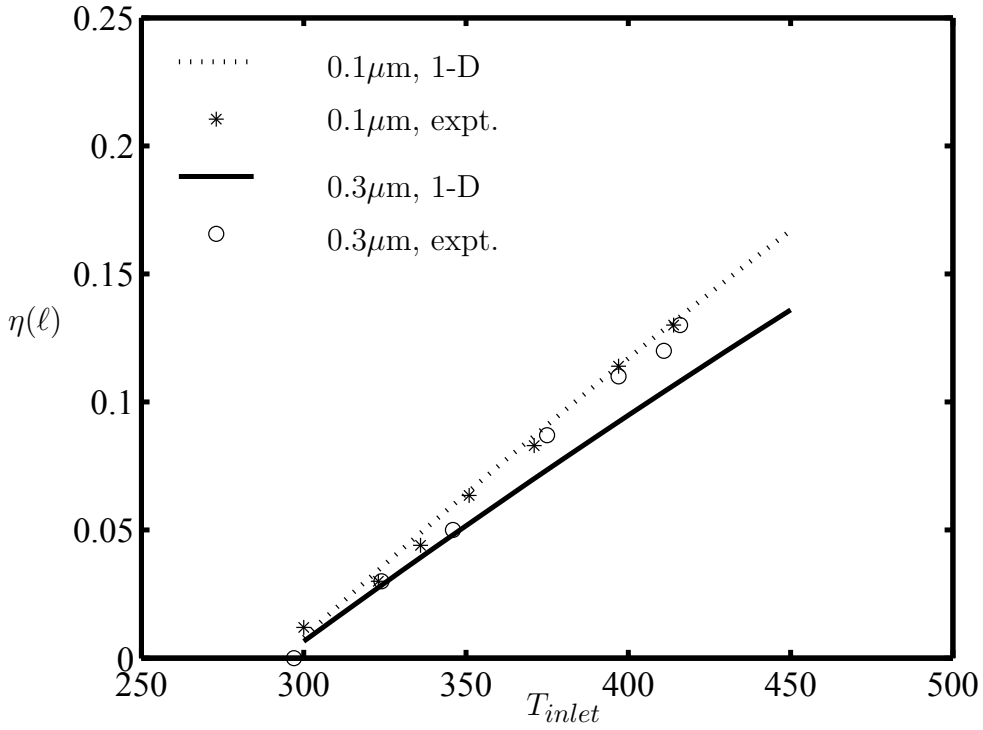

Figure 5.3: Deposition efficiency vs. inlet temperature for NaCl particles of 0.1, 0.3 μm diameter at Re=5500($\tau_p{}^+ = 0.016, 0.15$)

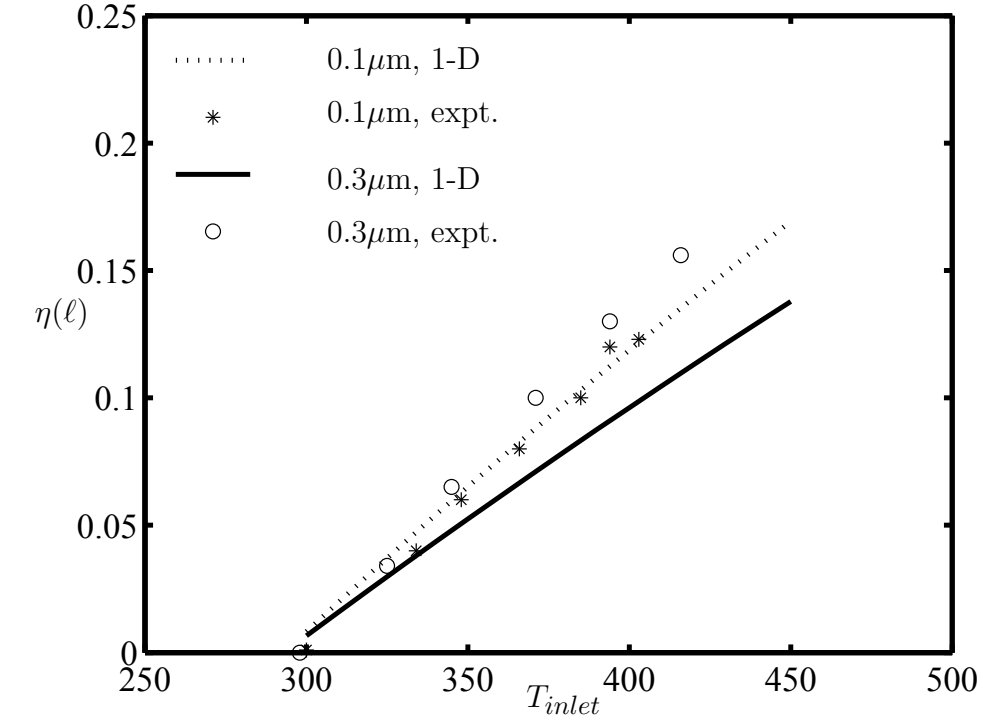

Figure 5.4: Deposition efficiency vs. inlet temperature for NaCl particles of 0.1, 0.3 μm diameter at Re=9700($\tau_p{}^+ = 0.04, 0.39$)

TUBA-TT28 data are shown in Fig. 5.5. The deposition-efficiency predictions of the 1-D

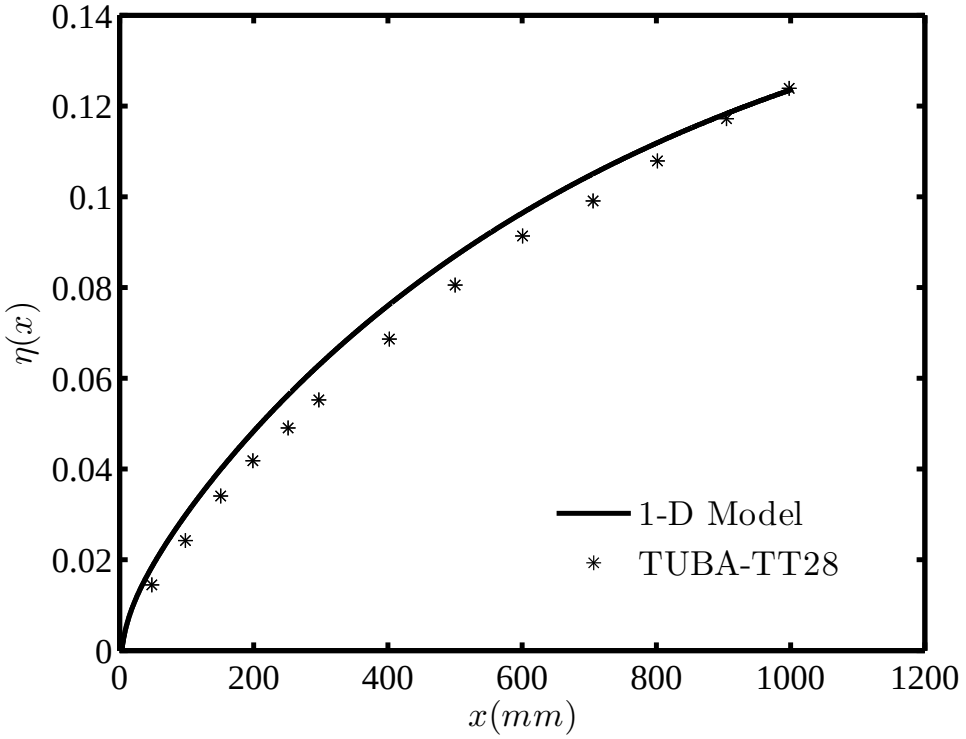

Figure 5.5: Deposition efficiency vs. longitudinal distance for CsI particles of 1.2μm diameter($\tau_p{}^+ = 0.115$)

model compare reasonably well with the experimental results. Although the diameter of the particles is greater than one micron, the particle relaxation time $\tau_p{}^+$ is still sufficiently small ($\tau^+ < 0.2$) that the assumption of a flat particle-concentration profile is a reasonable one.

5.1.3 Comparisons with Data for EGR Coolers

In the previous section, the comparisons between the predictions of the particle deposition model and experimental data implied it was an accurate method for approximating thermophoretic deposition of small particles in straight tubes. In this section, we use the particle deposition model to predict the soot-layer thickness in an EGR cooler after 2 and 5 hours of operation and compare the results with the experimental measurements of Ismail

et al. [56, 57] (Fig. 5.6). These results are plotted in the figure below and appear to be in good agreement with the experimental measurements. The model incorporates an empirical

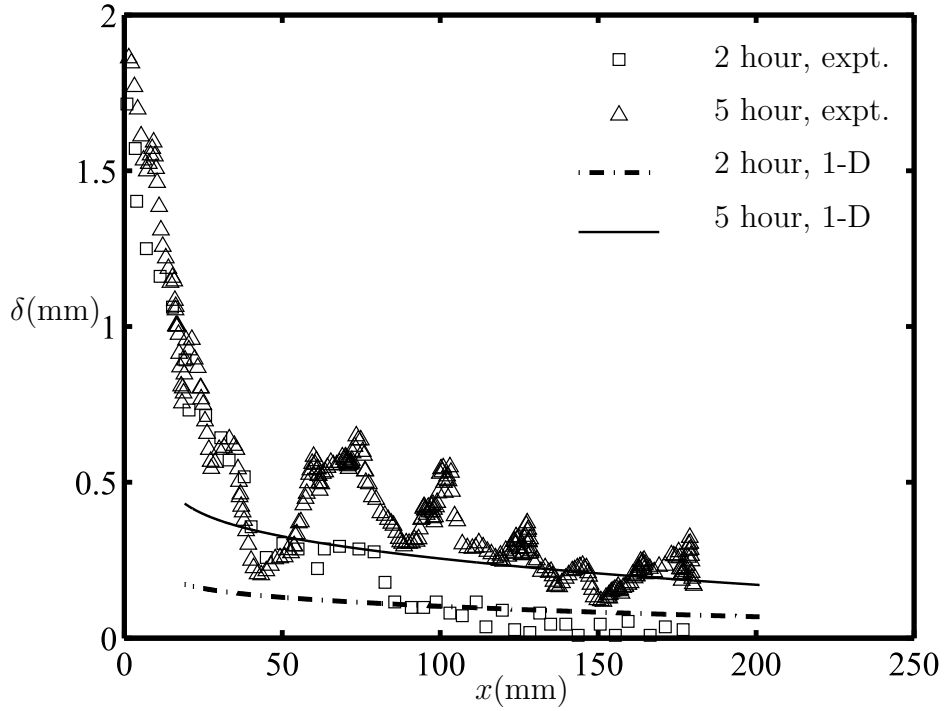

Figure 5.6: Comparison of predictions of a 1-D model with average soot thickness measurements along the EGR cooler using the neutron radiography technique [56] (Re=7000; 2 and 5 hours of operation.)

relation for Nusselt number, which is valid for $x/D > 3$. Near the entrance ($x/D < 3$) the Nusselt number increases sharply. The predictions of the one-dimensional model appears to be in reasonable agreement with the experimental data of Ismail [55]. Although the current model shares similarities with Romay's and Teng's methods [107, 128], its use of the uniform particle-concentration-profile assumption in turbulent wall-bounded flow is also consistent with the 3-D DNS results of Dehbi [25], and accounts for entrance zone effects. The effect of condensation is also important in the early stages of EGR operation and has been modeled with an empirical condensation correction factor $K_c \simeq 1.3$, which diminishes with time (see [89, 1] for more details).

Chapter 6

Thermophoresis in Unsteady Flows

In many applications such as respiratory systems, blood vessels, combustion engines and reciprocating pumps, the flow is oscillatory. There have been almost no studies of effects of unsteadiness on thermophoresis in such flows. The effects of axial flow unsteadiness on heat and diffusive mass transfer has been studied by several researchers, who have reported a variety of interesting results [68, 49, 8]. For example, the axial dispersion in capillary tubes has been reported to increase significantly under axially- oscillatory flow conditions in several studies [127, 139, 15]. The effect of flow pulsation on conductive heat transfer in tubes was also investigated by Kurzweg [69], who studied the axial heat exchanger in tubes, with axial flow pulsation but no mean convective mass transfer, as applied to the heating/cooling of hazardous materials, and observed that the pulsation led to the effective thermal diffusivity increasing to more than 10^4 times its molecular value. Kurzweg solved the energy equation for the oscillating flow within capillary channels analytically and reported a tuning effect where the maximum value of the corresponding effective thermal diffusivity occured at $\alpha^2.\mathrm{Pr} = \pi$, where α is the Womersley number $\sqrt{\nu/\omega}R$. This optimum value occured when the oscillation period and the transverse thermal diffusion time response were almost the same. Kurzweg also solved the problem of simpler counter-oscillating slug flow in a pipe with an imposed axial temperature gradient and flat velocity profile analytically and observed a similar tuning effect [68].

Faghri et al. solved the problem of fully-developed, axially pulsating flow in a heated

tube at low frequencies analytically and reported that small oscillations in flow velocity slightly increased the Nusselt number [32]. Kim et al. calculated the heat transfer in the entrance zone of a pulsating channel flow with constant wall temperature numerically [64]. Their results showed that the Nusselt number could either increase or decrease depending upon the values of the pulsating flow parameters, and that the variation was mostly in the developing zone, diminishing gradually along the tube. Moschandreou and Zamir presented an exact solution for the heat transfer in a fully-developed pipe with oscillating axial flow and constant heat flux [92]. Although Moschandreou's results confirmed that the heat transfer conductance could either increase or decrease depending on the flow parameters, they differed significantly from those of Kim et al. [64]. However, Moschandreou and Zamir's data did not show a cut-off frequency and but did reveal a singularity at Pr=0.5 at low frequencies, which appeared to be unphysical. Hemida et al. later showed that the approximations used by Moschandreou and Zamir to obtain results were not valid. They also obtained a new analytical solution to this problem and reported that the influence of axial pulsation on heat transfer conductance in the fully developed region of pipe flow was less than 1% [49].

Hemida et al. also solved the governing equations in the thermally developing zone using a finite element method (FEM), which led to results similar to those of Kim et al. [64] for pipe flow with a constant-temperature wall, and showed that the averaged Nusselt number could increase or decrease by up to 6% in the thermally developing region. Chattopadhya et al. solved the problem of axially pulsating flow in a heated pipe numerically, when the flow was both thermally and hydrodynamically developing and the tube wall temperature was uniform [14], and observed negligible enhancement in the time-averaged heat transfer. Guo et al. [42] also solved numerically for the heat transfer in an axially pulsating pipe flow with constant heat flux and found that any changes in the mean Nusselt number were small

(see Fig. 6.1). The discrepancy between their numerical prediction and the experimental measurements of Kim [63] at A=1.05, 2.05 was also small (< 2%). Yu et al. proposed an analytical solution for pulsating flow in a laminar tube with constant heat flux, and also found that axial pulsation had no effect on the time-averaged Nusselt number [146].

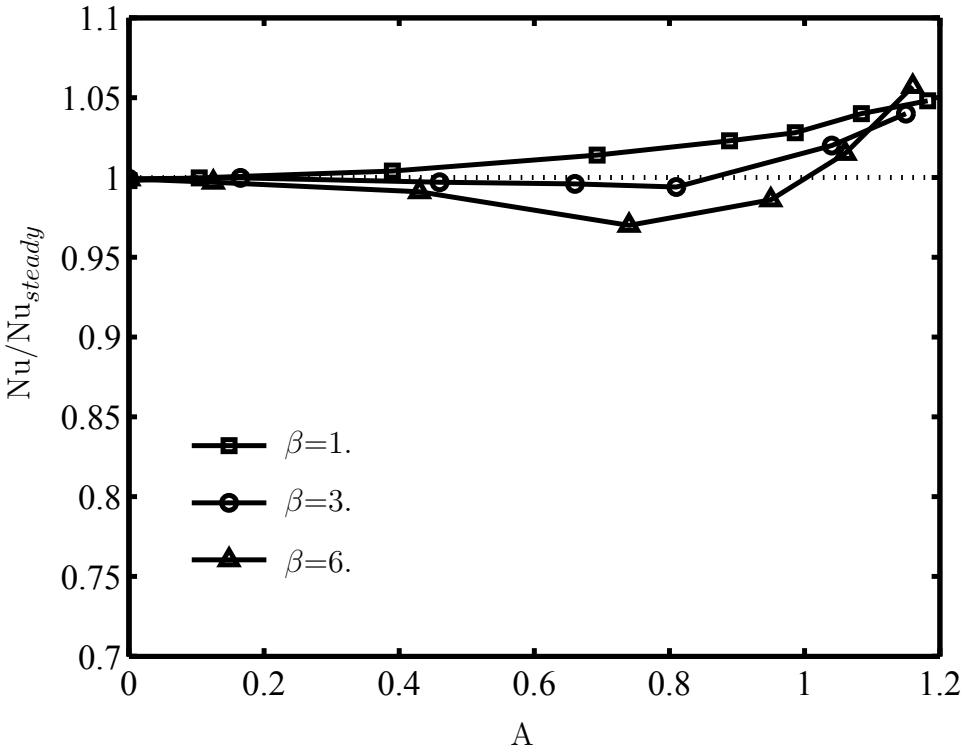

Figure 6.1: Variation of Nusselt number vs. pulsation intensity A (β is the Womersley number) [42]

Heat transfer in a pulsatile pipe flow with a uniform wall temperature was also studied experimentally by Gupta et al. [43]. They measured the variation of Nusselt number at different operating conditions and noticed that, at pulsation intensities of less than one, the changes in Nusselt number were small (Fig. 6.2). The behavior of laminar pulsating pipe flow inside a pipe with uniform heat flux was investigated experimentally by Habib et al. [45]. They reported that the Nusselt number could either increase or decrease with changing pulsation frequency and that the variations were slightly larger than those predicted

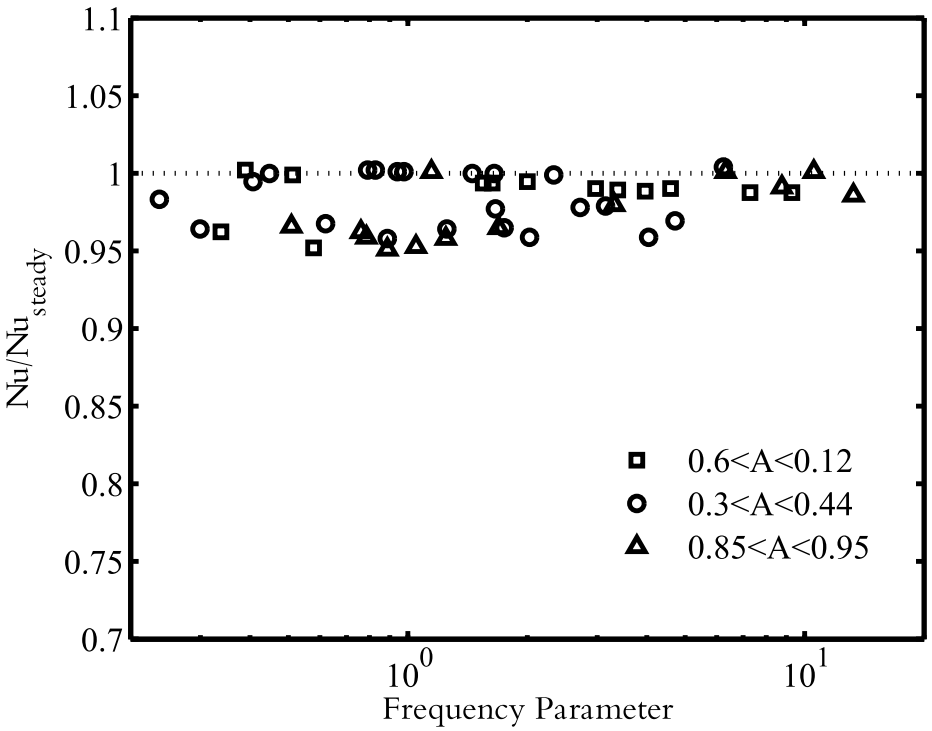

Figure 6.2: Variation of Nusselt number vs. normalized frequency parameter F_p corresponding to $0.13 < \omega < 0.35$ (experimental data reported by Gupta et al. [43]).

numerically by Hemida et al. [49] (Fig. 6.3), although the changes in the mean value of Nu over the corresponding range of Reynolds number (800< Re <2000) were still exceedingly small.

The effect of axial flow unsteadiness on heat transfer in turbulent flows was investigated by several researchers [59, 76, 36, 47, 46]. Liao and Wang [76] and Genin et al. [36] observed that at each Reynolds number turbulent bursts occur at a certain frequency and presented charts for evaluating the corresponding burst frequency (the interested reader is referred to [47] for more details). When the imposed pulsation frequency approached the turbulent bursting frequency, a resonance behavior occurred and the Nusselt number obtained its maximum value. This phenomenon was also reported in the measurements of Habib et al. [47, 46] (Fig. 6.4). They also noted that in the case of low Reynolds number flow, pulsation-dependent changes in the mean Nusselt number were insignificant.

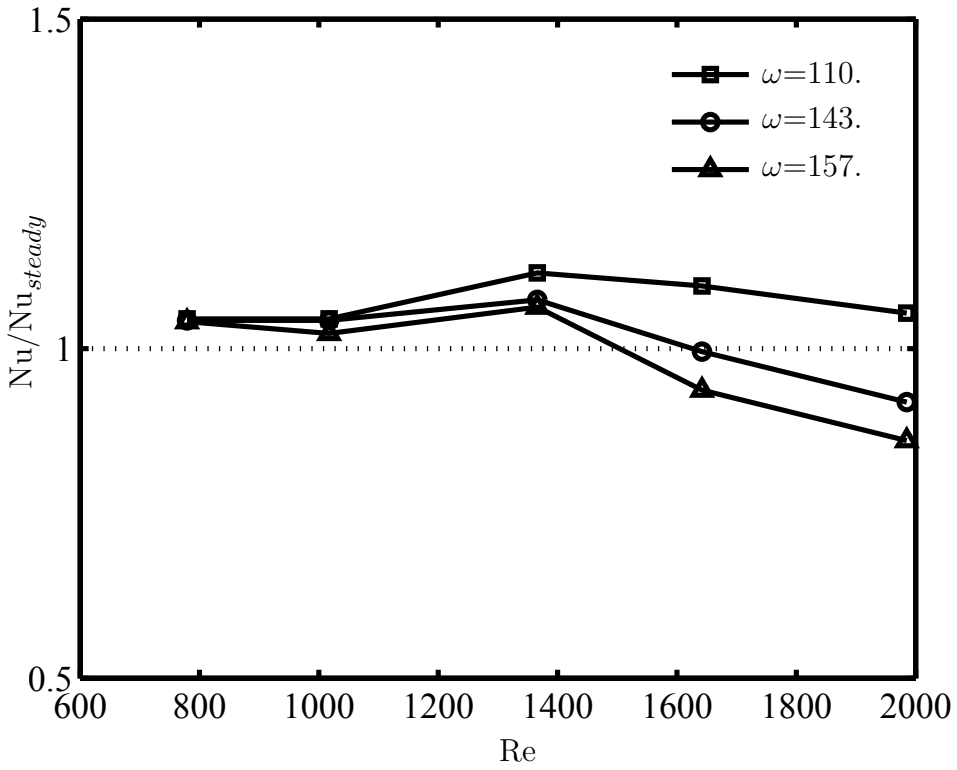

Figure 6.3: Experimental data on variation of Nusselt number vs. Re at different frequencies in laminar flows

The effect of boundary conditions was also investigated by Hemida et al., who reported that in the case of laminar flows with linear boundary conditions (linear combinations of temperature and temperature gradient), axial flow pulsation changed the heat transfer only slightly. When non-linear boundary conditions such as a radiation or a convective boundary condition apply, or non-linear phenomena such as turbulence are present, flow oscillations can potentially enhance the average Nusselt number. It has also been shown by Hafez and Montasser [35] that effects of compressibility may be important when the frequency of flow pulsation coincides with the natural frequency of the thermal-fluid system, which can lead to resonant effects. In many applications, the flow pulsation frequency is much lower that the natural frequency of the system and so effects of compressibility may often be neglected and the incompressible governing equations may be used without significant error.

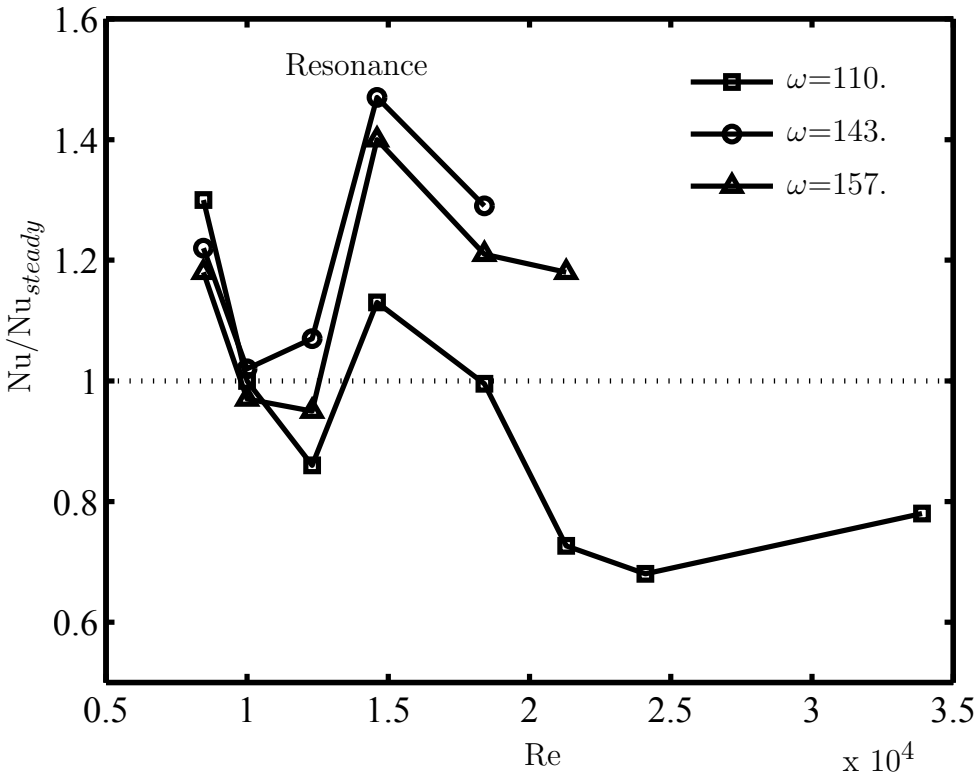

Figure 6.4: Experimental data on variation of Nusselt number vs. Re at different frequencies in turbulent flows

From the above discussion, it may be inferred that when flow oscillation takes place axially, in the direction normal to that of heat transfer, the change in heat transfer effectiveness is almost always negligible and no significant effect on thermophoretic mass transfer would be expected. On the other hand, when the directions of convective flow pulsation and heat transfer are aligned, the effective heat transfer can increase significantly and so changes in thermophoretic mass transfer would be expected too. In the following section, we investigate the effect of unsteadiness on heat and thermophoretic mass transfer.

6.1 Flows with Orthogonal Heat Transfer and Pulsation Directions

We consider an oscillating flow above a flat surface, when the directions of flow pulsation and heat transfer are perpendicular. This analysis extends that of Mao and Hanratty, who studied the effect of pulsating flows in heat and diffusional mass transfer in a boundary layer [83, 82], to include thermophoretic effects. It is assumed that the thickness of the thermal and concentration boundary layer is small enough that the effect of velocities normal to the wall can be neglected, so the streamwise velocity can be approximated as:

$$U = S.y \tag{6.1}$$

where S is the shear or velocity gradient at the wall. A harmonic velocity gradient is then imposed on the wall and changes with time as

$$S = \overline{S}(1 + A.sin(\omega.t)) \tag{6.2}$$

where $\overline{S}$ is the mean value of velocity gradient at the wall, ω is the frequency and A is the normalized amplitude of pulsation. The corresponding thermal energy equation is

$$\frac{\partial T}{\partial t} + S.y\frac{\partial T}{\partial x} = \alpha\frac{\partial^2 T}{\partial y^2} \tag{6.3}$$

with the boundary conditions

$$T(x, 0, t) = T_s,\ T(x, \infty, t) = T(0, y, t) = T_\infty. \tag{6.4}$$

The solution to this equation has been presented by Reiss [105] using a pseudo-steady state approximation as

$$\frac{T - T_s}{T_\infty - T_s} = \frac{1}{\Gamma(4/3)} \int_0^\eta e^{-z^2} dz \tag{6.5}$$

where

$$\eta = y \left(\frac{S}{9\alpha x} \right)^{1/3} \tag{6.6}$$

The particle transport equation is

$$\frac{\partial c}{\partial t} + S.y \frac{\partial c}{\partial x} = D \frac{\partial^2 c}{\partial y^2} + K_{th} \nu \frac{\partial}{\partial y} \left(\frac{c}{T} \frac{\partial T}{\partial y} \right). \tag{6.7}$$

The Schmidt number for submicron particles is very large and diffusion is negligible compared to thermophoresis. Walker et al. solved the corresponding steady mass transfer equation for submicron particles (Sc$\gg$1) in a wall-bounded flow including thermophoresis and imposed the c_s=0 constraint at the surface. Their results showed that, in steady flow, diffusion effects were limited to an extremely thin layer next to the surface over which there is an abrupt change in concentration from zero to a finite value [136]. The same trend is seen in the more recent results of Walsh et al. [137]. In case of negligibly small diffusion, the transport equation becomes a first-order PDE in which the particle concentration field has only a weak dependence on the wall boundary condition. In other words, at large Sc numbers the far-field condition is sufficient to solve for the entire domain and the effect of the wall boundary condition is be limited to an extremely thin layer. The same approach was used by Homsy et al., who also did not have to impose a c_s=0 condition in their analysis of a steady transverse flow past a cylinder [51]. Therefore, in this study, a weak condition (a Neumann condition) is used instead of the common c_s=0 condition, since it is expected, even in unsteady flow, to

have only a small effect on the corresponding particulate fluxes. The concentration boundary conditions are therefore

$$\frac{\partial c}{\partial y}(x,0,t) = 0,\ c(x,\infty,t) = c(0,y,t) = c_\infty. \tag{6.8}$$

When the governing equation is normalized with the length scale L and the velocity scale U_0, the non-dimensionalized constant-property thermal energy equation is

$$\frac{\partial T^*}{\partial t^*} + S^*.y^*\frac{\partial T^*}{\partial x^*} = \frac{1}{\mathrm{Re.Pr}}\frac{\partial^2 T^*}{\partial y^{*2}} \tag{6.9}$$

and

$$T^* = \frac{T}{T_\infty}, t^* = \frac{t.U_o}{L}, y^* = \frac{y}{L}, x^* = \frac{x}{L} \tag{6.10}$$

and the non-dimensionalized particle transport equation is

$$\frac{\partial c^*}{\partial t^*} + S^*.y^*\frac{\partial c^*}{\partial x^*} = \frac{1}{Sc.\mathrm{Re}}\frac{\partial^2 c^*}{\partial y^{*2}} + \frac{K_{th}}{\mathrm{Re}}\frac{\partial}{\partial y^*}\left(\frac{c^*}{T^*}\frac{\partial T^*}{\partial y^*}\right) \tag{6.11}$$

where

$$c^* = \frac{c}{c_\infty},\ \ S^* = \frac{S.L}{U_o} = \frac{\overline{S}.L}{U_o}(1 + A.Sin(St.t^*)) \tag{6.12}$$

The pulsation frequency is described by the non-dimensional Strouhal number St as

$$St = \frac{\omega.L}{U_o} \tag{6.13}$$

where ω is frequency, and L and U_o are length and velocity scales respectively. The thermophoretic flux is a nonlinear function of temperature and so normalizing the temperature

by T_∞ instead of $T_\infty - T_S$ leads to a simpler form of non-dimensional particle transport equation.

The local Nusselt number Nu_x can be obtained from the temperature profile and may be averaged over distance as the mean Nusselt number Nu, which represents effectiveness of the heat transfer. The mass transfer effectiveness or thermophoretic Sherwood number Sh_{th} (see Section. 3.2.2) is equal to $Nu.(c_s/c_m)$ in a pipe flow and may also be averaged over distance to describe the effectiveness of thermophoretic mass transfer.

A finite difference code was developed to compute numerical solutions to these transport equations. In order to validate the computational code, the solution to the energy equation under steady conditions was compared with the exact analytical solution (Eq. 6.5). It is seen that the numerical results are in excellent agreement with the exact solution (with a mean error smaller than 0.05%), so the developed numerical code was considered trustworthy. The calculated temperature and concentration contours are shown in Fig. 6.5 and Fig. 6.6 respectively. To the authors knowledge, this model problem has not been studied experimentally. However, the numerical heat transfer results for this laminar pulsating pipe flow, for either constant heat flux or uniform surface temperature, may be used for comparison and validation against analytical solutions such as those of Hemida et al. [49].

The validated CFD code was used to calculate the changes in heat and mass transfer effectiveness. The numerical domain size was $L \times 2L$, where L is the length scale. A uniform 100×100 grid was used to discretize the governing equations and the Reynolds number based on the length of the domain was equal to 150, with Pr=1. It is seen that the pulsation in wall shear stress lead to oscillatory heat and mass transfer coefficients, and changes are observed in their mean values. The amplitudes of the oscillation in heat and mass transfer coefficients are given as ΔNu and ΔSh_{th} respectively, while the mean values are normalized by the

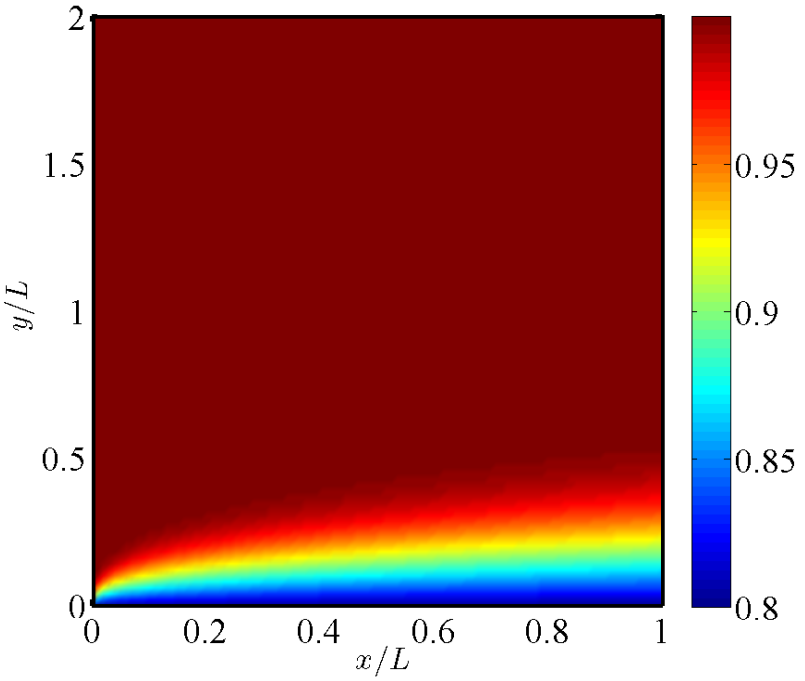

Figure 6.5: Contours of temperature at Re=150

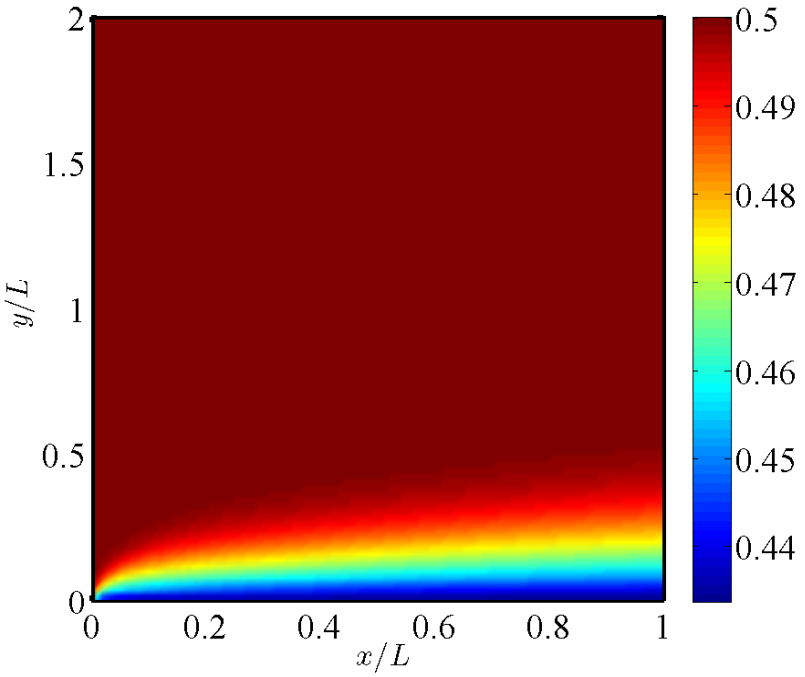

Figure 6.6: Contours of concentration at Re=150

steady values.

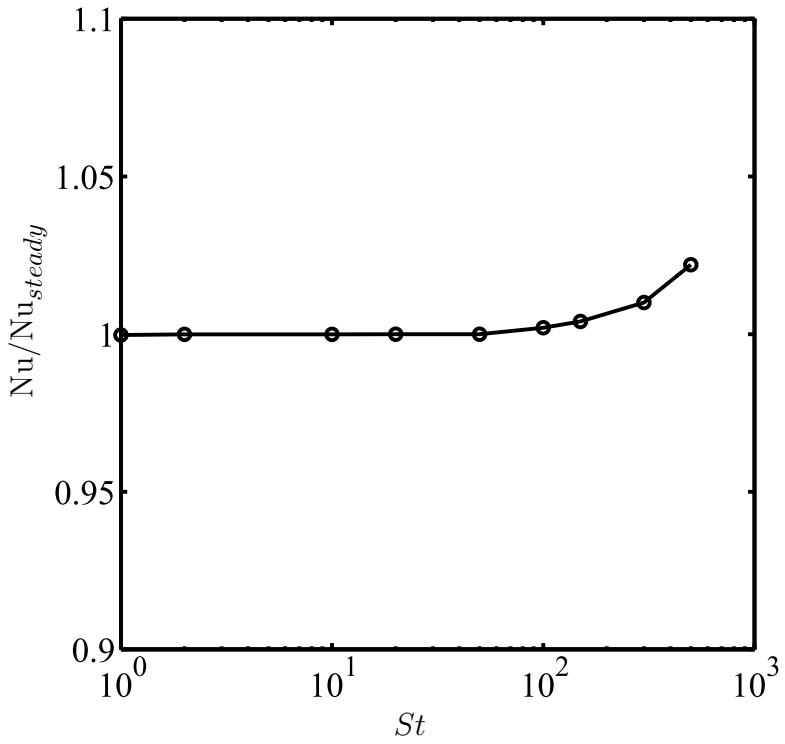

Figure 6.7: Effect of excitation frequency on the mean values of Nusselt number Nu

The numerical data shown in Figs. 6.7, 6.8, 6.9 and 6.10 are for the temperature ratio: $T_\infty/T_o = 1.25$, and very similar trends are seen for $T_\infty/T_o = 1.5$ and 1.75. The numerical values of ΔNu and ΔSh_{th} are less than 5% of the mean values at $St = 1$ and decay exponentially with increasing the frequency with a slope of -0.96 in both cases, when plotted in log-log coordinates. This decay with increasing excitation frequency is typical of physical systems with cut-off frequencies above which the pulsation is too fast to have a significant effect. In many engineering devices such as reciprocating engines, the Strouhal number St is greater than 10 and so the effect of pulsation on time-averaged heat and mass transfer coefficients is very small. These results are also in agreement with the observations of Gupta et al. [43] that effects of oscillation on mean Nusselt number are negligibly small (Fig. 6.2).

The parameter A is the ratio of pulsating to mean shear stress. In the numerical data

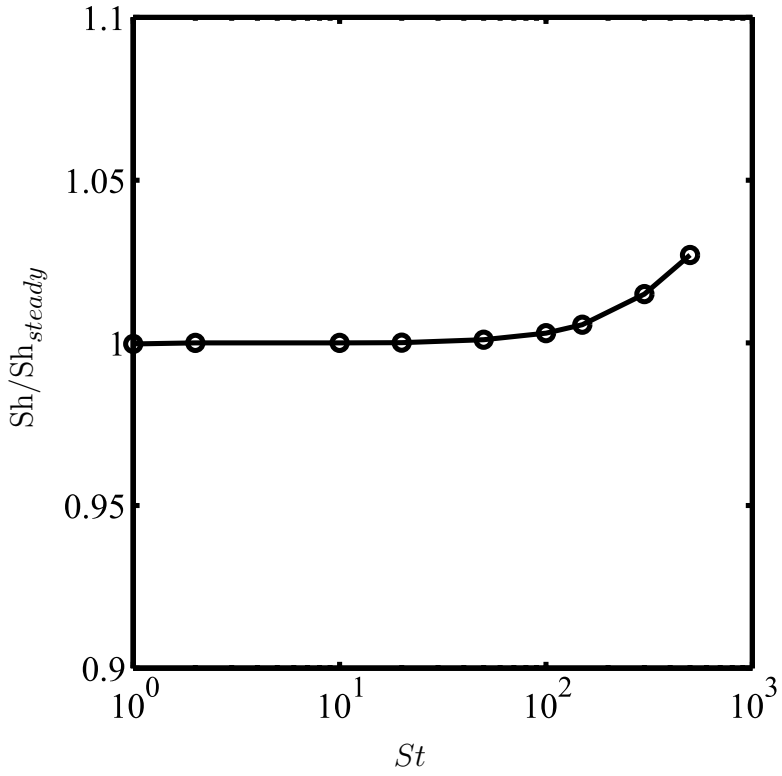

Figure 6.8: Effect of excitation frequency on the mean values of mass transfer effectiveness Sh_{th}

shown in Figs. 6.7, 6.8, 6.9 and 6.10, A was set to 0.3. The effect of A on heat and mass transfer coefficients at $T_\infty/T_o = 1.25$ and $St = 10$ is shown in Figs. 6.11 and 6.12.

It is clear that increasing the pulsation intensity A has negligible effect on the mean values of heat and mass transfer coefficients, which is consistent with the findings of Guo et al. [42] and the experimental measurements of Kim [63] (at $A < 1.1$ in Fig. 6.1). The amplitudes of oscillations in heat and mass transfer effectiveness $\Delta Nu, \Delta Sh_{th}$ increase linearly as, at higher values of A, there is more mixing in the flow so ΔNu and ΔSh_{th} increase. However, as the steady values of the heat and mass coefficients are 5.13 and 4.59 respectively, it is clear that in laminar flows, even at a pulsation intensity of $A = 0.5$, the changes in Nu and Sh_{th} are less than 1% of their steady values.

These numerical results are almost identical to the analytical results for steady flow and

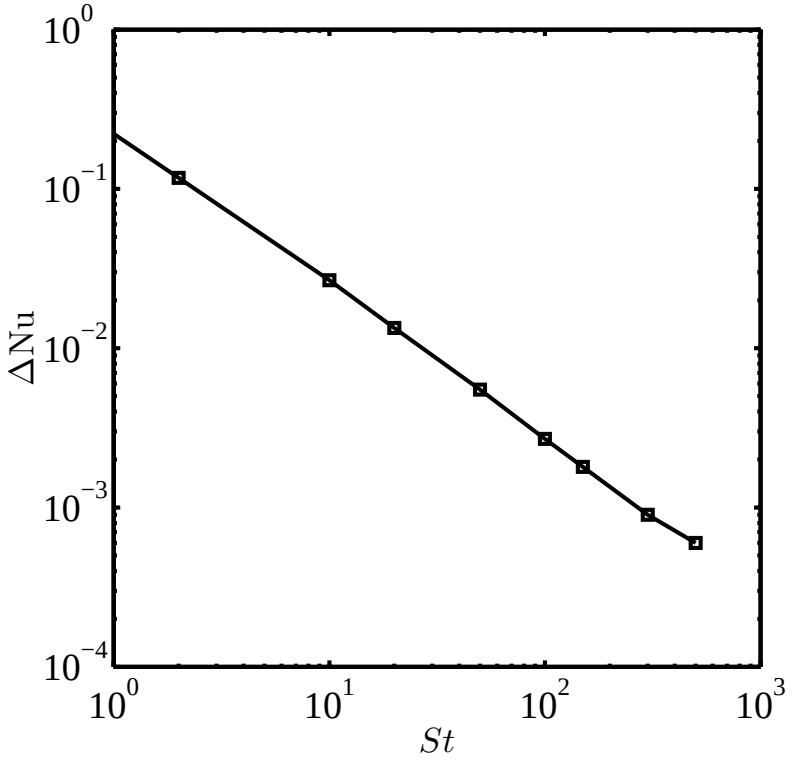

Figure 6.9: Effect of excitation frequency on the amplitude of subsequent oscillation in Nusselt number Nu

consistent with the observations of Hemida et al. [49] and Kim et al. [64] on the negligibly small effect of pulsation on heat transfer. The experimental measurements of Habib et al. [45] also support the finding that the variation in mean Nu due to pulsation is small. Their experimental results show larger variations in Nu compared to our results and other numerical data [49, 64], which may be due to the oscillating mechanism used or measurement uncertainty. In general the numerical results on heat and mass transfer effectiveness are in good agreement with the existing experimental data [45] and confirm that axial pulsation has a negligibly small effect on heat and thermophoretic mass-transfer phenomena.

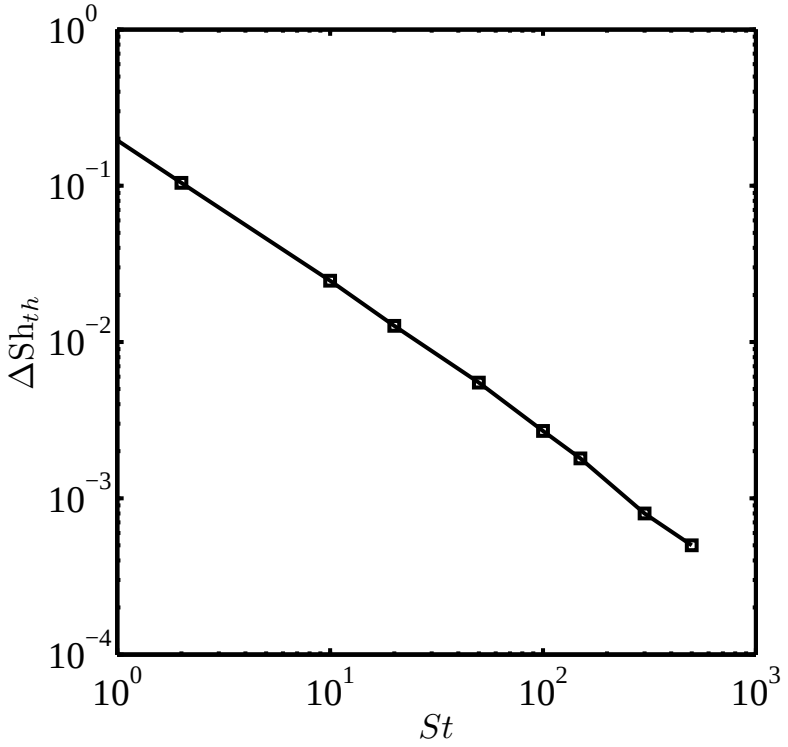

Figure 6.10: Effect of excitation frequency on the amplitude of subsequent oscillation in mass transfer effectiveness Sh_{th}

6.2 Flows with Aligned Heat Transfer and Pulsation Directions

In this section, the effect of flow pulsation is studied numerically when the directions of heat transfer and pulsation are aligned. The first model problem to be discussed is the counter-oscillating slug flow, which has been solved analytically for the case of heat transfer [68]. The second model problem is channel flow with an imposed pulsating velocity, which is more relevant to industrial applications.

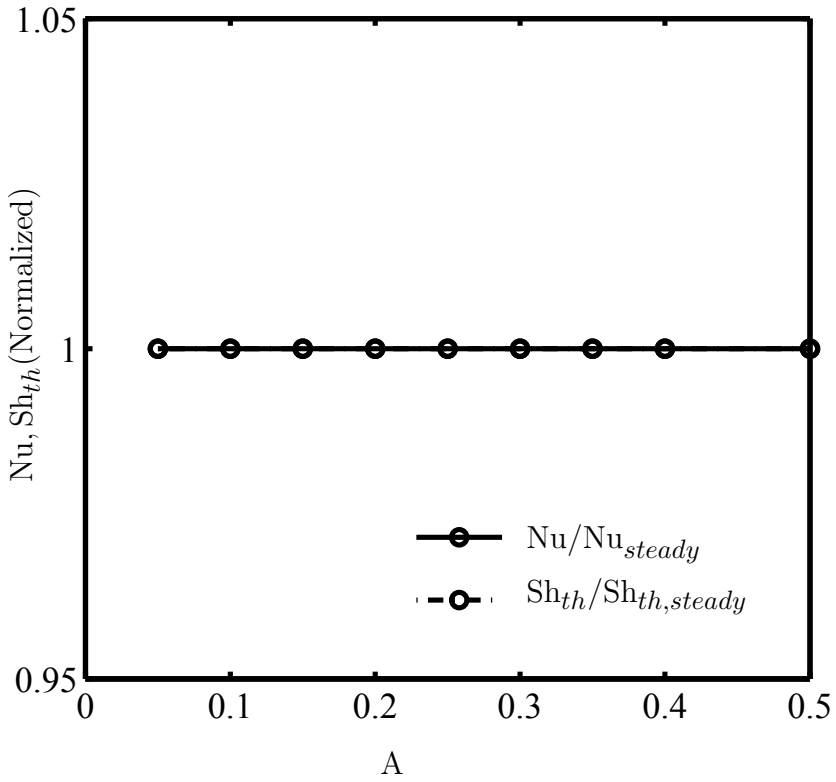

Figure 6.11: Effect of pulsation intensity A on mean value of subsequent oscillation in heat and mass transfer coefficients

6.2.1 Thermal and Thermophoretic Enhancement in Counter Oscillating Slug Flow

As stated above, Kurzweg et al. studied the effect of oscillatory flow on heat transfer when the direction of flow oscillation was aligned with the direction of heat transfer and reported that, because of the nonlinear term $u\dfrac{\partial T}{\partial x}$, the axial conductance was significantly enhanced. The model problem that Kurzweg analyzed was that of a counter-oscillating slug flow, shown in Fig. 6.13. The effective thermal diffusivity is equivalent to the effectiveness of heat transfer and is defined as

$$\lambda = -\frac{1}{2\pi\gamma(\triangle x)^2}\int_0^\tau \left(\int_o^1 [U]_R[T]_R d\eta\right) dt \tag{6.14}$$

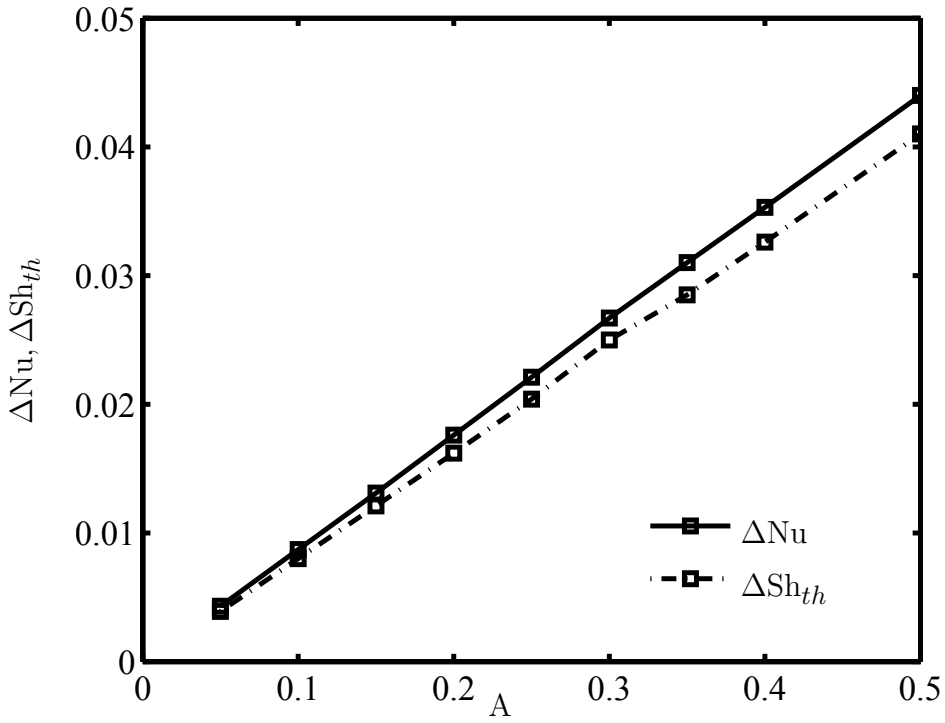

Figure 6.12: Effect of pulsation intensity A on amplitude of subsequent oscillation in heat and mass transfer coefficients

where the subscript R represents the real part of a complex number. Kurzweg simplified the governing equations and presented an exact solution for the problem and calculated the effective thermal diffusivity λ to be

$$\lambda = \frac{1}{8\beta}(\sqrt{i}.tanh\sqrt{i}\beta)_R \tag{6.15}$$

Eq. 6.15 shows that there is a tuning effect whereby the effective thermal diffusivity can be adjusted to take its maximum value at the particular oscillatory frequency $\beta = 1.59$, where $\beta = a\sqrt{\omega/\alpha}$ [68]. A numerical code was developed which could solve the exact transport equations for this problem. They were solved for the case of channel flow, with a plate at $y = 0$, with values of velocity taken from the exact solution to the momentum equation. It may be seen that the effective thermal diffusivity follows a similar trend to that found for

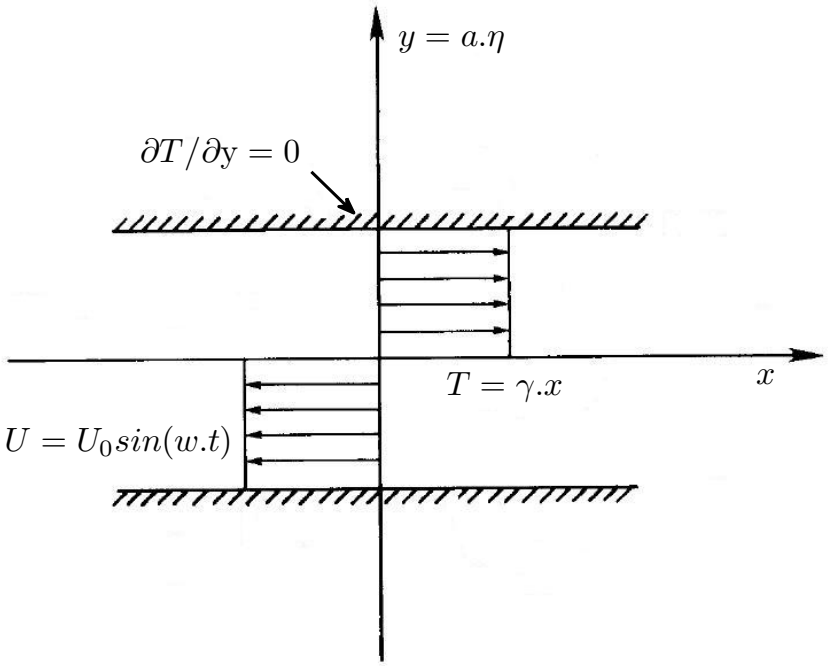

Figure 6.13: The counter oscillating slug flow analyzed by Kurzweg et al. [68]

slug flow, and that discrepancies between the exact solution and the numerical data for slug and channel flow are negligibly small (Fig. 6.14).

In a manner analogous to the definition of effective thermal diffusivity, the effective thermophoretic diffusivity λ_{th} may be defined as

$$\lambda_{th} = -\frac{1}{2\pi\gamma_c(\triangle x)^2}\int_0^\tau \left(\int_o^1 [U]_R[C]_R d\eta\right) dt \tag{6.16}$$

where $\triangle x$ is the tidal displacement, and γ and γ_c are the steady-state slopes of the temperature and concentration respectively. The numerical code was used to solve the particulate transport equation which included the thermophoresis term. The numerical results show that a similar tuning effect is seen for the effective thermophoretic diffusivity λ_{th}, which might have been anticipated since thermophoresis is driven by the temperature gradient. It is also noticeable that axial flow pulsation can enhance the thermophoretic transport by

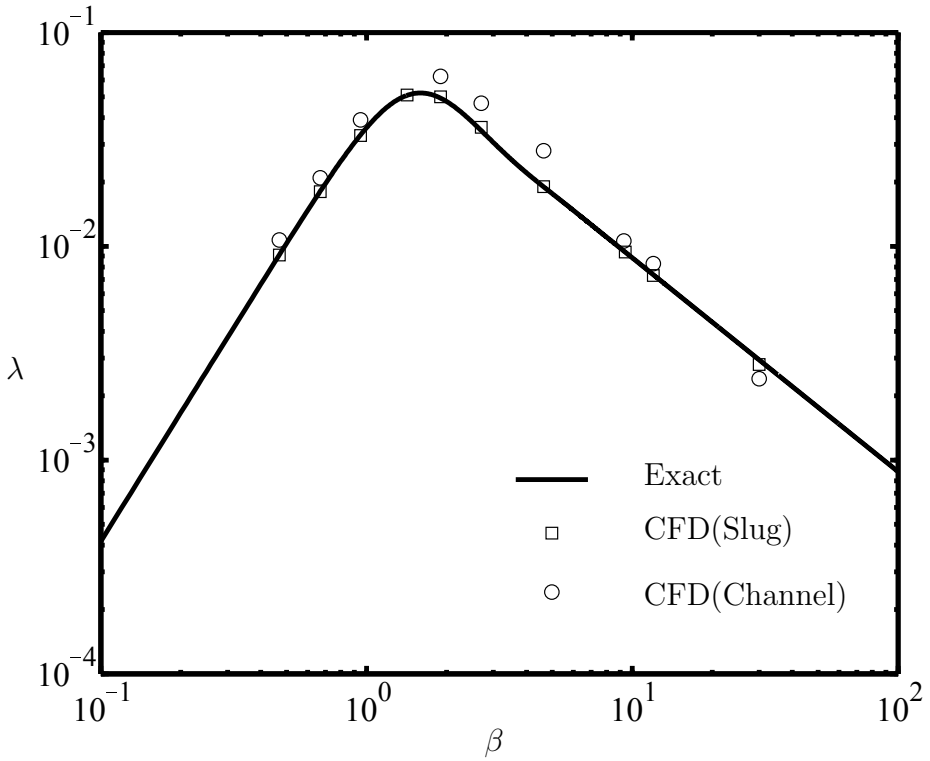

Figure 6.14: Comparison between the values of the effective thermal diffusivity based on exact and numerical solutions

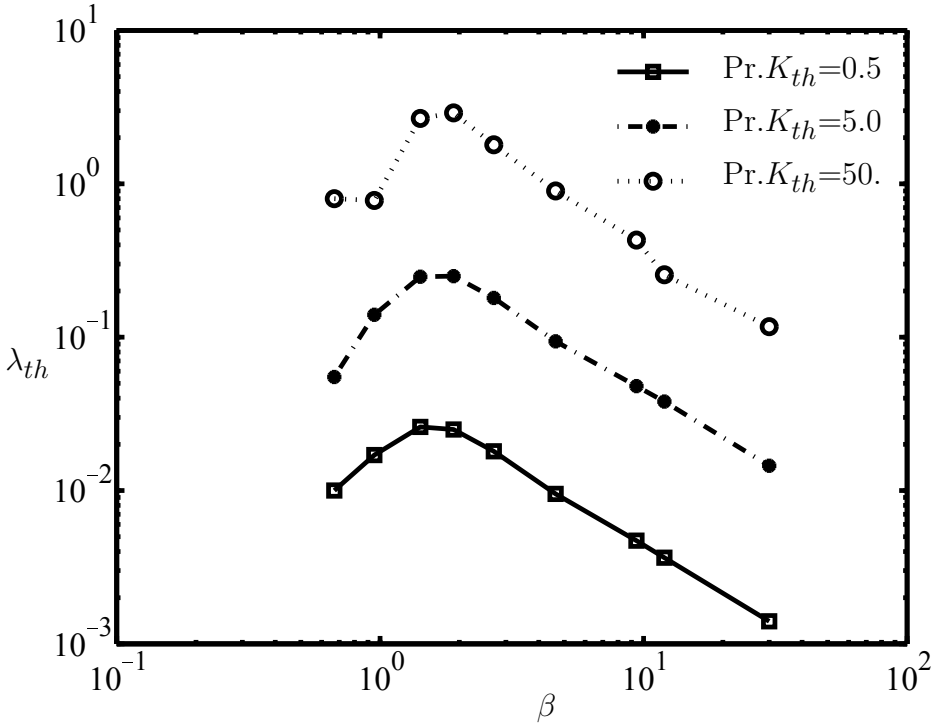

Figure 6.15: Numerical values of the effective thermophoretic diffusivity λ_{th} for different values of Pr.K_{th}

up to 3 orders of magnitude. Since the magnitude of the thermal 'force' is proportional to $\nu.K_{th}$, it may be seen that increasing Pr.K_{th} will enhance λ_{th} (Fig. 6.15). Numerical data for lower values of the frequency parameter β indicate that at high values of Pr.K_{th} the thermophoretic force could be higher than the force required to produce a uniform concentration profiles, and could in theory lead to inverse mass transfer ($\lambda_{th} < 0.$). This phenomenon is not possible in the absence of thermophoresis, as an infinite Brownian diffusion coefficient would be required to provide the flux necessary for a uniform radial concentration—where λ_{th} approaches zero.

6.2.2 Thermal and Thermophoretic Enhancement in a Vertically Pulsating Channel Flow with Porous Walls

The numerical simulations of the previous section on counter-oscillating slug flow have provided new findings on the effects of pulsation on thermophoresis. Although the slug flow studied is a simple model problem, such a flow could not be realized in practice because the shear stress at the centreline which would cause a Kelvin-Helmholtz instability. In the current section, we investigate the effects of pulsation on thermophoresis in a more practical model problem which is a channel flow that is a closer representation of heat-exchanger flows. In order to obtain an amplifying effect on heat conduction near the surface, it is assumed that a pulsating velocity is being imposed perpendicular to the direction of the bulk flow. It is assumed that the walls of the channel are porous and that the vertical velocity v could be imposed either by acoustic waves or by a pulsating flexible membrane which achieves its highest velocity in the center of the pores and recedes to zero away from the pores. It is also assumed that the pores are directly opposite each other on both sides of the channel and that the magnitude of the vertical velocity v changes smoothly from zero to its corresponding value (as shown in Fig. 6.16. The horizontal velocity u is assumed to be that of a steady, laminar, constant-property, fully-developed channel flow:

$$u = \frac{3}{2} U_m (1 - y^{+2}) \tag{6.17}$$

where U_m is the average velocity, $y^+ = y/H$, and H is the half width of the channel. The vertical velocity v is assumed to be zero at the solid parts of the intermittently porous wall, while it reaches its maximum value V_0 between each pore. The corresponding thermal energy

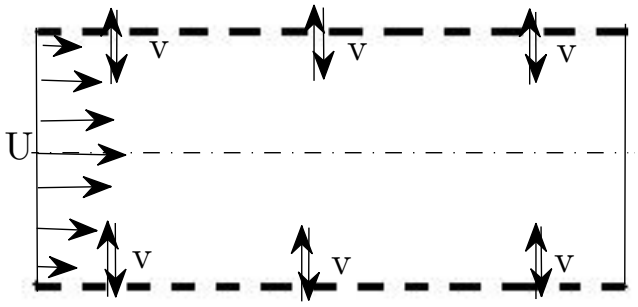

Figure 6.16: The pulsating vertical velocity v in a channel with porous walls

equation is

$$\frac{\partial T}{\partial t} + u\frac{\partial T}{\partial x} + v\frac{\partial T}{\partial y} = \alpha\left[\frac{\partial^2 T}{\partial x^2} + \frac{\partial^2 T}{\partial y^2}\right] \tag{6.18}$$

on which a symmetry boundary condition has been imposed at the centreline, while the Dirichlet condition has been imposed on the solid wall and the temperature between each pore has been extrapolated. The thermal energy equation was solved numerically and, based on the decay of the time-averaged value of the mixed-mean temperature, the effective Nusselt number was evaluated (Fig. 6.17).

In the studies of Kurzweg et al. [68], it was seen that when the time required for thermal diffusion over the width of the channel and the pulsation period coincide, a tuning effect was observed and the heat transfer improved significantly. In the case of channel flow with a horizontal bulk flow, thermal transport by convection is much faster than thermal diffusion. Therefore, in order to obtain an equivalent enhancement effect, the frequency of pulsation should be very high (see Fig. 6.17). However, the required vertical velocities V_0 at high frequencies would be so high (see Fig. 6.18) as to surpass the laminar threshold. The

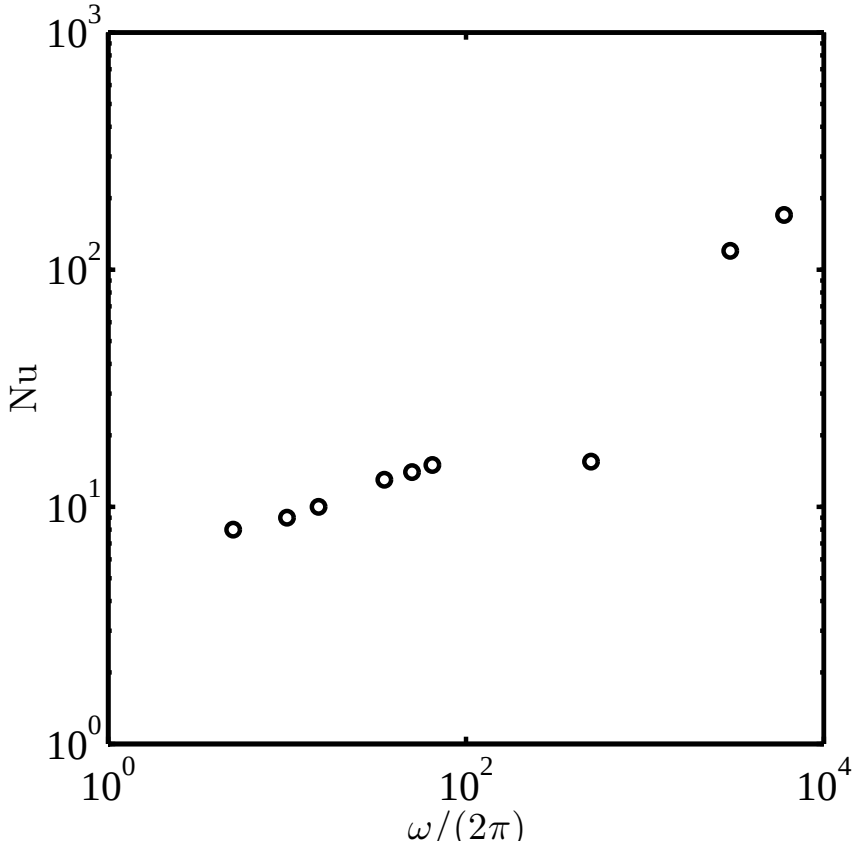

Figure 6.17: Variations in Nusselt number at different frequencies.

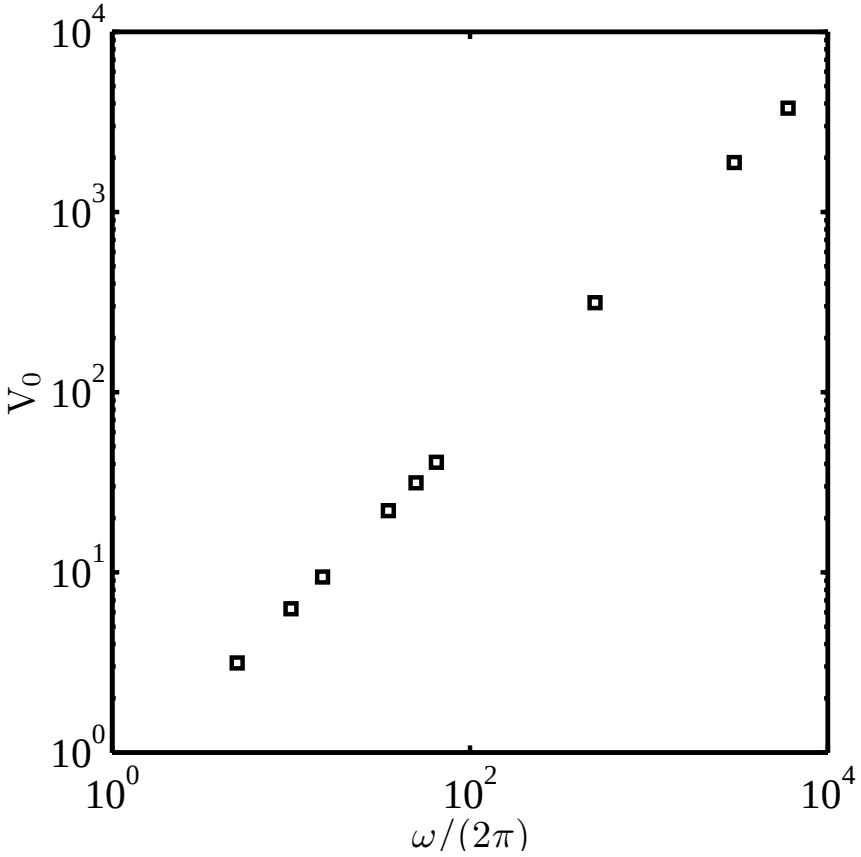

Figure 6.18: Variations in the maximum vertical velocity at different frequencies.

required mass flow rates through each porous wall would be implausibly high.

The thermophoretic particle transport equation for this problem is

$$\frac{\partial c}{\partial t} + u\frac{\partial c}{\partial x} + v\frac{\partial c}{\partial y} = D\left[\frac{\partial^2 c}{\partial x^2} + \frac{\partial^2 c}{\partial y^2}\right] + K_{th}\nu\left[\frac{\partial}{\partial x}\left(\frac{c}{T}\frac{\partial T}{\partial x}\right) + \frac{\partial}{\partial y}\left(\frac{c}{T}\frac{\partial T}{\partial y}\right)\right] \tag{6.19}$$

Again, a symmetry boundary condition is imposed on the centreline, while extrapolation is applied at the walls. It is assumed that all the particles that enter the pores of the porous wall attach to the surfaces and get trapped in porous media, so the concentration of the flow coming out of the walls would be equal to zero. In other words, the porous wall behaves as a side filter which traps all particles. The Eulerian approach is capable of capturing the filtering effect of walls at low frequencies but at higher frequencies ($St > 5$) the numerical code diverges. The divergence of the numerical code may be explained based on the fact that at higher frequencies the cleaning effect of the side walls is much stronger and leads to the formation of a void region near the surface which is similar to a jump and cannot be properly handled by the Eulerian solvers (see Fig. 6.19). Therefore a Lagrangian solver was developed which could solve for the transport of particles at high frequencies. The results showed that shortly after the entrance, the void region formed with a thickness of δ_v, and the mean concentration dropped sharply over a very short distance beyond the entrance zone. The mean concentration also decreased with axial distance in a similar manner to a channel flow with no pulsation. A more comprehensive study on the concentration profiles and mass transfer effectiveness in the channel based on the Lagrangian approach is necessary to further understanding of such flows in which particle voids develop, and is recommended as a topic for future research.

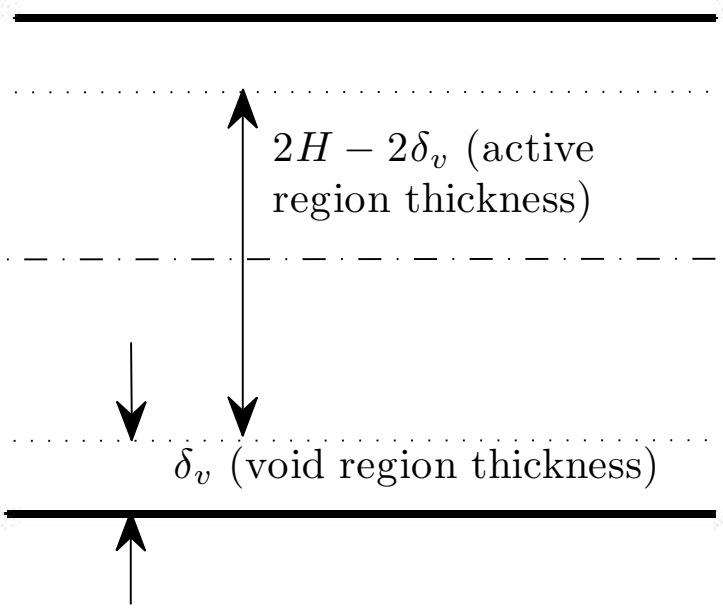

Figure 6.19: The formation of a void region near the surface at higher frequencies ($St > 5$)

Chapter 7

Conclusions

Thermophoresis is an important phenomenon in several scientific and engineering applications, and can be the dominant mechanism of transport of sub-micron particles. Thermophoretis is a force which is driven by differences in temperature on either side of particles, which drives the particles from hotter regions towards the colder ones and may lead to deposition on walls, which can reduce heat transfer. In the current study, the governing equations for particulate transport have been formulated and the effects of using various plausible surface and near-surface boundary conditions have been explored. A new solution has been obtained in the form of a series for the particle concentration profile in fully developed laminar tube flow. This solution appears to be the first reported for this flow, for which no experimental measurements of particle concentration have been made, and the theoretical particle deposition efficiencies derived from this solution appear to be in good agreement with deposition efficiencies measured in experiments. A new measure of the effectiveness of thermophoretic transport—the thermophoretic Sherwood number—was devised. According to this new, exact solution, the thermophoretic conductance, expressed as a thermophoretic Sherwood number, approaches a value of approximately 5 when the fluid, thermal and concentration fields are fully developed.

The particle concentration field in the entrance zone of a particle-laden pipe flow and the effects of compressibility have been studied using numerical analysis. Numerical calculations of the particle deposition efficiency are in good agreement with experimental measurements.

While the numerical solution yields results that are slightly more accurate than those of simple laminar-flow models for entrance-zone and compressibility effects, the computational cost is high. In flows with Mach numbers below 0.2, effects of compressibility on particle deposition efficiency are negligible.

In steady turbulent particle-laden duct flows, results from DNS suggest that particle concentration profiles across the bulk of the flow are almost uniform, in which case a uniform-concentration approximation may be used to formulate a simple one-dimensional model for surface deposition [89]. The particle deposition efficiency evaluated with this model compares well with available experimental measurements. The thickness of soot deposits in an EGR cooler has been evaluated with this one-dimensional model, and is also in good agreement with experimental data. Although turbulent flows are difficult to predict in many applications, it is seen that, in the case of thermophoretic transport of submicron particles in ducts, the uniform particle-concentration model appears to be quite accurate.

In many practical applications, thermophoretic transport of particles takes place in flows that pulsate. The effect of flow oscillation on thermophoretic mass transfer was analyzed numerically. In the model problem of counter-oscillating slug flow (with no mean velocity) in a long channel with imposed axial temperature and concentration gradients, it was found that flow oscillation enhanced the thermophoretic mass transfer by up to 3 orders of magnitude over that in a static fluid. It was also found that the thermophoretic mass transfer (or effective thermophoretic diffusivity λ_{th}) could be tuned to reach a maximum value, by choosing a particular flow oscillation frequency and that λ_{th} also scaled in proportion to $\mathrm{Pr}.K_{th}$. At high values of the flow-oscillation frequency parameter β, thermophoretic transport is dominated by convection so λ and λ_{th} follow similar trends, while at low flow-oscillation frequencies, thermophoretic transport is dominated by the non-linear thermophoretic force

which has a complex behavior. Numerical solutions show that, at low values of β, the thermal flux can surpass the force required to make the particle concentration profile uniform and can, in theory, lead to inverse mass transfer($\lambda_{th} < 0.$). This effect of pulsation on thermophoresis is an interesting topic for further study. Finally, the effect on thermophoresis of unsteady blowing/suction through channel walls was explored. While it seemed possible that thermophoresis could be enhanced in this way, it appeared that the frequencies of pulsation required to achieve significant enhancement would be implausibly high for conventional applications.

APPENDIX

A condition describing the concentration of suspended particles in gas flows in close proximity to a surface is deduced by considering an imaginary interface located a very short distance χ from the surface. The particle mass flux toward the surface (see [144] for more details) is

$$J = c(v_r + v_{th}) - D\frac{\partial c}{\partial r} \tag{1}$$

where v_r and v_{th} are the surface-normal convective and thermophoretically induced components of velocity. It is assumed that the distribution of particles around the convective and thermophorestic velocities $(v_r + v_{th})$ is Maxwellian, by making an analogy between the behaviour of particles and gas molecules. This assumption may have more justification in the free-molecular regime ($Kn \gg 1$) than in the transition regime ($0.1 < Kn < 10$) but it is assumed that the deviation from the Maxwell-Boltzmann distribution is small. If we set $f(\xi_r; \xi_\phi; \xi_z)d\xi_r d\xi_\phi d\xi_z$ to be the number of particles per unit volume having components of velocity with magnitudes in the range: $\xi_r \to \xi_r + d\xi_r, \xi_\phi \to \xi_\phi + d\xi_\phi, \xi_z \to \xi_z + d\xi_z$, the mass flux of particles to the surface is

$$J = \int_{-\infty}^{+\infty}\int_{-\infty}^{+\infty}\int_{-\infty}^{+\infty} m_p.\xi_r f(\xi_r, \xi_\phi, \xi_z)d\xi_r d\xi_\phi d\xi_z \tag{2}$$

The integral can be evaluated by defining

$$c_r = \frac{\xi_-(v_r+v_{th})}{\sqrt{2R_pT}}, \quad c_\phi = \frac{\xi_\phi}{\sqrt{2R_pT}}, \quad c_z = \frac{\xi_z - v_z}{\sqrt{2R_pT}} \tag{3}$$

where m_p is the mass of each particle and f is assumed to be locally Maxwellian in the

moving frame, so

$$f(c_r, c_\phi, c_z) = n_p(2\pi R_p T)^{(-3/2)}\exp(-({c_r}^2 + {c_\phi}^2 + {c_z}^2)) \tag{4}$$

Integration yields the result

$$J = \frac{1}{2} m_p n_p (v_r + v_{th}) \left(1 + erf\{M_r\} + \frac{e^{-{M_r}^2}}{\sqrt{\pi} M_r}\right) \tag{5}$$

where $R_p = k/m_p$ and $M_r = (v_r + v_{th})/\sqrt{2kT/m_p}$. If we assume that χ is small enough so that Eq. 1 and Eq. 5 approach the same value, then

$$\begin{aligned} J &= c(v_r + v_{th}) - D\frac{\partial c}{\partial r} \\ &= \frac{c}{2}(v_r + v_{th}) \left(1 + erf\{M_r\} + \frac{e^{-{M_r}^2}}{\sqrt{\pi} M_r}\right) \end{aligned} \tag{6}$$

at approach to the surface. If v_r is determined from the solution to the radial momentum equation and v_{th} is approximated from the temperature field that satisfies the thermal energy equation and Talbot's model [125]), then Eq. 7 provides a relationship between c and $\partial c/\partial r$ that is a condition on particulate concentration at approach to a surface.

BIBLIOGRAPHY

BIBLIOGRAPHY

[1] M. Abarham, J. Hoard, D. Assanis, D. Styles, E.W. Curtis, N. Ramesh, C.S. Sluder, and J.M.E. Storey. Modeling of Thermophoretic Soot Deposition and Hydrocarbon Condensation in EGR Coolers. *SAE International Journal of Fuels and Lubricants*, 2(1):921, 2009.

[2] M. Abarham, J.W. Hoard, D. Assanis, D. Styles, C.S. Sluder, and J.M.E. Storey. An analytical study of thermophoretic particulate deposition in turbulent pipe flows. *Aerosol Science and Technology*, 44(9):785–795, 2010.

[3] M. Al-Arabi. Turbulent heat transfer in the entrance region of a tube. *Heat Transfer Engineering*, 3(3):76–83, 1981.

[4] C. Asbach, H. Fissan, J.H. Kim, S.J. Yook, and D.Y.H. Pui. Technical note: Concepts for protection of euvl masks from particle contamination. *Journal of Nanoparticle Research*, 8(5):705–708, 2006.

[5] J.J. Bang, E.A. Trillo, and L.E. Murr. Utilization of selected area electron diffraction patterns for characterization of air submicron particulate matter collected by a thermophoretic precipitator. *Journal of the Air & Waste Management Association*, 53(2):227–236, 2003.

[6] GK Batchelor and C. Shen. Thermophoretic deposition of particles in gas flowing over cold surfaces. *Journal of Colloid and Interface Science*, 107(1):21–37, 1985.

[7] P.L. Bhatnagar, E.P. Gross, and M. Krook. A model for collision processes in gases. i. small amplitude processes in charged and neutral one-component systems. *Physical Review*, 94(3):511, 1954.

[8] G.J. Brereton and Y. Jiang. Convective heat transfer in unsteady laminar parallel flows. *Physics of Fluids*, 18:103602, 2006.

[9] J.R. Brock. On the theory of thermal forces acting on aerosol particles. *Journal of Colloid Science*, 17(8):768–780, 1962.

[10] M.H. Carpenter and C.A. Kennedy. Fourth-order 2n-storage runge-kutta schemes. *Nasa tm*, 109112, 1994.

[11] C.Y. Cha and B.J. McCoy. Thermal force on aerosol particles. *Physics of Fluids*, 17:1376, 1974.

[12] M. Chaker, C.B. Meher-Homji, and T.R. Mee III. Inlet fogging of gas turbine engines-part b: Fog droplet sizing analysis, nozzle types, measurement and testing. In *Proceedings of ASME Turbo Expo*, volume 2002, 2002.

[13] YP Chang, R. Tsai, and FM Sui. The effect of thermophoresis on particle deposition from a mixed convection flow onto a vertical flat plate. *Journal of aerosol science*, 30(10):1363–1378, 1999.

[14] H. Chattopadhyay, F. Durst, and S. Ray. Analysis of heat transfer in simultaneously developing pulsating laminar flow in a pipe with constant wall temperature. *International communications in heat and mass transfer*, 33(4):475–481, 2006.

[15] P.C. Chatwin. On the longitudinal dispersion of passive contaminant in oscillatory flows in tubes. *Journal of Fluid Mechanics*, 71(03):513–527, 1975.

[16] S. Chen and G.D. Doolen. Lattice boltzmann method for fluid flows. *Annual review of fluid mechanics*, 30(1):329–364, 1998.

[17] S.J. Choi, D.J. Rader, and A.S. Geller. Massively parallel simulations of brownian dynamics particle transport in low pressure parallel-plate reactors. *Journal of Vacuum Science & Technology A: Vacuum, Surfaces, and Films*, 14(2):660–665, 1996.

[18] JW Cleaver and B. Yates. Mechanism of detachment of colloidal particles from a flat substrate in a turbulent flow. *Journal of Colloid and Interface Science*, 44(3):464–474, 1973.

[19] R.I. Crane. Deposition of fog drops on low pressure steam turbine blades. *International Journal of Mechanical Sciences*, 15(8):613–631, 1973.

[20] E. Cunningham. On the velocity of steady fall of spherical particles through fluid medium. *Proceedings of the Royal Society of London. Series A, Containing Papers of a Mathematical and Physical Character*, 83(563):357–365, 1910.

[21] A. D'Alessio, AC Barone, R. Cau, A. D'Anna, and P. Minutolo. Surface deposition and coagulation efficiency of combustion generated nanoparticles in the size range from 1 to 10 nm. *Proceedings of the Combustion Institute*, 30(2):2595–2603, 2005.

[22] E.J. Davis and G. Schweiger. *The airborne microparticle: its physics, chemistry, optics, and transport phenomena*. Springer Verlag, 2002.

[23] A. Dehbi. A CFD model for particle dispersion in turbulent boundary layer flows. *Nuclear Engineering and Design*, 238(3):707–715, 2008.

[24] A. Dehbi. Turbulent particle dispersion in arbitrary wall-bounded geometries: A coupled CFD-Langevin-equation based approach. *International Journal of Multiphase Flow*, 34(9):819–828, 2008.

[25] A. Dehbi. A stochastic Langevin model of turbulent particle dispersion in the presence of thermophoresis. *International Journal of Multiphase Flow*, 35(3):219–226, 2009.

[26] B.V. Derjaguin and Y. Yalamov. Theory of thermophoresis of large aerosol particles. *Journal of Colloid Science*, 20(6):555–570, 1965.

[27] B.V. Derjaguin and Y. Yalamov. Authors' reply to brock's discussion remarks on the theory of thermophoresis of large aerosol particles. *Journal of Colloid and Interface Science*, 22(2):195–195, 1966.

[28] P. Dumaz, Y. Drossinos, J. Areia Capitao, and I. Drosik. Fission product deposition and revaporization phenomena in scenarios of large temperature differences. In *ANS Proceedings 1993 National Heat Transfer Conference*, pages 348–358. American Nuclear Society Atlanta, GA, 1993.

[29] Campbell E.E. *Volcanic ash. Proc. 747 Flight Oper. Symp.*, pages 231–234, oct.9-11 1990.

[30] N. Epstein. Elements of particle deposition onto nonporous solid surfaces parallel to suspension flows. *Experimental Thermal and Fluid Science*, 14(4):323–334, 1997.

[31] P.S Epstein. *Z. Physik*, 54:437, 1929.

[32] M. Faghri, K. Javdani, and A. Faghri. Heat transfer with laminar pulsating flow in a pipe. *Letters in Heat and Mass Transfer*, 6(4):259–270, 1979.

[33] M. Fichman, C. Gutfinger, and D. Pnueli. A model for turbulent deposition of aerosols. *Journal of aerosol science*, 19(1):123–136, 1988.

[34] S.K. Friedlander and H.F. Johnstone. Deposition of suspended particles from turbulent gas streams. *Industrial & Engineering Chemistry*, 49(7):1151–1156, 1957.

[35] O. Montasser G. Hafez. A theoretical study on enhancing the heat transfer by pulsation. In *11th International Mechanical Power Engineering Conference, Cairo*, 2000.

[36] LG Genin, AP Koval, SP Manchkha, and VG Sviridov. Hydrodynamics and heat transfer with pulsating fluid flow in tubes. *Thermal engineering*, 39(5):251–255, 1992.

[37] V. Gnielinski. New equations for heat and mass transfer in turbulent pipe and channel flow. *International chemical engineering: 25th anniversary issue, 1961-1985*, 41(1):126, 1988.

[38] D. Gonzalez, A.G. Nasibulin, A.M. Baklanov, S.D. Shandakov, D.P. Brown, P. Queipo, and E.I. Kauppinen. A new thermophoretic precipitator for collection of nanometer-sized aerosol particles. *Aerosol science and technology*, 39(11):1064–1071, 2005.

[39] S.L. Gorelov. Thermophoresis and photophoresis in a rarefied gas. *Fluid Dynamics*, 11(5):800–804, 1976.

[40] S.L. Goren. Thermophoresis of aerosol particles in the laminar boundary layer on a flat plate. *Journal of Colloid and Interface Science*, 61(1):77–85, 1977.

[41] A. Guha. Transport and deposition of particles in turbulent and laminar flow. 2008.

[42] Z. Guo and H.J. Sung. Analysis of the nusselt number in pulsating pipe flow. *International journal of heat and mass transfer*, 40(10):2486–2489, 1997.

[43] SK Gupta, TRD Patel, and RC Ackerberg. Wall heat/mass transfer in pulsatile flow. *Chemical Engineering Science*, 37(12):1727–1739, 1982.

[44] V.R. GUTTI and S.K. LOYALKA. Thermophoretic deposition in a cylindrical tube: Computations and comparison with experiments. *Nuclear technology*, 166(2):121–133, 2009.

[45] MA Habib, AM Attya, AI Eid, and AZ Aly. Convective heat transfer characteristics of laminar pulsating pipe air flow. *Heat and mass transfer*, 38(3):221–232, 2002.

[46] MA Habib, AM Attya, SAM Said, AI Eid, and AZ Aly. Heat transfer characteristics and nusselt number correlation of turbulent pulsating pipe air flows. *Heat and mass transfer*, 40(3):307–318, 2004.

[47] MA Habib, SAM Said, AA Al-Farayedhi, SA Al-Dini, A. Asghar, and SA Gbadebo. Heat transfer characteristics of pulsated turbulent pipe flow. *Heat and mass transfer*, 34(5):413–421, 1999.

[48] C. He and G. Ahmadi. Particle deposition with thermophoresis in laminar and turbulent duct flows. *Aerosol science and technology*, 29(6):525–546, 1998.

[49] H.N. Hemida, M.N. Sabry, A. Abdel-Rahim, and H. Mansour. Theoretical analysis of heat transfer in laminar pulsating flow. *International journal of heat and mass transfer*, 45(8):1767–1780, 2002.

[50] J. Heyder, J. Gebhart, G. Rudolf, C.F. Schiller, and W. Stahlhofen. Deposition of particles in the human respiratory tract in the size range 0.005-15 [mu] m. *Journal of Aerosol Science*, 17(5):811–825, 1986.

[51] GM Homsy, FT Geyling, and KL Walker. Blasius series for thermophoretic deposition of small particles. *Journal of Colloid and Interface Science*, 83(2):495–501, 1981.

[52] C. Housiadas and Y. Drossinos. Thermophoretic deposition in tube flow. *Aerosol Science and Technology*, 39(4):304–318, 2005.

[53] B. Hu, B. Yang, and U.O. Koylu. Soot measurements at the axis of an ethylene/air non-premixed turbulent jet flame. *Combustion and flame*, 134(1-2):93–106, 2003.

[54] F. Incropera and D. DeWitt. Introduction to heat transfer. 1985.

[55] B. Ismail, F. Charles, D. Ewing, J.S. Cotton, and J.S. Chang. Mitigation of the diesel soot deposition effect on the exhaust gas recirculation (EGR) cooling devices for diesel engines. 2005.

[56] B. Ismail, D. Ewing, and J.S. Chang. Development of a non-destructive neutron radiography technique to measure the three-dimensional soot deposition profiles in diesel engine exhaust systems. *Journal of Aerosol Science*, 35(10):1275–1288, 2004.

[57] B.I.A. Ismail. The heat transfer and the soot deposition characteristics in diesel engine exhaust gas recirculation system cooling devices. *Open Dissertations and Theses*, page 1588, 2004.

[58] A.C. K Lai and W.W. Nazaroff. Modeling indoor particle deposition from turbulent flow onto smooth surfaces. *Journal of aerosol science*, 31(4):463–476, 2000.

[59] O.E. Karamercan and J.L. Gainer. The effect of pulsations on heat transfer. *Industrial & Engineering Chemistry Fundamentals*, 18(1):11–15, 1979.

[60] W.M. Kays, M.E. Crawford, and B. Weigand. *Convective heat and mass transfer*. McGraw-Hill New York, 1966.

[61] E.H. Kennard and E.H. Kennard. *Kinetic theory of gases: with an introduction to statistical mechanics*. McGraw-Hill New York, 1938.

[62] J.H. Kim, G.W. Mulholland, S.R. Kukuck, and DH Pui. Slip correction measurements of certified psl nanoparticles using a nanometer differential mobility analyzer (nanodma) for knudsen number from 0.5 to 83. *JOURNAL OF RESEARCH-NATIONAL INSTITUTE OF STANDARDS AND TECHNOLOGY*, 110(1):31, 2005.

[63] S.Y. Kim. *Convective Heat Transfer Enhancement in a Confined Passageway*. PhD thesis, Korea Advanced Institute of Science and Technology, 1995.

[64] S.Y. Kim, B.H. Kang, and J.M. Hyun. Heat transfer in the thermally developing region of a pulsating channel flow. *International journal of heat and mass transfer*, 36(17):4257–4266, 1993.

[65] A.G. Konstandopoulos. Deposit growth dynamics: particle sticking and scattering phenomena. *Powder Technology*, 109(1-3):262–277, 2000.

[66] A.G. Konstandopoulos, E. Skaperdas, and M. Masoudi. Microstructural properties of soot deposits in diesel particulate traps. 2002.

[67] U.O. Koylu and G.M. Faeth. Structure of overfire soot in buoyant turbulent diffusion flames at long residence times. *Combustion and Flame*, 89(2):140–156, 1992.

[68] U.H. Kurzweg. Temporal and spatial distribution of heat flux in oscillating flow subjected to an axial temperature gradient. *International journal of heat and mass transfer*, 29(12):1969–1977, 1986.

[69] U.H. Kurzweg and L. De Zhao. Heat transfer by high-frequency oscillations: A new hydrodynamic technique for achieving large effective thermal conductivities. *Physics of Fluids*, 27:2624, 1984.

[70] A.C.K. Lai and W.W. Nazaroff. Modeling indoor particle deposition from turbulent flow onto smooth surfaces. *Journal of Aerosol Science*, 31(4):463–476, 2000.

[71] S. Lain and J.A. Garcia. Study of four-way coupling on turbulent particle-laden jet flows. *Chemical engineering science*, 61(20):6775–6785, 2006.

[72] M.J. Lance, C.S. Sluder, H. Wang, and J.M.E. Storey. Direct Measurement of EGR Cooler Deposit Thermal Properties for Improved Understanding of Cooler Fouling. 2009.

[73] M.M. Lee, T.J. Hanratty, and RJ Adrian. The interpretation of droplet deposition measurements with a diffusion model. *International journal of multiphase flow*, 15(3):459–469, 1989.

[74] W. Li and E. James Davis. The effects of gas and particle properties on thermophoresis. *Journal of aerosol science*, 26(7):1085–1099, 1995.

[75] W. Li and E. James Davis. Measurement of the thermophoretic force by electrodynamic levitation: Microspheres in air. *Journal of aerosol science*, 26(7):1063–1083, 1995.

[76] N.S. Liao and C.C. Wang. An investigation of the heat transfer in pulsating turbulent pipe flow. fundamentals of forced and mixed convection. In *The 23rd National Heat Transfer Conference. Denver. Co., USA,*, 1985.

[77] B.Y.H. Liu and J.K. Agarwal. Experimental observation of aerosol deposition in turbulent flow. *Journal of Aerosol Science*, 5(2):145–148, 1974.

[78] S.K. Loyalka. Thermophoretic force on a single particle–i. numerical solution of the linearized boltzmann equation. *Journal of aerosol science*, 23(3):291–300, 1992.

[79] C. Ludwig. "diffusion zwischen ungleich erwwrmten orten gleich zusammengestzter lsungen". *Sitz. Ber. Akad. Wiss. Wien Math-Naturw. Kl.*, 20:539, 1856.

[80] S.L. Manzello, D.B. Lenhert, A. Yozgatligil, M.T. Donovan, G.W. Mulholland, M.R. Zachariah, and W. Tsang. Soot particle size distributions in a well-stirred reactor/plug flow reactor. *Proceedings of the Combustion Institute*, 31(1):675–683, 2007.

[81] S.L. Manzello, G.W. Mulholland, M. Donovan, W. Tsang, K. Park, M. Zachariah, and S.D. Stouffer. On the use of a well stirred reactor to study soot inception. In *Fourth Joint Meeting of the US Sections of the Combustion Institute, Philadelphia, Pa*, pages 20–23, 2005.

[82] Z. Mao and T.J. Hanratty. Application of an inverse mass transfer method to the measurement of turbulent fluctuations in the velocity gradient at the wall. *Experiments in Fluids*, 11(1):65–73, 1991.

[83] Z.X. Mao and T.J. Hanratty. The use of scalar transport probes to measure wall shear stress in a flow with imposed oscillations. *Experiments in fluids*, 3(3):129–135, 1985.

[84] M.M. Maricq. Size and charge of soot particles in rich premixed ethylene flames. *Combustion and Flame*, 137(3):340–350, 2004.

[85] M.M. Maricq. On the electrical charge of motor vehicle exhaust particles. *Journal of Aerosol Science*, 37(7):858–874, 2006.

[86] A.D. Maynard. The development of a new thermophoretic precipitator for scanning transmission electron microscope analysis of ultrafine aerosol particles. *Aerosol science and technology*, 23(4):521–533, 1995.

[87] D.D. McCoy and T.J. Hanratty. Rate of deposition of droplets in annular two-phase flow. *International Journal of Multiphase Flow*, 3(4):319–331, 1977.

[88] J.B. McLaughlin. Aerosol particle deposition in numerically simulated channel flow. *Physics of Fluids A: Fluid Dynamics*, 1:1211, 1989.

[89] M. Mehravaran and G. Brereton. Modeling of thermophoretic soot deposition and stabilization on cooled surfaces. 2011.

[90] A. Messerer, R. Niessner, and U. Poschl. Miniature pipe bundle heat exchanger for thermophoretic deposition of ultrafine soot aerosol particles at high flow velocities. *Aerosol Science and Technology*, 38(5):456–466, 2004.

[91] N. Montassier, D. Boulaud, and A. Renoux. Experimental study of thermophoretic particle deposition in laminar tube flow. *Journal of Aerosol Science*, 22(5):677–687, 1991.

[92] T. Moschandreou and M. Zamir. Heat transfer in a tube with pulsating flow and constant heat flux. *International journal of heat and mass transfer*, 40(10):2461–2466, 1997.

[93] R. Muŋoz-Bueno, E. Hontaŋkŋn, and MI Rucandio. Deposition of fine aerosols in laminar tube flow at high temperature with large gas-to-wall temperature gradients. *Journal of aerosol science*, 36(4):495–520, 2005.

[94] Y. Nakamura, Y. Yonekawa, and N. Okamoto. Effect of the combustion chamber deposits on octane requirement increase and fuel economy. *Am. Chem. Soc., Div. Pet. Chem., Prepr.;(United States)*, 26(2), 1981.

[95] H. Nasr and G. Ahmadi. The effect of two-way coupling and inter-particle collisions on turbulence modulation in a vertical channel flow. *International Journal of Heat and Fluid Flow*, 28(6):1507–1517, 2007.

[96] A. Neer and U.O. Koylu. Effect of operating conditions on the size, morphology, and concentration of submicrometer particulates emitted from a diesel engine. *Combustion and Flame*, 146(1-2):142–154, 2006.

[97] K. Nishiwaki. Unsteady thermal behavior of engine combustion chamber deposits. Technical report, Society of Automotive Engineers, Warrendale, PA, 1988.

[98] P.G. Papavergos and A.B. Hedley. Review Paper-Particle deposition behavour from turbulent flows. *Chemical Engineering Research and Design*, 62(a):275–295, 1984.

[99] A. Parola and R. Piazza. Particle thermophoresis in liquids. *The European Physical Journal E: Soft Matter and Biological Physics*, 15(3):255–263, 2004.

[100] T.W. Peterson, F. Stratmann, and H. Fissan. Particle deposition on wafers: a comparison between two modeling approaches. *Journal of aerosol science*, 20(6):683–693, 1989.

[101] J.K. Platten. The soret effect: a review of recent experimental results. *Journal of applied mechanics*, 73:5, 2006.

[102] T.J. Poinsot and S.K. Lelef. Boundary conditions for direct simulations of compressible viscous flows. *Journal of computational physics*, 101(1):104–129, 1992.

[103] G. Prado, J. Jagoda, K. Neoh, and J. Lahaye. A study of soot formation in premixed propane/oxygen flames by in-situ optical techniques and sampling probes. In *Symposium (International) on Combustion*, volume 18, pages 1127–1136. Elsevier, 1981.

[104] M.W. Reeks. On the dispersion of small particles suspended in an isotropic turbulent fluid. *J. Fluid Mech*, 83(3):529–546, 1977.

[105] L.P. Reiss and T.J. Hanratty. An experimental study of the unsteady nature of the viscous sublayer. *AIChE Journal*, 9(2):154–160, 1963.

[106] H.C. Reynolds, T.B. Swearingen, and D.M. McEligot. Thermal entry for low Reynolds number turbulent flow. *J. Basic Eng*, 91:87–94, 1969.

[107] F.J. Romay, S.S. Takagaki, D.Y.H. Pui, and B.Y.H. Liu. Thermophoretic deposition of aerosol particles in turbulent pipe flow. *Journal of Aerosol Science*, 29(8):943–959, 1998.

[108] D.E. Rosner. Total mass deposition rates from polydispersed aerosols. *AIChE journal*, 35(1):164–167, 1989.

[109] D.E. Rosner and Y.F. Khalil. Particle morphology-and Knudsen transition- effects on thermophoretically dominated total mass deposition rates from. *Journal of Aerosol Science*, 31(3):273–292, 2000.

[110] D.H. Rudy and J.C. Strikwerda. A nonreflecting outflow boundary condition for subsonic navier-stokes calculations. *Journal of Computational Physics*, 36(1):55–70, 1980.

[111] R.D. Sandberg. Governing equations for a new compressible navier-stokes solver in general cylindrical coordinates. 2007.

[112] A. Sasse, W.W. Nazaroff, and A.J. Gadgil. Particle filter based on thermophoretic deposition from natural convection flow. *Aerosol science and technology*, 20(3):227–238, 1994.

[113] S. Sato, D. Chen, and D.Y.H. Pui. Molecular Dynamics Study of Nanoparticle Collision with a Surface- Implication to Nanoparticle Filtration. *Aerosol and Air Quality Resarch*, 7(3):278–303, 2007.

[114] K.H. Schmitt. Untersuchungen an schwebstoffteilchen im temperaturfeld. *Zeitschrift Naturforschung Teil A*, 14:870, 1959.

[115] RK Shah and AL London. *Laminar flow forced convection in ducts. In Supplement l to Advances m Heat Transfer*. Academic Press, New York, 1978.

[116] H. Shokouhmand and K. Hooman. An Exact Solution for Fully Developed Temperature Distribution in Laminar Steady Forced Convection Inside Circular Tubes with Uniform Wall Temperature. *Journal of Porous Media*, 11(4), 2008.

[117] E.N. Sieder and G.E. Tate. Heat transfer and pressure drop of liquids in tubes. *Industrial & Engineering Chemistry*, 28(12):1429–1435, 1936.

[118] G.W. Smith. A simple nucleation/depletion model for the spherule size of particulate carbon. *Combustion and Flame*, 48:265–272, 1982.

[119] Y. Sone and K. Aoki. A similarity solution of the linearized boltzmann equation with application to thermophoresis of a spherical particle. *Journal de Mécanique Théorique et Appliquée*, 2:3–12, 1983.

[120] Ch. Soret. "influence de la temprature sur la distribution des sels dans leurs solutions,". *Acad. Sci., Paris,*, 91(5):289291, 1880.

[121] Ch. Soret. "sur l'tat d'quilibre que prend au point de vue de sa concentration une dissolution saline primitivement homohne dont deux parties sont portes des tempratures diffrentes". *Arch. Sci. Phys. Nat.*, 2:48–61, 1979.

[122] F. Stratmann and H. Fissan. Experimental and theoretical study of submicron particle transport in cooled laminar tube flow due to combined convection, diffusion, and thermophoresis. *Journal of Aerosol Science*, 20(8):899–902, 1989.

[123] F. Stratmann, E. Otto, and H. Fissan. Thermophoretical and diffusional particle transport in cooled laminar tube flow. *Journal of Aerosol Science*, 25(7):1305–1319, 1994.

[124] S. Suzuki, K. Kuwana, and R. Dobashi. Effect of particle morphology on thermophoretic velocity of aggregated soot particles. *International Journal of Heat and Mass Transfer*, 52(21-22):4695–4700, 2009.

[125] C. Talbot. Schefer, & Willis 1980. L. Talbot, R.K. Cheng, R.W. Schefer and D.R. Willis, Thermophoresis of particles in a heated boundary layer. *Journal of Fluid Mechanics*, 101(4), 1980.

[126] D.M. Taylor. Human respiratory tract model for radiological protection. *Journal of Radiological Protection*, 16, 1996.

[127] G. Taylor. Dispersion of soluble matter in solvent flowing slowly through a tube. *Proceedings of the Royal Society of London. Series A. Mathematical and Physical Sciences*, 219(1137):186–203, 1953.

[128] H. Teng and G. Regner. Particulate fouling in egr coolers. *SAE International Journal of Commercial Vehicles*, 2(2):154, 2010.

[129] D.G. Thakurta, M. Chen, J.B. McLaughlin, and K. Kontomaris. Thermophoretic deposition of small particles in a direct numerical simulation of turbulent channel flow. *International journal of heat and mass transfer*, 41(24):4167–4182, 1998.

[130] K. Tian, K.A. Thomson, F. Liu, D.R. Snelling, G.J. Smallwood, and D. Wang. Determination of the morphology of soot aggregates using the relative optical density method for the analysis of TEM images. *Combustion and Flame*, 144(4):782–791, 2006.

[131] C.J. Tsai, J.S. Lin, S.G. Aggarwal, and D.R. Chen. Thermophoretic deposition of particles in laminar and turbulent tube flows. *Aerosol science and technology*, 38(2):131–139, 2004.

[132] C.J. Tsai and H.C. Lu. Design and evaluation of a plate-to-plate thermophoretic precipitator. *Aerosol science and technology*, 22(2):172–180, 1995.

[133] F. Vasak, BD Bowen, C.Y. Chen, F. Kastanek, and N. Epstein. Fine particle deposition in laminar and turbulent flows. *Canadian journal of chemical engineering*, 73(6):785–792, 1995.

[134] H. Waldman and K.L. Schmitt. *Thermophoresis and Diffusiophoresis of aerosols*. Academic Press, New York, 1966.

[135] L. Waldmann. Über doe kraft eines inhomogenen gases auf kleine suspendierte kugeln. *Zeitschrift Naturforschung Teil A*, 14:589, 1959.

[136] K.L. Walker, G.M. Homsy, and F.T. Geyling. Thermophoretic deposition of small particles in laminar tube flow. *Journal of Colloid and Interface science*, 69(1):138–147, 1979.

[137] J.K. Walsh, A.W. Weimer, and C.M. Hrenya. Thermophoretic deposition of aerosol particles in laminar tube flow with mixed convection. *Journal of aerosol science*, 37(6):715–734, 2006.

[138] A. Warey, S. Balestrino, P. Szymkowicz, and M.R. Malayeri. A one-dimensional model for particulate deposition and hydrocarbon condensation in exhaust gas recirculation coolers. *Aerosol Science and Technology*, 46(2):198–213, 2012.

[139] E.J. Watson. Diffusion in oscillatory pipe flow. *Journal of Fluid Mechanics*, 133(1):233–244, 1983.

[140] M.C. Weinberg. Calculation of thermophoretic deposition efficiency of particles in tubes. *Journal of Colloid and Interface Science*, 84(2):550–551, 1981.

[141] N.B. Wood. Mass transfer of particles and acid vapor to cooled surfaces. *Journal of the Institute of Energy*, 54(419):76–93, 1981.

[142] K. Yamamoto and Y. Ishihara. Thermophoresis of a spherical particle in a rarefied gas of a transition regime. *Physics of Fluids*, 31:3618, 1988.

[143] Y. Ye, DYH Pui, BYH Liu, S. Opiolka, S. Blumhorst, and H. Fissan. Thermophoretic effect of particle deposition on a free standing semiconductor wafer in a clean room. *Journal of Aerosol Science*, 22(1):63–72, 1991.

[144] J. Young and A. Leeming. A theory of particle deposition in turbulent pipe flow. *Journal of Fluid Mechanics*, 340:129–159, 1997.

[145] J.B. Young and K.K. Yau. The inertial deposition of fog droplets on steam turbine blades. *Journal of turbomachinery*, 110:155, 1988.

[146] J.C. Yu, Z.X. Li, and TS Zhao. An analytical study of pulsating laminar heat convection in a circular tube with constant heat flux. *International journal of heat and mass transfer*, 47(24):5297–5301, 2004.